CRWR Online Report 04-09

Hydrostatic and Non-hydrostatic Internal Wave Models

by

Bridget M. Wadzuk, B.S., M.S
Graduate Research Assistant

and

Ben R. Hodges, Ph.D.
Principal Investigator

The University of Texas at Austin
December 4, 2004

Final Report to the Office of Naval Research
under Contract No. N00014-01-1-0574

This document is available online via World Wide Web at
http://www.crwr.utexas.edu/online.html

Abstract

Numerical models have become an indispensable tool for ocean and inland flow modeling. Such models typically use the hydrostatic approximation based on the argument that their horizontal length scales are longer than the vertical length scales. There are a wide variety of physical processes in oceans and inland water systems, and many of these processes are adequately modeled with the hydrostatic approximation. However, internal waves contribute to the physics that influence mixing in a density stratified system and have been previously shown to be non-hydrostatic. The neglect of non-hydrostatic pressure in a hydrostatic model is problematic since non-hydrostatic pressure plays a significant role in internal wave evolution balancing nonlinear wave steepening. Where non-hydrostatic pressure is neglected in a model, the governing equations are missing a piece of the physics that control the internal wave evolution, so it should not be surprising that the evolution may be poorly predicted.

Despite the knowledge that the non-hydrostatic pressure is necessary for correctly modeling the physics of a steepening internal wave, the high computational cost of solving the non-hydrostatic pressure has limited its use in large-scale systems. Furthermore, the errors associated with hydrostatic modeling of internal waves have not been quantified. This research quantifies the differences between hydrostatic and non-hydrostatic simulations of internal wave evolution and develops a method to a priori determine regions with non-hydrostatic behavior. In quantifying the errors and differences between the two models this research provides the characteristics of model error with grid refinement. Additionally, it is shown that hydrostatic models may develop high wavenumber "soliton-like" features that are purely a construct of model error, but may seem to mimic physical behaviors of the non-hydrostatic system. Finally, it is shown that regions of significant non-hydrostatic pressure gradients can be identified from a hydrostatic model. This latter finding is a building block towards coupling local non-hydrostatic solutions with global hydrostatic solutions for more efficient computational methods. The work presented here provides the foundations for future non-hydrostatic model development and application.

Chapter 1. Introduction

1.1 Motivation

Biogeochemical processes in oceans, lakes and estuaries evolve against the background of vertical density stratification. Internal waves are one mechanism which carry energy and momentum through a basin and contribute to mixing events in littoral regions that prompt ecosystem changes. Internal waves are motions that occur beneath the free-surface of a density-stratified waterbody. As an external force (i.e. wind or river inflow) moves the density layers from their equilibrium position, an internal wave is initiated to restore the system to equilibrium (Figure 1.1). Internal waves propagate through the basin and interact with the basin boundaries; this internal wave – slope interaction is an important source of energy that transports nutrients, biota and contaminants through the water column (Imberger and Ivey, 1993; Javam, et al., 1999). Hydrodynamic processes (e.g. internal waves, tides and eddies) are transport mechanisms in coastal oceans and lakes and their scope and magnitude depends on the processes' speed and length scales. Table 1.1 shows a large range of scales for different hydrodynamic processes and internal waves are considered a middle-scale process.

Quantitative assessment of nutrient and constituent transport in a stratified basin requires modeling of internal wave evolution (Imberger, 1994). To have an unambiguous water quality model, the complementary hydrodynamic model, which provides the flow field, should simulate all the significant physics (Gross, et al., 1999). Hydrodynamic models often neglect physics that are irrelevant to the focus of an investigation or can be a priori scaled as small compared to dominant (Marshall, et al., 1997). Large-scale ocean and littoral modeling have traditionally made the hydrostatic approximation, which neglects non-hydrostatic pressure and subsequently vertical momentum (e.g. POM: Blumberg and Mellor, 1987; EFDC: Hamrick, 1992; ROMS: Haidvogel, et al., 2000; Ezer, et al., 2002). The hydrostatic approximation fails at open boundaries (Mahadevan, et al., 1996a) and at steep slopes with strong vertical velocities (Weilbeer and Jankowski, 2000; Horn, et al., 2001; Horn, et al., 2002). Linear waves that are damped by viscous effects may be considered to

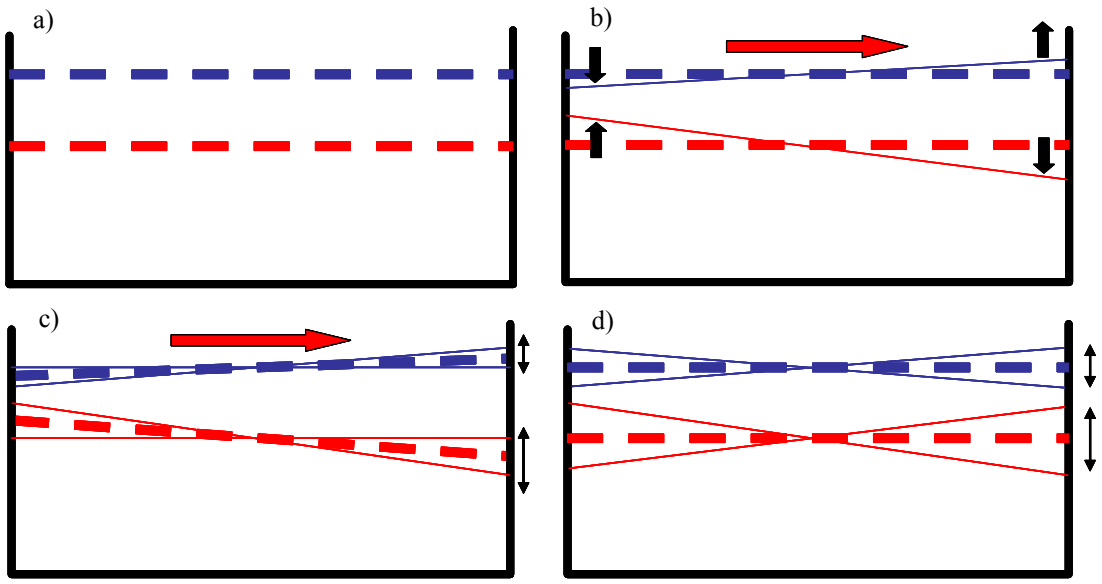

Figure 1.1: Internal wave evolution in a two-layer system. a) System at rest, where the equilibrium position for the free-surface (thick dashed blue line) and pycnocline (thick dashed red line) is flat. b) Wind is applied over the free surface (large red arrow) which moves the free-surface (thin blue line) and pycnocline (thin red line) from their respective equilibrium positions. c) Continued application of wind over the free-surface, so the equilibrium positions for the free-surface and pycnocline are tilted. The free-surface and pycnocline oscillate around the equilibrium position. d) The wind force stops and the free-surface and pycnocline equilibrium position is flat. The free-surface and pycnocline oscillate around the equilibrium position, setting up a basin-scale seiche.

Table 1.1: Scales of oceanic processes (Gill, 1982; Cushman-Roisin, 1994; Kantha & Clayson, 2000a; Miropol'sky, 2001)

Process/Activity	Speed (m/s)	Length
Oceanic Turbulence	0.1 - 100	1 cm - 100 m
Internal Waves	1 - 3	100 m - 1 km
Diurnal Tides	0.1 - 10	1 km - 1000 km
Mesoscale Eddy	1	10 km - 1000 km
Rossby Waves	0.1 - 9	1000 km - 10000 km
Surface Gravity Waves	1 - 20	1 m - 100 m
Sound waves	1400	200 km

behave hydrostatically, while internal waves that steepen nonlinearly are inherently non-hydrostatic (Long, 1972). It is suggested that non-hydrostatic pressure is essential for proper modeling of internal wave development and propagation (Laval, et al., 2003). When numerical models neglect non-hydrostatic pressure, they are neglecting a physical attribute of internal wave evolution. This neglect has repercussions on vertical transport at the topographic boundaries of a basin. Internal waves that nonlinearly steepen and degenerate into solitons can propagate to a basin's boundary where the wave may shoal and mix, energizing a turbulent benthic boundary layer (Boegman, et al., 2003); the interaction of internal waves and boundary layer mixing is a significant mechanism for nutrient transport and other biogeochemical processes (De Silva, et al., 1997; Nishri, et al., 2000). Modeling the boundary layer is not of interest to the present research, but properly modeling the internal wave evolution which contributes to boundary layer is.

During the past decade there has been interest simulating internal waves in numerical models, marked by the development of several non-hydrostatic models (e.g. Mahadevan, et al., 1996a,b; Marshall, et al., 1997; Stansby and Zhou, 1998; Casulli, 1999; Weilbeer and Jankowski, 2000; Fringer and Street, 2003; Daily and Imberger, 2003; Yuan and Wu, 2004). However, there has been little work done on quantifying the differences between hydrostatic and non-hydrostatic models or the scales for which non-hydrostatic pressure impacts internal wave evolution. If the proper scales (i.e. sufficient grid resolutions) are not used in a non-hydrostatic model, then the results of the non-hydrostatic model are no different than a hydrostatic model's solution, as described in §4.2

Presently, computational power is insufficient for application of non-hydrostatic models to large domains (i.e. coastal oceans) with sufficient grid resolution. By example, one computational "work unit" may be considered the processing power required for one operation across the entire domain. Thus, a work unit scales on the number of cells within a domain (e.g. a grid of N × M size: 1 work unit = N × M). A hydrostatic model's basic operations are solving for the three velocity components, salinity transport, temperature transport and the free-surface; the computational effort for each of these operations scales on one work unit, thus totaling six work units for each timestep. A non-hydrostatic model solves for these operations twice (once before the non-hydrostatic solver and once after) and a pressure solution. The work associated with the pressure solution is N × M × the number of smoothing iterations per timestep; the number of iterations per timestep for the non-hydrostatic pressure solver may be $O(10^2)$ (§3.2 ff.). If the non-hydrostatic model is applied with the same spatial grid and timestep as the hydrostatic model, the non-hydrostatic model requires an additional 10^6 work units, that is, about two orders of magnitude more computational effort. However, as discussed in §4, the non-hydrostatic model also requires a finer spatial grid and timestep than a hydrostatic model. A typical hydrostatic coastal ocean model applies a spatial grid with an aspect ratio ($\Delta z/\Delta x$) of $O(10^{-3})$ (Marshall, et al., 1997; Tartinville, et al., 1998), while §4 shows that a non-hydrostatic model requires a grid with an aspect ratio of at least $O(10^{-2})$. This refined spatial grid increases the required work units by another order of magnitude, to $\sim 10^3$. Furthermore, §4 discusses the need for a non-hydrostatic model to be applied to a smaller timestep, which increases the number of work units by another order of magnitude. Thus, $O(10^4)$ work units are needed for the non-hydrostatic model, while the hydrostatic computational effort scales on $O(10)$ work units. According to Moore's law (Moore, 1965), computational ability doubles about every two years. Assuming that we are reaching the maximum capacity of present computers with the hydrostatic model, the computational power needed to run a coastal ocean non-hydrostatic model with a sufficiently fine spatial grid and timestep will not be available for another 26 years! It is computational power that limits our ability to use non-hydrostatic models. This motivates the present research to quantify the spatial grid and timestep necessary to apply a non-hydrostatic model and develop the theoretical foundations for future methods that may circumvent the constraint of computational power.

1.2 Objectives

The present research has two main objectives to address the motivational issues within internal wave modeling:

- quantify the differences between hydrostatic and non-hydrostatic simulations of internal wave evolution, and
- develop a method to a priori determine regions with non-hydrostatic behavior.

The first objective is achieved by: 1) quantifying accumulation of error within both hydrostatic and non-hydrostatic models of internal waves; and 2) comparing the space-time evolution of internal wave characteristics in both models. Comparing the models' internal wave evolution and error accumulation provides a means of defining the conditions for which a hydrostatic model is acceptable and those conditions requiring a non-hydrostatic model to capture an internal wave's propagation. It is shown that a model's error accumulation and representation of internal wave evolution are dependent on spatial and temporal resolution. Delineation of the spatial and temporal resolution necessary to adequately resolve non-hydrostatic processes is included within the first objective.

The second objective is achieved by using a hydrostatic model to estimate non-hydrostatic pressure effects. Using this estimation, local regions where the non-hydrostatic pressure significantly contributes to internal wave evolution are identified. Through reaching this objective, the present work provides the theoretical basis for future model development for a non-hydrostatic solution in isolated, "non-hydrostatic" areas, concurrent with a hydrostatic solution elsewhere.

1.3 Background

1.3.1 Internal Waves

Internal waves occur in stably stratified fluids when a water parcel is displaced by some external force (wind, inflow, etc.) and is restored by buoyancy forces; the restoration motion may overshoot the equilibrium position and set up an oscillation thereby forming an internal wave (Turner, 1973; Kantha and Clayson, 2000a). The buoyancy frequency (N) is the upper limit of wave frequencies (ω) that can propagate through a system; thus, the only internal waves of interest for the present research are those where $\omega < N$, as waves where $\omega > N$ remain local and do not significantly contribute to the system's overall transport and energy (Turner, 1973; Lighthill, 1978; Javam, et al., 1999). The lower limit of internal wave frequencies is the Coriolis or inertial wave frequency, f. The inertial frequency is defined as $f = 2\Omega\sin\varphi$, where Ω is the angular velocity of the earth's rotation and φ is the latitude. At f, wave motions become inertial oscillations, where fluid parcels have horizontally circular trajectories (Cushman-Roisin, 1994). While Coriolis forces are known to affect internal wave evolution, their impact is principally three-dimensional. To limit the number of processes under consideration, this project is restricted to vertical stratification in two-dimensional box models where Coriolis effects cannot be represented. Thus, this project is focused primarily on internal waves dominated by gravity, which is typically the case for waves breaking on sloping boundaries (De Silva, et al., 1997).

Field studies by Garrett and Munk (1979) indicated that most internal waves follow a consistent energy-wave spectrum (Figure 1.2). There is a full range of wave frequencies and associated energy, where waves of low-frequency are associated with high energy, while those of high-frequency have low energy. Internal waves also evolve over a wide spectrum of spatial scales. An initial low-frequency, long wavelength internal wave may degenerate into a train of high-frequency, short

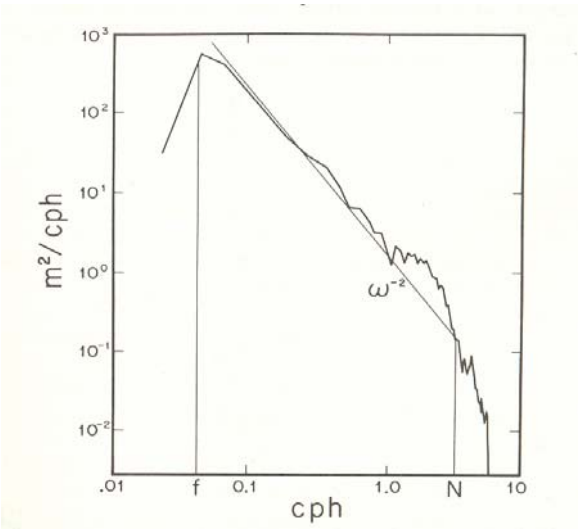

Figure 1.2: Energy-Frequency Spectrum. f is the Coriolis frequency, N is the Brunt-Väisälä frequency and ω is the frequency, cph (cycles per hour) is a frequency scale and m^2/cph is an energy scale. (Garrett and Munk, 1979)

wavelength waves (Kao, et al., 1985; Horn, et al., 2001; Boegman, et al., 2003), as seen in Figure 1.3. This degeneration is connected to the nonlinearity of internal waves. Several field studies (Farmer, 1978; Osborne and Burch, 1980; Apel, 1981; Wiegand and Carmack, 1986) and model results (Segur and Hammack, 1982; Hutter, et al., 1998; Horn, et al., 2002) have verified that an internal wave will behave nonlinearly if the initial wave is sufficiently steep. Steepness is defined as the ratio of a wave's amplitude to its wavelength. A "sufficiently" steep wave is one whose timescale for steepening is shorter than its timescale for damping (Farmer, 1978; Horn, et al., 2001). The relationship between the total water depth and thickness of the upper layer can also contribute to a wave's nonlinearity.

The following description of wave evolution is adapted from Kinsman (1965), Whitham (1974) and Lighthill (1978). A wave may be viewed as a recognizable feature of a disturbance that moves with a finite velocity. An infinite number of sinusoidal waves, each with a discrete frequency and discrete wavelength, may be superposed to create the characteristic material surface recognizable as a wave (Figure 1.4 A). Wave speed (c):

$$c = \frac{\omega}{k} \tag{1.1}$$

where ω is the wave frequency and k is the total wavenumber (i.e. $k = \sqrt{j^2 + l^2 + m^2}$; j, l and m are the wavenumbers in the x-, y- and z-directions, respectively) is dependent on the dispersion relationship for an internal wave:

$$\omega^2 = N^2 \frac{\left(j^2 + l^2\right)}{\left(j^2 + l^2 + m^2\right)} \tag{1.2}$$

where the buoyancy frequency, N^2 is:

$$N^2 = \frac{g}{\rho_o}\frac{d\rho}{dz} \tag{1.3}$$

It follows that wave speed is dependent upon the density gradient of fluid. Waves on different density structures propagate at different speeds (i.e. the crest of the wave, with one density gradient, is moving faster than the trough of the wave, with another density gradient, as seen in Figure 1.4 B&C). This density gradient dependency produces a nonlinearly steepening wave. Wave speed is also dependent on wavelength (the inverse of the wavenumber). As the different sinusoidal waves comprising the material wave move at different speeds, the material wave spreads out over time, or disperses, into a series of waves (Figure 1.4 D).

The wave speed dependence on the dispersion relationship shows there is a relationship between

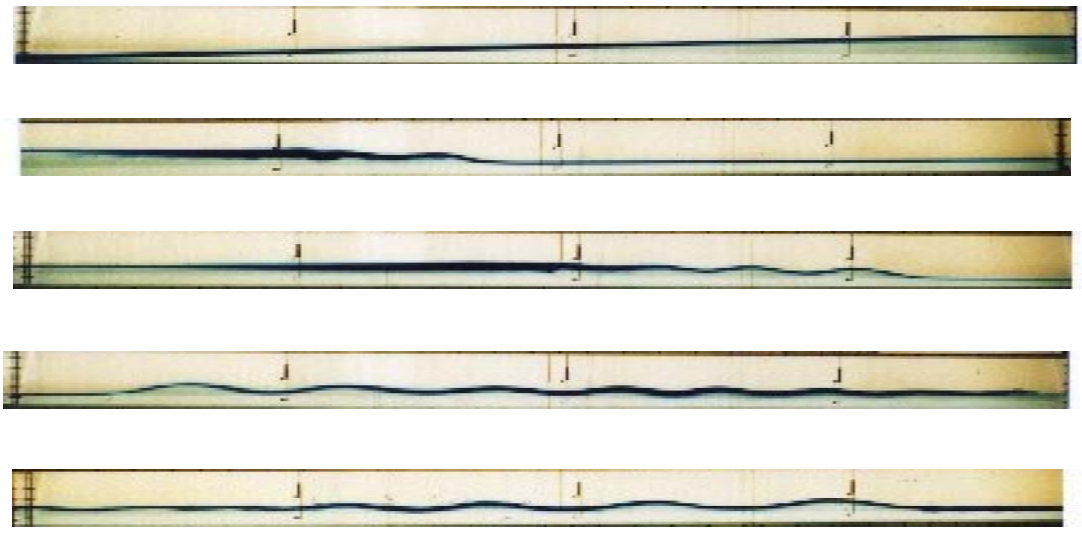

Figure 1.3: Laboratory experiment, conducted by Horn, et al. (2001), of a steepening, initial basin-scale wave that degenerates into a train of solitons. The first panel is the initial wave setup. The second panel shows the wave front steepening. The third panel shows the beginning of smaller waves developing behind the lead wave. The last two panels are the train of solitons traveling through the domain. The basin is 6m long and 0.29m high.

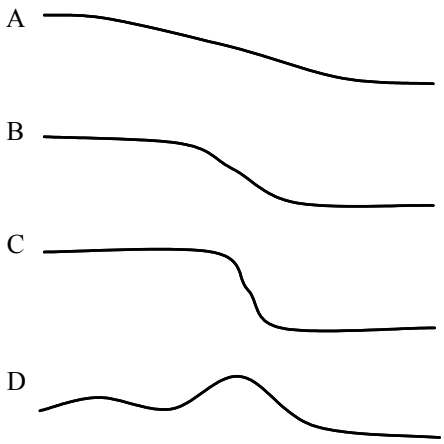

Figure 1.4: Cartoon of wave steepening and dispersion. A) An initial wave with a unique wave speed and amplitude. B&C) Wave steepening where the crest is moving faster than trough. D) Wave degeneration into a train of waves.

nonlinear acceleration and a dispersive force. The dispersive force that opposes nonlinear wave deformation is the non-hydrostatic pressure gradient. The dispersion of a wave leads to an energy cascade from an initial, low-frequency wave to a resulting, high frequency wave series that is more susceptible to wave breaking (van Haren, 2004). When non-hydrostatic pressure is not modeled while nonlinearities are modeled (i.e. typical of a hydrostatic model), there are two possible results. The first possibility is a wave steepens unabated and creates artificial mixing events through density overturns. The second possibility is a build up of numerical error that balances nonlinear steepening.

The two dominate forms of numerical error are numerical diffusion of mass (from herein called numerical diffusion) and numerical diffusion of momentum. The latter results in dissipation of energy and is henceforth called numerical dissipation. Numerical diffusion artificially weakens sharp gradients across the wave front. Thus, as a wave steepens, numerical diffusion increases and smoothes the wave front. This smoothing impedes wave steepening and reduces the available potential energy in wave, but increases the background potential energy of the system (Figure 1.5 A). The increase in background potential energy is seen in the thickening of the layer that contains the density gradient between the constant density upper and lower layer, which is called the pycnocline (see §2.2.1 for a description of available and background potential energy). Numerical dissipation has a similar effect in damping wave steepening. As a wave steepens, the velocity shear increases across the wave front, thereby increasing the artificial spreading of momentum through model error. The artificial spreading of momentum reduces the kinetic energy of the wave and inhibits steepening (Figure 1.5 B).

1.3.2 Modeling

Several hydrodynamic models for large-scale applications use the hydrostatic approximation (e.g. POM: Blumberg and Mellor, 1987; EFDC: Hamrick, 1992; ROMS: Haidvogel, et al., 2000). The hydrostatic approximation neglects non-hydrostatic pressure and vertical acceleration, but models

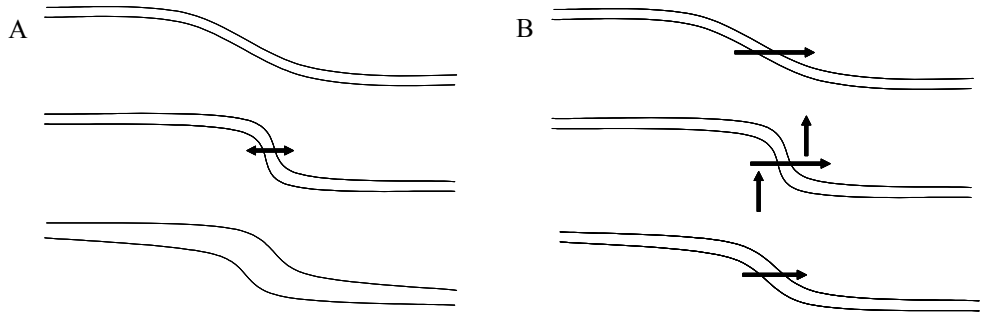

Figure 1.5: Cartoon of wave steepening. A) Nonlinear steepening wave with numerical diffusion. As the wave steepens, diffusion acts across the wave front and reduces the density gradient, available potential energy and steepness. B) Nonlinear wave steepening with numerical dissipation. The initial wave is primarily moving in a horizontal direction. As the wave steepens, the vertical velocities in front and behind the wave increase, increasing the shear. The increased diffusion of momentum (dissipation) reduces the wave's kinetic energy and limits the wave steepness.

nonlinear horizontal momentum. The hydrostatic approximation is generally applicable to processes with small aspect ratios (depth: length $\leq O[10^{-3}]$); for example, most large-scale ocean and atmospheric problems. However, the hydrostatic approximation breaks down for mesoscale systems [aspect ratio ~ $O(10^{-1} - 10^{-2})$] and small-scale events, such as the steepening and breaking of nonlinear internal waves (Kantha and Clayson, 2000a). Hydrostatic models often predict excessive steepening (Wadzuk and Hodges, 2003), which induces artificial breaking and diffusion, thereby developing a weakened pycnocline (Laval, et al., 2003). Hydrostatic models also show increased dissipation of internal wave energy which artificially reduces internal wave amplitude. Internal wave dispersion is not physically modeled in hydrostatic models (as it requires non-hydrostatic pressure), but may still appear as a numerical phenomenon in a simulated evolution (Hodges and Delavan, 2004). The aforementioned errors, which are all numerical, result in an incorrect evolution of an internal wave and its energy. Thus, the need for non-hydrostatic models is evident (Horn, et al., 2001; Laval, et al., 2003).

Several quasi-hydrostatic and non-hydrostatic models for large-scale systems have been developed (e.g. Mahadevan, et al., 1996a,b; Casulli and Stelling, 1998; Casulli, 1999; Fringer and Street, 2003). Despite this work, there has been little research on quantifying the timestep and spatial grid scales necessary to model non-hydrostatic behavior. The present research shows that a fine spatial and temporal resolution is needed to capture non-hydrostatic behavior (§4 ff.), thus significantly increasing computational time over hydrostatic models. The aforementioned models applied the non-hydrostatic model over the entire domain, but Stansby and Zhou (1998) recognized that non-hydrostatic effects are local and suggested application of the non-hydrostatic solution only in these limited areas. However, their work provides neither a method to locally solve the pressure, nor a method to locate regions where the non-hydrostatic pressure is important. The present research has developed a method to numerically identify regions with significant non-hydrostatic effect.

1.4 Approach

Achieving the objectives of this study required both hydrostatic and non-hydrostatic models. The University of Western Australia Centre for Water Research's Estuary and Lake Computer Model (CWR-ELCOM: Hodges, 2000) was used as the hydrostatic model. As part of this project, a non-hydrostatic pressure solver was developed as a modification to CWR-ELCOM. CWR-ELCOM is a three-dimensional hydrodynamic model that applies the incompressible, Boussinesq and hydrostatic approximations to solve the Euler equations on an Arakawa C staggered grid with a semi-implicit method and a moving free-surface. The model temporal accuracy is first-order for the flow field, third-order ULTIMATE-QUICKEST (Leonard, 1991) for scalar transport and first-order for the free surface. Surface thermodynamics are solved by bulk transfer models that are not used or investigated in this work. The Euler-Lagrange method for momentum is third-order spatially accurate, while spatial gradients in other terms are second-order. Details of the non-hydrostatic solver developed for the present research are described in §2 ff.

The existing and modified models were used to perform the analysis fulfilling the two research objectives. The first chapter of this document provides the reader with the motivation, objectives and background of this project. The second chapter provides the numerical methods applied in the hydrostatic model and the design of the non-hydrostatic solver, as well as the analytical methods used to quantify the performance of hydrostatic and non-hydrostatic models. The third chapter demonstrates the validation and verification of the non-hydrostatic solver. Chapter four uses the tools developed in chapter two to examine the first objective (comparing the differences between hydrostatic and non-hydrostatic models), including an evaluation of model skill on predicting internal wave evolution and quantification of numerical error. Chapter five develops and demonstrates a method to isolate non-hydrostatic effects. Chapter six concludes this work and makes suggestions for future work in this area of hydrodynamic modeling.

Chapter 2. Methods

Several different numerical and analytical methods are used in the present work to develop the models used in analysis and to provide a means to quantify and compare model results. Governing equations (§2.1.1) are used to model the physics of internal wave evolution and are applied to the numerical model with a pressure Poisson solution implemented by the fractional-step method described in §2.1.2 and §2.1.3. Along with the governing equations and numerical methods, a set of approximations and conditions are made to simplify the problem and provide boundaries for the solution space. In assessment of model skill, both qualitative and quantitative techniques are used. Section 2.2 provides qualitative methods for assessing model skill by examining the pycnocline displacement and quantitative methods for evaluating model skill through computing numerical dissipation and diffusion.

2.1 Numerical Model

This sections discusses a description of the governing equations of CWR-ELCOM and the non-hydrostatic solver and a justification for the inviscid approximation (§2.1.1). The methods used to develop the non-hydrostatics solver (§2.1.2 and §2.1.3) and the applicable boundary conditions (§2.1.4) are also described.

2.1.1 Governing Equations

The governing equations for the present research are the Euler equations, the free-surface equation with the kinematic boundary condition and the linear equation of state for density. In Cartesian tensor form, these are:

Incompressible momentum:

$$\frac{DU_i}{Dt} = -\delta_{i\alpha} g\left(\frac{\partial \eta}{\partial x_\alpha} + \frac{1}{\rho_o}\frac{\partial}{\partial x_\alpha}\int_{z'}^{\eta}\left(\tilde{\rho}\right)dz\right) - \frac{1}{\rho_o}\frac{\partial P_{nh}}{\partial x_i} \qquad (2.1)$$

Incompressible continuity:

$$\frac{\partial U_i}{\partial x_i} = 0 \qquad (2.2)$$

Free-surface – Kinematic boundary condition integrated over depth with continuity applied:

$$\frac{\partial \eta}{\partial t} = -\frac{\partial}{\partial x_\alpha}\int_b^{\eta} U_\alpha dz \qquad (2.3)$$

Density:

$$\rho = \rho_o\left(1+\beta S\right) \qquad (2.4)$$

In Equations (2.1) - (2.4), i = 1, 2, 3; α = 1, 2; U_i is the velocity; η is the free-surface elevation; z' is the vertical position in the water column; P_{nh} is the non-hydrostatic pressure; ρ is the density; ρ_o is the reference density; g is gravity. The haline expansion coefficient, β, is constant for a linear equation of state and S is salinity. The density can be decomposed as:

$$\rho = \rho_o + \tilde{\rho} \qquad (2.5)$$

where $\tilde{\rho}$ is a small departure from the reference density. When the hydrostatic approximation is used, as in CWR-ELCOM, the non-hydrostatic pressure gradient is neglected in Equation (2.1). Within the hydrostatic limit, vertical motions are assumed small (horizontal velocity ~ 10^{-1} ms^{-1}, vertical velocity ~ 10^{-4} to 10^{-5} ms^{-1}); therefore the vertical momentum equation is neglected (Cushman-Roisin, 1994). However, Long (1972) showed that the inclusion of vertical acceleration and non-hydrostatic pressure is necessary to properly model internal wave evolution. Thus, CWR-ELCOM has been modified as described in this chapter to include a non-hydrostatic pressure component based on Equation (2.1).

The present research's focus is on quantifying hydrostatic and non-hydrostatic models' ability to represent internal wave evolution and error accumulation. All analysis for the present research neglects viscous effects and diffusion terms in the momentum and transport equations for two reasons: 1) the effects of viscous damping and viscous effects in wave breaking are at the two extremes of wave phenomena, which are of lesser interest than the evolution of solitons; and 2) by neglecting viscosity and diffusion the dissipation of energy and diffusion of mass can be used to quantify numerical error. Viscous damping acts primarily through the wall boundary layers, which are not modeled in the present research, and the shear between density

layers. The viscous effect between density layers is immaterial in the present work as the timescale for damping is longer than the timescale for steepening, which is a phenomenon of interest for an evolving nonlinear wave. The modulus of decay provides the timescale for significance of viscous effects. This viscous timescale is the time it takes for a wave's amplitude to decrease to e^{-1} of its initial amplitude (Lamb, 1932):

$$\tau = \frac{\lambda^2}{8\pi^2 \nu} \qquad (2.6)$$

where τ is the modulus of decay, λ is wavelength and ν is viscosity. Figure 2.1 shows the modulus of decay for several different wavelengths. This viscous timescale is small for very short waves (e.g. capillary waves, Kinsman, 1965), so viscosity is important in their evolution and attenuation. Conversely, the viscous timescale for gravity waves (e.g. $\lambda >$ O[1m]) is long compared to the timescales of forcing and wave evolution (see discussion of wave steepening timescale, §3.3.3 ff.), so viscosity is insignificant for the evolution of longer waves. Viscous and diffusive effects in wave breaking and mixing are not of interest in the present work as large-scale coastal oceans and lake models do not have sufficient grid resolution to capture the details of these processes. The present research is focused on wave behavior prior to breaking, when the wave can be considered a smooth material surface that effectively suppresses turbulent diapycnal diffusion of mass and momentum.

λ (m)	τ (s)	τ (d)
10000	1.267E+12	1.466E+07
100	1.267E+08	1.466E+03
1	1.267E+04	1.466E-01
0.01	1.267E+00	1.466E-05

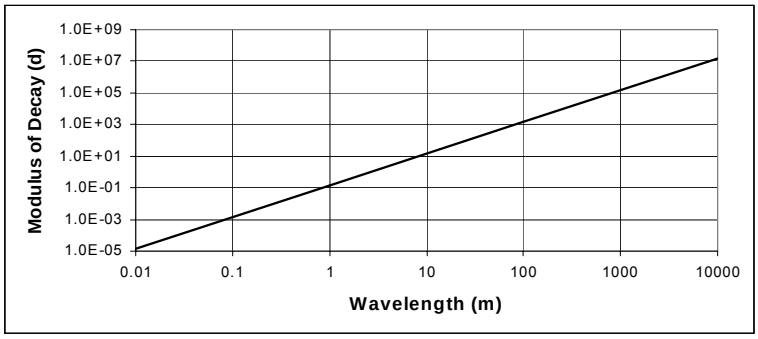

Figure 2.1: Modulus of decay for as a function of wavelength, determined from Equation (2.6). Viscosity is 10^{-6} m^2/s.

2.1.2 Solution Methods

The fractional step method (Kim and Moin, 1985) was used to incorporate the non-hydrostatic solver into the existing hydrostatic CWR-ELCOM. The fractional step method is mass conservative and has second-order temporal accuracy for 3D incompressible flows with fine spatial discretization and coarse temporal discretization (Casulli and Stelling, 1998; Casulli, 1999; Armfield and Street, 1999). The fractional step method can be outlined as follows:

- Solution of hydrostatic velocity field and free surface
- Solution of non-hydrostatic pressure
- Update of velocity field and free surface to reflect non-hydrostatic pressure.

The velocity field is initially approximated via a hydrostatic solution, providing U* and W*, as well as a hydrostatic free surface (η*).

$$U^*_{i+\frac{1}{2},k} = GU^n_{i+\frac{1}{2},k} - g\Delta t\left[\frac{\eta^*_{i+1} - \eta^*_i}{\Delta x_{i+\frac{1}{2},k}}\right] - g\Delta t\left[\frac{1}{\rho_o \Delta x_{i+\frac{1}{2},k}} \sum_b^{\eta}\left(\tilde{\rho}^n_{i+1,k} - \tilde{\rho}^n_{i,k}\right)\Delta z\right] \qquad (2.7)$$

$$W^*_{i,k+\frac{1}{2}} = GW^n_{i,k+\frac{1}{2}}$$

$$\eta^*_i = \eta^n_i - \frac{\Delta t}{\Delta x_{i,k}}\left(\sum_b^{\eta}\left(U^*_{i+\frac{1}{2},k} - U^*_{i-\frac{1}{2},k}\right)\Delta z_{i,k}\right)$$

where subscripts indicate the cell center (integers) and cell faces (fractions), as seen in Figure 2.2. The x-direction cell length is Δx_i, while $\Delta x_{i+1/2}$ is the cell center to center distance. The Lagrangian discretization of velocity from the Euler-Lagrange method is represented by GU^n, which uses a particle pathline in the time 'n' velocity field to estimate the Lagrangian momentum term at time 'n+1.' This method reduces the artificial damping associated with most low-order methods and can be applied to flows that have a Courant-Friedrich-Lewy (CFL) condition up to two (Hodges, 2000).

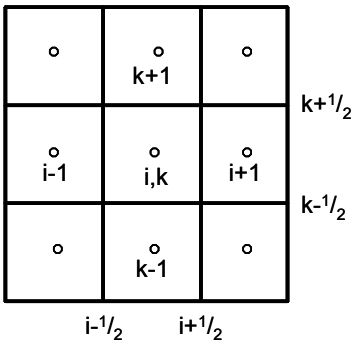

Figure 2.2: Schematic of grid field

The hydrostatic estimated velocity [Equation (2.7)] is subtracted from the discretized non-hydrostatic momentum equation, written as:

$$U_{i+½,k}^{n+1} = GU_{i+½,k}^{n} - g\Delta t\left[\frac{\eta_{i+1}^{n+1}-\eta_{i}^{n+1}}{\Delta x_{i+½,k}}\right] - g\Delta t\left[\frac{1}{\rho_o \Delta x_{i+½,k}}\sum_{b}^{\eta}\left(\tilde{\rho}_{i+1,k}^{n}-\tilde{\rho}_{i,k}^{n}\right)\Delta z\right] - \frac{\Delta t}{\rho_o}\left(\frac{P_{nh,i+1,k}^{n+1}-P_{nh,i,k}^{n+1}}{\Delta x_{i+½,k}}\right) \quad (2.8)$$

$$W_{i,k+½}^{n+1} = GW_{i,k+½}^{n} - \frac{\Delta t}{\rho_o}\left(\frac{P_{nh,i,k+1}^{n+1}-P_{nh,i,k}^{n+1}}{\Delta z_{i,k+½}}\right)$$

to obtain velocity correction equations:

$$U_{i+½,k}^{n+1} = U_{i+½,k}^{*} - \frac{\Delta t}{\rho_o}\left(\frac{P_{nh,i+1,k}^{n+1}-P_{nh,i,k}^{n+1}}{\Delta x_{i+½,k}}\right) \quad (2.9)$$

$$W_{i,k+½}^{n+1} = W_{i,k+½}^{*} - \frac{\Delta t}{\rho_o}\left(\frac{P_{nh,i,k+1}^{n+1}-P_{nh,i,k}^{n+1}}{\Delta z_{i,k+½}}\right) \quad (2.10)$$

The discrete form of continuity [Equation (2.2)] is:

$$\frac{U_{i+1,k}^{n+1}-U_{i,k}^{n+1}}{\Delta x_{i+½,k}} + \frac{W_{i,k+1}^{n+1}-W_{i,k}^{n+1}}{\Delta z_{i,k+½}} = 0 \quad (2.11)$$

which can be applied to the divergence of Equations (2.9) and (2.10) to yield a pressure Poisson equation (in Einstein summation):

$$\frac{\partial^2 P_{nh}}{\partial x_i \partial x_i} = \frac{\rho_o}{\Delta t}\frac{\partial U_i^{*}}{\partial x_i} \quad (2.12)$$

Equation (2.12) can be written discretely as:

$$\frac{1}{\Delta x_{i,k}}\left(\frac{P_{nh,i+1,k}^{n+1}-P_{nh,i,k}^{n+1}}{\Delta x_{i+½,k}} - \frac{P_{nh,i,k}^{n+1}-P_{nh,i-1,k}^{n+1}}{\Delta x_{i-½,k}}\right) + \frac{1}{\Delta z_{i,k}}\left(\frac{P_{nh,i,k+1}^{n+1}-P_{nh,i,k}^{n+1}}{\Delta z_{i,k+½}} - \frac{P_{nh,i,k}^{n+1}-P_{nh,i,k-1}^{n+1}}{\Delta z_{i,k-½}}\right) = \frac{\rho_o}{\Delta t}\left(\frac{U_{i+½,k}^{*}-U_{i-½,k}^{*}}{\Delta x_{i,k}} + \frac{W_{i,k+½}^{*}-W_{i,k}^{*}}{\Delta z_{i,k}}\right) \quad (2.13)$$

Solution of Equation (2.13) provides a non-hydrostatic pressure, $P_{nh,i,k}^{n+1}$, which is used to update the horizontal velocity field using Equation (2.9). The updated horizontal velocity field is used to update the free-surface:

$$\eta_{\alpha}^{n+1} = \eta_{\alpha}^{n} - \frac{\Delta t}{\Delta x_{\alpha}}\left(\sum_{k=b}^{\eta}\left(U_{\alpha+½,k}^{n+1}-U_{\alpha-½,k}^{n+1}\right)\Delta z_{\alpha,k}\right) \quad (2.14)$$

If Equation (2.10) is used to update the vertical velocity, the resulting velocity field may not be solenoidal due to the residual in the non-hydrostatic pressure solver. To ensure a solenoidal velocity field for mass transport, the vertical velocity is updated diagnostically from the continuity equation:

$$W_{i,k+½}^{n+1} = W_{i,k-½}^{n+1} - \left(\frac{U_{i+½,k}^{n+1}-U_{i-½,k}^{n+1}}{\Delta x_{i,k}}\right)\Delta z_{i,k} \quad (2.15)$$

The free-surface update [Equation (2.14)] has been treated differently in various models. The quasi-hydrostatic models of Mahadevan, et al. (1996a) and Casulli and Stelling (1998) solve only for the hydrostatic free-surface [Equation (2.7)] and do not account for non-hydrostatic effects on surface evolution. Casulli (1999) addressed this problem by correcting the surface elevation for the intermediate step [Equation (2.7)] and after the pressure Poisson equation was applied [Equation (2.14)]. The approach of Casulli (1999) was to advance the velocities, pressure and free-surface at time level 'n+1' while still applying the vertical discretization (Δz) of the previous time step (n). His approach removes a nonlinearity that arises when using inconsistent time discretization of 'Δz' and the free surface, which Hodges (2004) showed exists, but is second-order in time. Thus, the first-order temporal accuracy of CWR-ELCOM makes the inconsistency irrelevant and Casulli's (1999) treatment appropriate

for the updated free-surface. A more complex approach by Chen (2003) applies a double predictor-corrector method, updating the velocity first after the non-hydrostatic pressure is resolved and again after the free-surface is updated. The double predictor-corrector allows the non-hydrostatic change in the free-surface to alter the velocity field. While this method is second-order temporally accurate, Chen (2003) states that a comparison between the results with his method and those of Casulli (1999) show no significant improvement in model performance.

2.1.3 Iterative Methods – Pressure Poisson Equation

The pressure Poisson equation [Equation (2.13)] is an elliptic equation, which is inefficient for direct solution by matrix inversion (Mahadevan, et al., 1996a) and is therefore solved with iterative methods. Jacobi, Gauss-Seidel (GS), and successive over-relaxation (SOR) iterative methods were used in the development of the non-hydrostatic solver as a learning exercise for the author. The Jacobi and GS methods were impractical because of long convergence times (i.e. red-black point GS: ~3500 iterations for the L_∞ norm to converge to 10^{-8} in the manufactured solution case described in §3.1 ff). SOR, with a red-black point iteration scheme, has proved to have adequate convergence times (i.e. red-black point SOR: ~1000 iterations for the L_∞ norm to converge to 10^{-8}; this reduced the run time by about 70% for the manufactured solution case in §3.1 ff.). The SOR scheme used is presented in Equation (2.16) with the optimal over-relaxation factor (ψ) determined by Equation (2.17).

$$\begin{aligned} P_{nh,i,k}^{n+1} &= \psi\left(\frac{Q_{i,k}}{a_{i,k}}\right) + (1-\psi)P_{nh,i,k}^{n} \\ &\quad -\psi\left(\frac{a_{i+1,k}P_{nh,i+1,k}^{n+1} + a_{i-1,k}P_{nh,i-1,k}^{n+1}}{a_{i,k}}\right) \\ &\quad -\psi\left(\frac{a_{i,k+1}P_{nh,i,k+1}^{n+1} + a_{i,k-1}P_{nh,i,k-1}^{n+1}}{a_{i,k}}\right) \end{aligned} \tag{2.16}$$

$$\psi = \frac{2}{1+\sin\left(\frac{\pi}{\sqrt{N_g}}\right)} \tag{2.17}$$

where Q is the source term [i.e. the right hand side of Equation (2.13)], a is the coefficient that represents that spatial discretization and N_g is the number of grid cells in the computational domain.

Convergence was measured using by the residual (R):

$$\begin{aligned} R_{i,k} &= Q_{i,k} - a_{i+1,k}P_{nh,i+1,k}^{n+1} - a_{i-1,k}P_{nh,i-1,k}^{n+1} \\ &\quad - a_{i,k+1}P_{nh,i,k+1}^{n+1} - a_{i,k-1}P_{nh,i,k-1}^{n+1} - a_{i,k}P_{nh,i,k}^{n+1} \end{aligned} \tag{2.18}$$

When the residual is reduced to a specified convergence criteria (§3.1 ff), the non-hydrostatic pressure is considered resolved and the velocity field and free surface are updated with the new non-hydrostatic pressure. Other methods may be used to solve the pressure Poisson equation more efficiently (e.g. Mahadevan, et al., 1996b; Marshall, et al., 1997; Casulli and Stelling, 1999; Casulli, 1999; Fringer and Street, 2003). Some possibilities include the SOR applied in line-relaxation form, conjugate gradient method or multigrid methods. The multigrid method is well suited to handle stiff problems, such as the pressure Poisson equation, and it may use a Gauss-Seidel iterative scheme, so the non-hydrostatic solver could be adapted into multi-grid form. However, the multi-grid method may be difficult to implement over complex boundaries (He, et al., 1996).

2.1.4 Boundary Conditions

The model boundary conditions were assigned so that the vertical solid boundaries perfectly reflect wave propagation and neither vertical nor horizontal boundaries have viscous boundary layers. To achieve these requirements, the velocity is assigned Dirichlet conditions normal to solid boundaries (U = 0 or W = 0) and Neumann conditions tangential to solid boundaries (dU/dx = 0 or dW/dz = 0). Scalar quantities, including the non-hydrostatic pressure, have Neumann conditions (zero gradient) at all solid boundaries. The velocity and scalar conditions are implemented in CWR-ELCOM under the designation of "free-slip" boundaries. The non-hydrostatic pressure at the free surface is a Dirichlet condition requiring $P_{nh} = 0$. The boundary conditions for the non-hydrostatic pressure are built directly into the non-hydrostatic solver in the SOR coefficients, 'a,' in Equation (2.16).

2.2 Analysis Methods

Both qualitative and quantitative analysis methods are used to compare and contrast hydrostatic and non-hydrostatic model results. The simplest qualitative analysis is visual examination of internal wave evolution over several wave periods in both models and theory. The human eye/brain

combination is capable of distinguishing the overall scope of phase/amplitude errors in an intuitive way that provides the first level of screening for model results. Quantitative analysis methods developed herein are focused on the energy changes within the system. A principle reason for conducting model experiments using the inviscid/diffusionless equations is that any change in the modeled total energy (E_T) is directly attributable to numerical error. Therefore, energy changes are an integrator of numerical dissipation and diffusion errors in the model results. Furthermore, there is an energy shift to smaller wavelengths associated with the degeneration of an internal wave, which is used to identify numerical error.

2.2.1 Background

Total energy (E_T) in a system is comprised of kinetic (E_K) and potential energy (E_P), written below for a 2D system with a constant breadth (B):

$$E_K = \frac{1}{2}\int_0^L\int_b^\eta \rho U_i^2 B\, dz dx \qquad (2.19)$$

$$E_P = g\int_0^L\int_b^\eta \rho z B\, dz dx \qquad (2.20)$$

so that E_T may be written as:

$$E_T = E_K + E_P \qquad (2.21)$$

The potential energy can further be separated into background potential energy (E_B) and available potential energy (E_A) (Lorenz, 1955). The E_B is the potential energy when the system is at its lowest possible energy state. That is, if a system is adiabatically brought to rest and the density field settles without mixing, then the system is considered to have its lowest possible potential energy, which is E_B. The E_A is the potential energy of a system displaced from its lowest possible energy field, or also described as the E_P available to be transferred to E_K. Thus, the EA is defined as the difference between the E_P and E_B:

$$E_A \equiv E_P - E_B \qquad (2.22)$$

A simple monochromatic standing wave is an oscillatory exchange of E_A (the potential energy in the inclined wave) for E_K (kinetic energy when the wave is flat), and back to potential energy again. In an inviscid/diffusionless system, the exchange of E_A for E_K must be conservative, so it is convenient to define their sum as dynamic energy (E_D):

$$E_D \equiv E_A + E_K \qquad (2.23)$$

The relationship between energies is seen in Figure 2.3

Mass diffusion is the spreading, or weakening, of a stratified density field and is characterized by the increase in the background potential energy (E_B) as heavier particles are diffused upwards and lighter particles diffused downwards. Since E_B is the

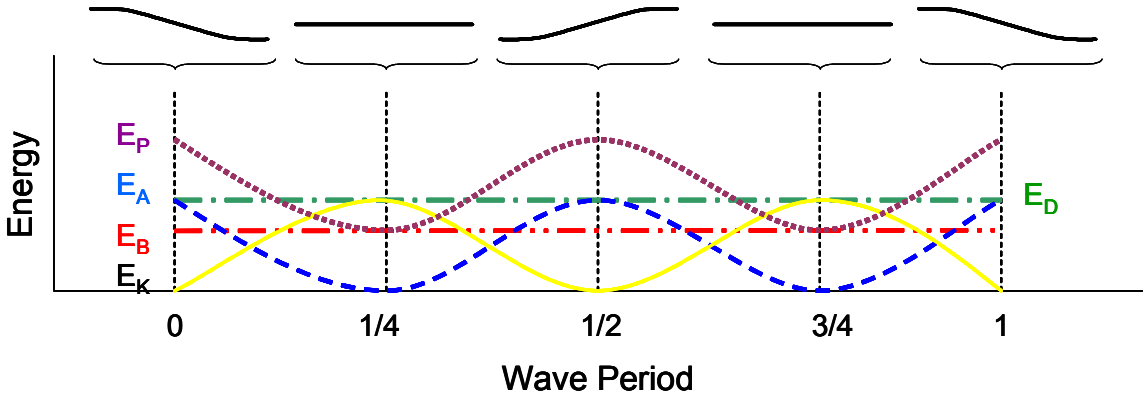

Figure 2.3: Schematic of energy behavior over a wave period, for a inviscid/diffusionless monochromatic standing wave. The black lines above the graph show the evolution of the wave shape. The purple (·····) line is the potential energy (E_P), the red (— · ·) line is the background potential energy (E_B), the blue (– –) line is the available potential energy (E_A), the yellow (——) line is the kinetic energy (E_K) and the green (— ·) line is dynamic energy (E_D). The E_P is the sum of E_B and E_A and the E_D is the sum of E_A and E_K.

density field when restored to its lowest energy state, it can only change through physical diffusion of the density gradient (Winters, et al., 1995). That is, advection and wave propagation can not directly increase EB. However, in the physical world they may cause shear instabilities and wave breaking which will more readily allow physical diffusion to occur.

Numerical diffusion of mass is indistinguishable from physical diffusion of mass in the resulting smoothing and spreading of gradients, which makes it difficult to quantify the numerical diffusion error when the governing equations include physical diffusion. In a model that sets physical diffusion to zero, any change in E_B is model error (Laval, et al., 2003), which is commonly referred to as numerical diffusion. Numerical diffusion is dependent on the coarseness of the grid; that is, fine grids reduce numerical diffusion (Hodges, et al., 2000). Thus, as a grid is refined and numerical diffusion is inhibited, modelers typically presume that model representation of E_B and internal wave evolution are improved; however, as shall be seen, this is not always true (§4 ff.).

In the physical world, dynamic energy (E_D) is decreased by: 1) transfer of available potential energy (E_A) and kinetic energy (E_K) to background potential energy (E_B) through turbulent mixing or 2) loss of E_K to heat through the action of viscosity. The latter is called "dissipation," while the former (mixing) is where waves and advection enhance the rate of physical diffusion. Shear instabilities and wave breaking move a fluid around, (i.e. 'stirring') which raises some of the heavy fluid, increasing E_A and decreasing E_K. If physical diffusion is present, a portion of the stirred fluid is irreversibly mixed. Thus, a portion of the E_K that went into E_A to stir the fluid is, in a sense, converted into E_B. Therefore, physical diffusion increases the E_B of a system while decreasing the E_D of the system. The portion of E_K lost due to diffusion is not considered dissipation of energy because the E_K was converted to E_B rather than heat. Without physical diffusion, stirred fluids cannot irreversibly 'mix' so the heavier fluid would eventually fall back to its lowest energy state, thereby converting the E_A back to E_K with no impact on E_B or E_D. Hence, in a diffusionless, inviscid model any decrease in E_D represents energy lost in the form of dissipation. As dissipation decreases E_K, there is less energy available for conversion to E_A and consequently a reduction in the E_D of a system.

The evolution of background potential energy (E_B) and dynamic energy (E_D) provide a measure of numerical diffusion and numerical dissipation. While the total potential energy for any particular density distribution is a relatively simple computation, the calculation of background potential energy is more difficult. Following the example of Winters, et al. (1995), an algorithm was developed to determine E_B, as described in Figure 2.4. The model approximates reality by assigning each cell in a system a unique value for density. By example, a 5×5 random domain would result in 25 layers in the resorted system, as in Figure 2.5.

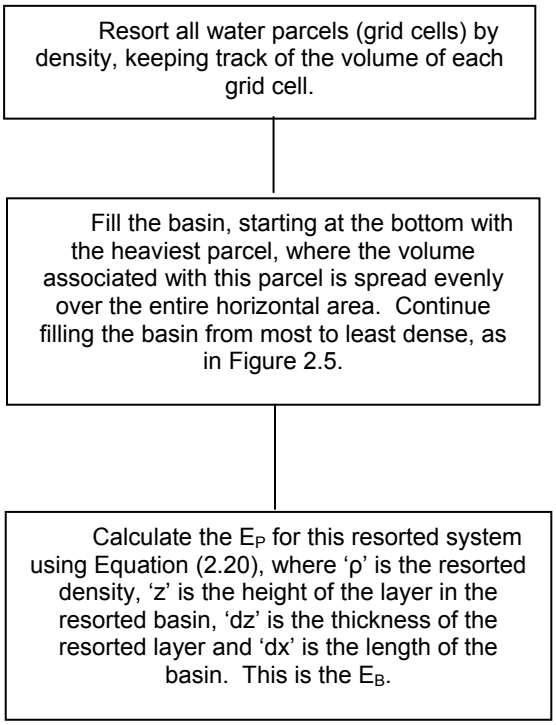

Figure 2.4: Flow chart of sorting algorithm for background potential energy (E_B).

Figure 2.5 provides a simple example, but a larger domain results in significantly more layers (i.e. 4380 for a 60×73 grid). The resorted density field yields a vertical resolution that has a much finer scale than the model's representation of the vertical processes. When the full resorted density field is used in calculations, the results are "noisy" and are a misleading representation of the model's resolvable vertical structure. To return the data to the appropriate analysis scale, the resorted density profile is "binned" into groups of densities to yield a resorted density domain that has the same number of layers as the original vertical resolution (Figure 2.6).

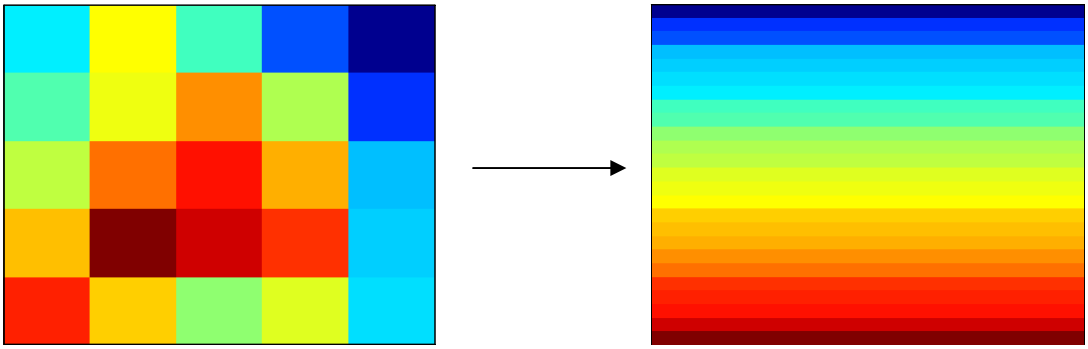

Figure 2.5: Schematic of a random 5×5 density field resorted into 25 layers from most to least dense. The blue indicates least dense and red indicates most dense.

The binned, resorted density field yields a domain that produces smoother calculations (Figure 2.7).

2.2.2 Numerical Diffusion

Physical diffusion changes stratification by smoothing density gradients transferring more dense fluid into lower density regions and vice-versa. Typically, changes in the background potential energy provide a measure of the physical diffusion in a system. In a diffusionless system, any changes in the stratification can be attributed to numerical diffusion. Therefore, changes in the background potential energy for a diffusionless system provide an estimate of numerical diffusion. Physical diffusion is modeled by diffusivity for each of the scalars, such as salinity or temperature. Thus, the concept of diffusivity is used to develop a numerical diffusion coefficient based on changes in the background potential energy. The numerical diffusion coefficient acts as a global parameter to compare model performance and error accumulation.

The resorted density field allows calculation of the E_B per unit area (A):

$$\frac{E_B(t)}{A} = \int_b^\eta \left[\rho_B(t,z)\,gz\right] dz \qquad (2.24)$$

where ρ_B is the binned, resorted density. The evolution of E_B is:

$$\frac{d}{dt}\left(\frac{E_B(t)}{A}\right) = \frac{d}{dt}\int_b^\eta \rho_B(t,z)\,gz\,dz \qquad (2.25)$$

The free surface for the background density field is constant in a system without inflows or outflows, so the derivative passes through the integral in Equation (2.25). Discretizing Equation (2.25) for 'N' layers yields:

$$\frac{d}{dt}\left(\frac{E_B(t)}{A}\right) = \sum_{k=1}^{N}\left\{\frac{d}{dt}\left[\rho_{B,k}(t,z_k)\,\Delta z_k\right]\right\} gz_k \qquad (2.26)$$

The density term for layer 'k' can be represented as:

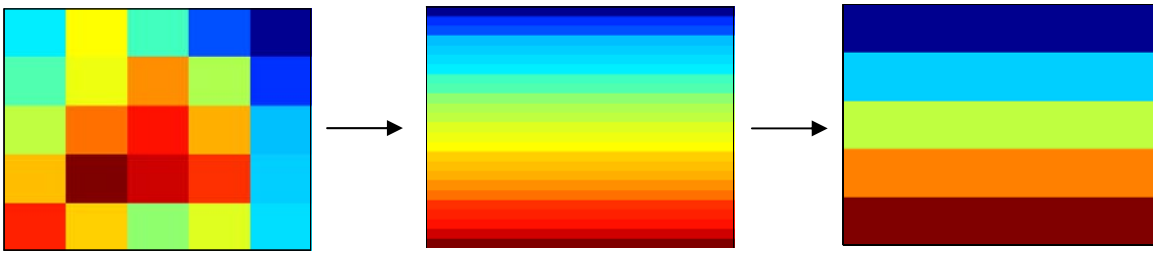

Figure 2.6: Schematic of a random 5×5 density field resorted into 25 layers from most to least dense and then binned into 5 layers. The blue indicates least dense and red indicates most dense.

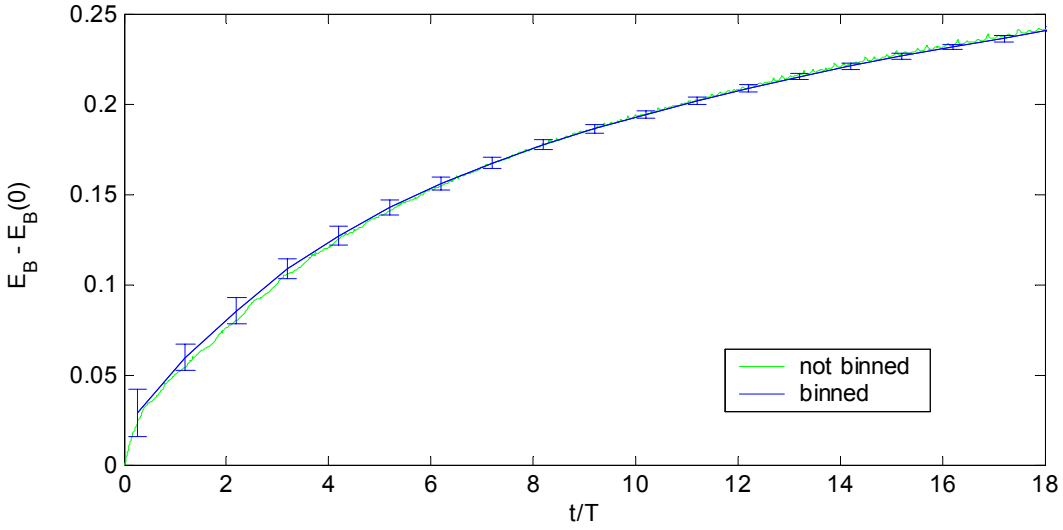

Figure 2.7: Typical change in background potential energy (units: Joules) versus the time normalized by a wave period (T). The green line is before the density field is binned, the blue line is after the density field is binned, with the errorbars representing the standard deviation.

$$\begin{aligned}\frac{d}{dt}\left[\rho_{B,k}(t,z_k)\Delta z_k\right] &= \frac{d}{dt}\left\{\frac{m_B(t,z_k)}{A\Delta z_k}\Delta z_k\right\}\\ &= \frac{1}{A}\frac{d}{dt}\left[m_B(t,z_k)\right]\\ &= \frac{\dot{m}_B(t,z_k)}{A}\end{aligned} \qquad (2.27)$$

where $\rho = m/\forall$ and $\forall = A\Delta z$ with Δz_k constant in time. The vertical mass flux, $\dot{m}_B$, represents the rate of change in the resorted density field; any change in E_B is due only to the diffusion of mass in the density stratified system. The relationship in Equation (2.27) can be substituted into Equation (2.26) to obtain:

$$\frac{d}{dt}\left(\frac{E_B(t)}{A}\right) = \sum_{k=1}^{N}\frac{\dot{m}_B(t,z_k)}{A}gz_k \qquad (2.28)$$

Fick's law states:

$$q = -D\frac{\partial C}{\partial z} \qquad (2.29)$$

where D is the diffusion coefficient, q is the mass flux per unit area and C is the mass concentration. The vertical mass flux per unit area in Equation (2.28) may be expressed in the form of Fick's law:

$$\frac{\dot{m}_B(z)}{A} = -D(z)\frac{\partial\rho(z)}{\partial z} \qquad (2.30)$$

Making the substitution for the vertical mass flux per unit area into Equation (2.28), yields

$$\frac{d}{dt}\left(\frac{E_B(t)}{A}\right) = \sum_{k=1}^{N} -D_k g z_k \frac{\partial\rho_B(t,z_k)}{\partial z} \qquad (2.31)$$

which can be redefined as

$$F = \sum_{k=1}^{N}\sigma_k D_k \qquad (2.32)$$

where

$$\begin{aligned}F &= \frac{d}{dt}\left(\frac{E_B(t)}{A}\right)\\ \sigma_k &= -gz_k\frac{\partial\rho_B(t,z_k)}{\partial z}\end{aligned} \qquad (2.33)$$

F is computed from model results using the rate of change of E_B and σ is computed from the resorted density profiles. Local diffusion coefficients (D_k) cannot be directly computed from the global change in E_B in Equation (2.32). However, we can estimate an approximate global diffusivity based on a simplified treatment of the density field. In all the present investigations, hyperbolic tangents are used to construct the density field:

$$\rho = \rho_{base} + \frac{1}{2}\Delta\rho_{py}\tanh\left\{\frac{e^{1}\left[z_{py} + \eta\cos\left(\pi\frac{x}{L}\right) - z\right]}{\frac{h_{py}}{2}}\right\} \tag{2.34}$$

where ρ_{base} is the density at the center of the pycnocline, $\Delta\rho_{py}$ is the density change across the pycnocline, η is the amplitude, x is the horizontal grid location, L is the length of the basin, z is the vertical grid location and h_{py} is the thickness of the pycnocline. The height at the center of the pycnocline is z_{py} and the initial thickness (h_{py}) is split equally on each side of the pycnocline center line to designate the initial pycnocline position. Equation (2.34) yields a representative density profile (Figure 2.8). The hyperbolic tangent profile models a continuous stratification in a real world system with three distinct layers; two approximately uniform density layers separated by a region of rapidly changing density. Therefore, dividing a stratified system into three layers: 1 = upper, 2 = pycnocline and 3 = lower (Figure 2.8); Equation (2.32) can be written

$$\sigma_1 D_1 + \sigma_2 D_2 + \sigma_3 D_3 = F \tag{2.35}$$

The upper and lower layers have approximately constant density, so $\sigma_1 = \sigma_2 = 0$, which leaves

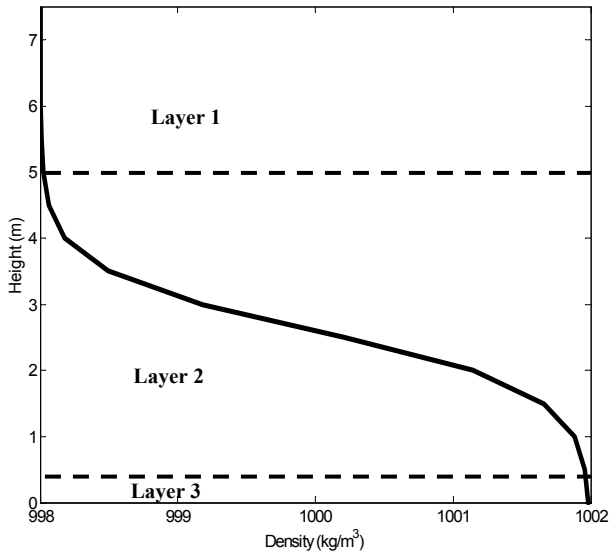

Figure 2.8: Typical density profile constructed by a hyperbolic-tangent function. The dashed lines separate layers 1, 2 and 3.

$$D_2 = \frac{F}{\sigma_2} = -\frac{\frac{d}{dt}\left(\frac{E_B(t)}{A}\right)}{gz_k\frac{\partial\rho_2}{\partial z}} \tag{2.36}$$

Equation (2.36) can be approximated as

$$D_2 \approx -\frac{\frac{d}{dt}\left(\frac{E_B(t)}{A}\right)}{gz_{py}\left(\frac{\rho_1 - \rho_3}{h_{py}}\right)} \tag{2.37}$$

where ρ_1 and ρ_3 are the densities of the upper and lower layers, respectively. Equation (2.37) yields a global approximation for D across the pycnocline derived from the change in the background potential energy system and changes in the pycnocline thickness and density field. This approximation provides a tool with which numerical diffusion can be estimated for the simple three-layer system. Since this approximation is taken at each time step there is the possibility of oscillations due to small-scale anti-diffusive fluxes. The small-scale anti-diffusive fluxes arise from non-monotonic advection (Leonard, 1991). Oscillations form around sharp wave fronts (i.e. a discontinuity) and are referred to as Gibb's phenomenon (Kreyszig, 1999). The transport algorithm used in the present research is ULTIMATE QUICKEST; ULTIMATE (Leonard, 1991) smoothes the oscillations in QUICKEST (Leonard, 1979) so that the scalar concentration decreases monotonically in a one-dimensional system. Lin and Falconer (1997) found that ULTIMATE QUICKEST is not monotonic for a two-dimensional system, such as used in the present research.

Model performance over multiple wave periods is the focus of this work; thus, the change in E_B and the pycnocline density gradient are binned over a wave period to smooth anti-diffusive fluxes and provide a clear indication of numerical diffusion. The average form of Equation (2.37) is

$$\overline{D_2} = -\frac{\frac{1}{\Delta T}\int_T \frac{d}{dt}\left(\frac{E_B(t)}{A}\right)dt}{\frac{1}{\Delta T}\int_T gz_{py}\left(\frac{\rho_1 - \rho_3}{h_{py}}\right)dt} \tag{2.38}$$

where T is the wave period. The change in h_{py} is slow if the upper and lower layer densities remain

constant and the pycnocline has not diffused over the entire water column (Figure 2.9). With this assumption, Equation (2.38) can be discretized as

$$\overline{D_2}\left(T_{n-\frac{1}{2}}\right) = -\frac{\frac{1}{A\Delta T_{n-\frac{1}{2}}}\left\{\overline{E_B\left(T_n\right)} - \overline{E_B\left(T_{n-1}\right)}\right\}}{g\overline{z_{py}}\left(\frac{\overline{\rho_1} - \overline{\rho_3}}{\overline{h_{py}}}\right)} \tag{2.39}$$

where the over bar represents the binned data over a wave period.

2.2.3 Numerical Dissipation

Energy dissipation in a physical fluid is controlled by molecular viscosity acting at the smallest scales of velocity shear. However, the energy at the smallest scales of motion is fed by the larger scales of motion (Kantha and Clayson, 2000b; Kundu and Cohen, 2002), so the larger scales are considered to be the energy-containing scales and control the rate at which viscosity can work. In modeling, turbulence is commonly discussed in terms of the eddy viscosity associated with a large-scale velocity shear, so that the eddy viscosity characterizes the enhancement of turbulent dissipation for the large-scale features. The concept of eddy viscosity is well-entrenched in our understanding of dissipative phenomenon, so it is useful to develop a measure of a numerical viscosity associated with the dissipation by numerical error.

The mechanical energy dissipation rate, typically presented on a unit mass basis (ε), (Batchelor, 1967) in a 2D, incompressible fluid is

$$\varepsilon = \nu\left[\left(\frac{\partial u}{\partial z} + \frac{\partial w}{\partial x}\right)^2 + 2\left(\frac{\partial u}{\partial x}\right)^2 + 2\left(\frac{\partial w}{\partial z}\right)^2\right] \tag{2.40}$$

In a diffusionless system, the dissipation rate, integrated over a volume, is equivalent to the rate of change of the E_D.

$$\begin{aligned}\frac{dE_D}{dt} &= \int_{\forall} \rho\varepsilon\, d\forall \\ &= \int_{\forall} \left(\rho_o + \tilde{\rho}\right)\nu\left[\left(\frac{\partial u}{\partial z} + \frac{\partial w}{\partial x}\right)^2 + 2\left(\frac{\partial u}{\partial x}\right)^2 + 2\left(\frac{\partial w}{\partial z}\right)^2\right] d\forall\end{aligned} \tag{2.41}$$

Since $\tilde{\rho} \ll \rho$, the density perturbation from the reference density ($\tilde{\rho}$) can be neglected, yielding

$$\frac{dE_D}{dt} \approx \int_{\forall} \rho_o \nu\left[\left(\frac{\partial u}{\partial z} + \frac{\partial w}{\partial x}\right)^2 + 2\left(\frac{\partial u}{\partial x}\right)^2 + 2\left(\frac{\partial w}{\partial z}\right)^2\right] d\forall \tag{2.42}$$

The principle velocity shear (and hence numerical dissipation) occurs across the pycnocline. A characteristic numerical viscosity associated with numerical dissipation is developed that is consistent with the shear characteristics in the pycnocline. Integrating Equation (2.42) over the volume of the pycnocline and substituting the characteristic numerical viscosity of the pycnocline (ν_{py}) for the molecular viscosity (ν) yields:

$$\frac{dE_D}{dt} \approx \rho_o \nu_{py}\left[\left\langle\left(\frac{\partial u}{\partial z} + \frac{\partial w}{\partial x}\right)^2\right\rangle + \left\langle 2\left(\frac{\partial u}{\partial x}\right)^2\right\rangle + \left\langle 2\left(\frac{\partial w}{\partial z}\right)^2\right\rangle\right]\forall_{py} \tag{2.43}$$

where $\langle\ \rangle$ represents a spatial mean. If the pycnocline volume ($\forall_{py}$) is characterized by horizontal area (A) and pycnocline thickness (h_{py})

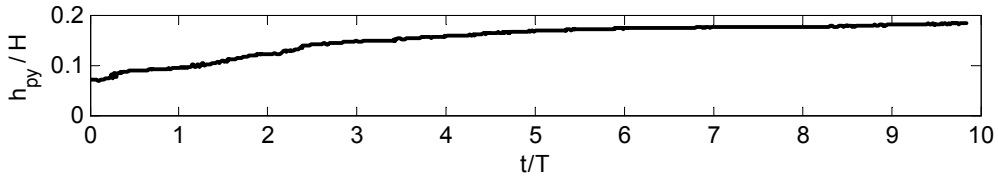

Figure 2.9: Typical change in pycnocline thickness (normalized by total depth, H) over time (normalized by the wave period, T). This case was scenario 2 for the 30×73 grid (§3.3).

then numerical viscosity, binned over a wave period, may be approximated as

$$\nu_{py} = \frac{1}{\Delta T_{n-½}}\left[\overline{E_D(T_{n+1})} - \overline{E_D(T_n)}\right] \times \left\{\rho_o A h_{py}\left[\overline{\left\langle\left(\frac{\partial u}{\partial z}+\frac{\partial w}{\partial x}\right)^2\right\rangle} + \overline{\left\langle 2\left(\frac{\partial u}{\partial x}\right)^2\right\rangle} + \overline{\left\langle 2\left(\frac{\partial w}{\partial z}\right)^2\right\rangle}\right]\right\}^{-1} \tag{2.44}$$

where an overbar represents the binned data over the wave period. For internal waves, the dominant velocity gradient is $\partial u/\partial z$, so Equation (2.44) can be reasonably reduced to

$$\nu_{py} = \frac{1}{\Delta T_{n-½}}\left[\overline{E_D(T_{n+1})} - \overline{E_D(T_n)}\right] \times \left\{\rho_o A h_{py}\left[\overline{\left\langle\left(\frac{\partial u}{\partial z}\right)^2\right\rangle}\right]\right\}^{-1} \tag{2.45}$$

Equation (2.45) provides an approximation for the numerical viscosity in the model, which is used to compare the relative importance of numerical viscosity with molecular viscosity.

2.2.4 Spectral Analysis

As modeled internal waves evolve, dynamic energy is transferred to smaller scale waves or lost to numerical error. The computation of numerical viscosity (§2.2.3) allows quantification of the energy dissipated. In this section we discuss how spectral analysis is used to quantify the transfer of energy into shorter wavelength features.

Spectral analysis describes the distribution of signal power over wave frequencies (or wavenumbers). For this work, the spectral analysis decomposes the spatial structure of pycnocline displacement into the power spectral density associated with different wavenumbers ($k = 2\pi/\lambda$). A Matlab® toolbox function (i.e. "pwelch") was used to obtain the power spectral density. Welch's method is used, which is outlined in the following steps: 1) the data is divided into overlapping segments, 2) a Hamming window is used to calculate the modified periodogram for each segment and 3) the modified periodograms are averaged to obtain the estimated power spectral density for the entire data set (Signal Processing Toolbox User's Guide, 1998). A small data set may reduce the resolution of the power spectral density estimation, thus the data set is replicated to create a longer data set (i.e. in this work, the replicated data set is used to include basin-scale waves). For all analysis in this work, the signal data is divided into eight segments with 50% overlap between adjacent segments and a Hamming window applied on each segment, 32 replicates of the initial half wavelength wave are used (to total 16 wavelengths). The power spectral density is computed at each binned period for all wavelengths, thus the data set is sampled at $2\pi/\Delta x$, which corresponds to wavenumber.

As an internal wave steepens and forms solitons, the initial long-wavelength wave evolves into a train of short-wavelength waves. The power spectral analysis provides the power distribution of the internal wave over different wavenumbers. As a wave evolves, an energy shift may occur, transferring energy from the long-wavelength wave to smaller-wavelength waves. For instance, the peak energy at time = 0 coincides with the initial, long-wavelength wave. However, as the wave evolves and dynamic energy (E_D) decreases, there is an energy transfer through different wavelength waves, which appears as a shift in the peak power wavenumber through time. The shift in peak power should coincide with the development of solitons. If a wave does not degenerate into solitons, the peak power should remain with the initial, long-wavelength wave. If a bore develops, then there may be a shift in peak power as the bore provides higher wavenumber components since the wave is no longer sinusoidal. Comparing expected wave behavior with the spectral analysis provides an assessment of model skill, in terms of the model's ability to represent soliton formation and the evolution of model error.

Chapter 3. Verification and validation of the non-hydrostatic solver

Verification and validation of a computer code are two necessary and basic steps to demonstrate that the code does what it is intended to do. According to Roache (2002), code verification is an evaluation of error from a known solution, a purely mathematical exercise, while code validation demonstrates the accuracy with which the mathematical model captures the physical phenomena based on theory or measured in the field or laboratory. This chapter verifies the non-hydrostatic pressure solver with an analytical solution, validates the solver's convergence with a simple test case and validates the model's solution against theory and a laboratory experiment.

3.1 Verification by the Method of Manufactured Solutions

The purpose of the manufactured solution is to verify the model's accuracy and establish the convergence criterion for the numerical model used in this work.

3.1.1 Setup

Roache (2002) suggests using the "Method of Manufactured Solutions" to verify a numerical code. This method uses a continuous mathematical solution independent of the code. The manufactured solution must be non-trivial and should exercise all terms in the numerical code and the corresponding boundary conditions. The manufactured solution is applied to the numerical model's homogeneous governing equations, producing a non-homogeneous source term that is discretized and added to the numerical model's governing equations; the resulting discrete non-homogeneous governing equations are used to approximate the exact manufactured solution. This study uses a manufactured two-dimensional analytical solution:

$$P = \cos(x)\cos(z) \tag{3.1}$$

Figure 3.1 shows the solution for Equation (3.1). The pressure Poisson equation has the form

$$\frac{\partial^2 P}{\partial x^2} + \frac{\partial^2 P}{\partial z^2} = Q \tag{3.2}$$

The second derivative of Equation (3.1) is:

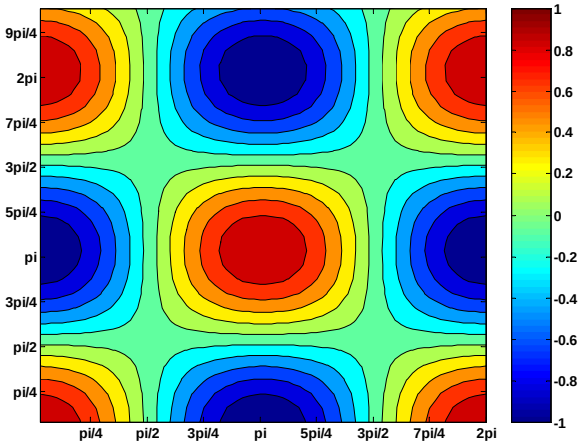

Figure 3.1: Solution space for the manufactured solution. The colorbar represents pressure in kg/ms^2.

$$\frac{\partial^2 P}{\partial x^2} = -\cos(x)\cos(z)$$
$$\frac{\partial^2 P}{\partial z^2} = -\cos(x)\cos(z) \tag{3.3}$$

This produces a manufactured source term:

$$Q = -2\cos(x)\cos(z) \tag{3.4}$$

which is used as the discrete source term for the non-hydrostatic solver [e.g. the right hand side of Equation (2.13)] to compute the discrete pressure field of the manufactured solution. Thus, the manufactured solution provides a known solution space which can be compared to the model's solution driven by the source term, Equation (3.4). This approach allows verification of model performance for different spatial grids and time steps.

The verification test domain is a square box, 2π m in length and 7.5 m in height, represented by four different grids, as described in Table 3.1. The boundary conditions of the manufactured solution are the same pressure boundary conditions used in other simulations within the present research (§2.1.4); the domain top (free-surface) has a Dirichlet boundary condition, while all other sides (solid boundaries) have Neumann boundary conditions.

3.1.2 Error Analysis

It is necessary to examine the grid convergence error to assess the model's accuracy at different grid

Table 3.1: Grids used in the manufactured solution (§3.1).

Case	Grid (nx × nz)
A	10 × 10
B	20 × 20
C	40 × 40
D	41 × 30

resolutions. Following Roy (2003), grid convergence error is analyzed using the L_1 and L_2 spatial error norms. The spatial error norms consider the entire domain to estimate the order of accuracy of the model.

As defined by Roy (2003), the discretization error at grid point (x,z):

$$\varepsilon_D(x,z) = P_{grid}(x,z) - P_{exact}(x,z) \qquad (3.5)$$

is used in the L_1 and L_2 spatial error norms:

$$L_1\ \text{norm}_\varepsilon = \frac{\sum_{n=1}^{N_{grid}} |\varepsilon_D(x,z)|}{N_{grid}}$$

$$L_2\ \text{norm}_\varepsilon = \left(\frac{\sum_{n=1}^{N_{grid}} |\varepsilon_D(x,z)|^2}{N_{grid}} \right)^{1/2} \qquad (3.6)$$

where N_{grid} is the number of grid points in the computational domain. Figure 3.2 shows the L_1 and L_2 spatial error norms. The three different grids used (Table 3.1 cases A - C) were refined in both the horizontal and vertical direction. As the grid is refined, the spatial error norms decrease with second-order behavior, verifying that the non-hydrostatic solver is spatially second-order accurate.

In real world problems, analytical solutions typically do not exist. Another way to look at error is the residual [from Equation (3.2)]:

$$R(x,z) \equiv Q(x,z) - \frac{\partial^2 P_{grid}(x,z)}{\partial x^2} - \frac{\partial^2 P_{grid}(x,z)}{\partial z^2} \qquad (3.7)$$

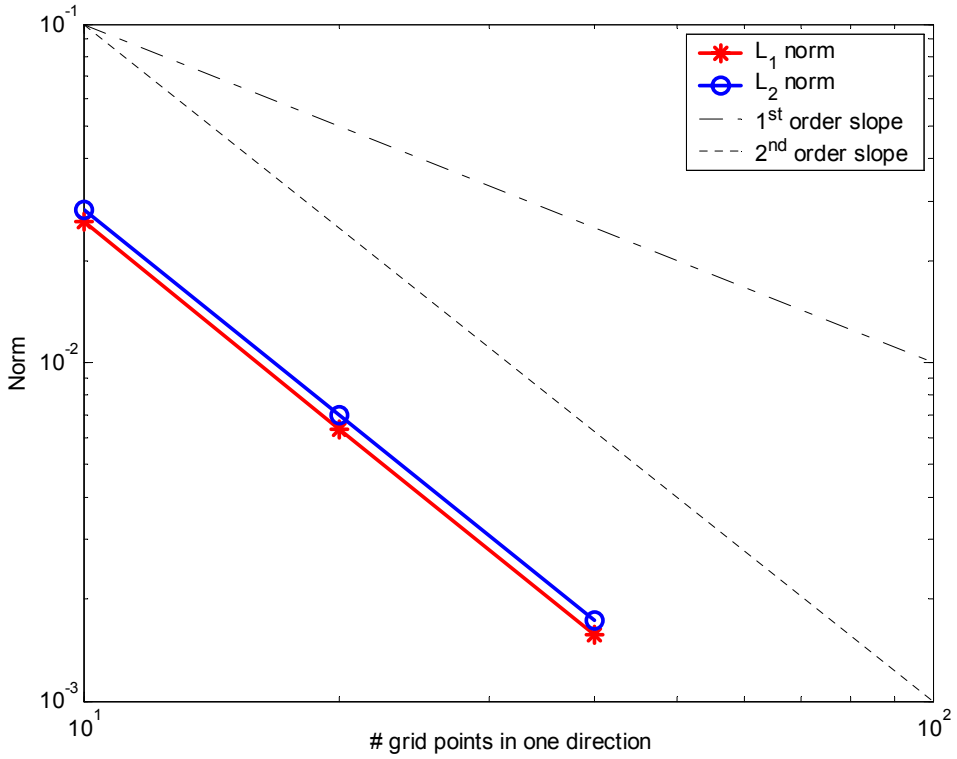

Figure 3.2: The L_1 and L_2 spatial error norms of the manufactured solution for grid refinement (Table 3.1 cases A – C).

The L_1, L_2 and L_∞ residual norms are then defined:

$$L_1 \text{ norm}_R = \frac{\sum_{n=1}^{N_{grid}} \left| R_{grid}(x,z) \right|}{N_{grid}}$$

$$L_2 \text{ norm}_R = \left(\frac{\sum_{n=1}^{N_{grid}} \left| R_{grid}(x,z) \right|^2}{N_{grid}} \right)^{1/2} \qquad (3.8)$$

$$L_\infty \text{ norm}_R = \max \left| R_{grid}(x,z) \right|$$

Figure 3.3 shows the L_1, L_2 and L_∞ residual norms for increasing number of iterations that the non-hydrostatic solver performs for the manufactured solution. This iteration count is equivalent to the number of iterations per timestep of the pressure solution in an unsteady problem (§3.2).

The change in residual norms with number of iterations measures the model's evolution towards convergence for a specific amount of computational effort. The norms continue to decrease with increasing number of iterations until the residual calculation [Equation (3.7)] reaches machine accuracy. However, the solution at machine accuracy will differ from the analytical solution by the truncation error in the discrete equations (Hirsch, 1988). Convergence is defined when the norms decrease by a specified order of magnitude. Hirsch (1988) gives the example of, "a second-order accurate space discretization, with $\Delta x = 10^{-2}$, will produce an error of the order of 10^{-4} on the solution, which cannot be reduced further even if the residual equals 10^{-14}." Thus, for second-order discretization of the non-hydrostatic solver, the solution is considered converged when the L_∞ residual norm decreases by four orders of magnitude. The

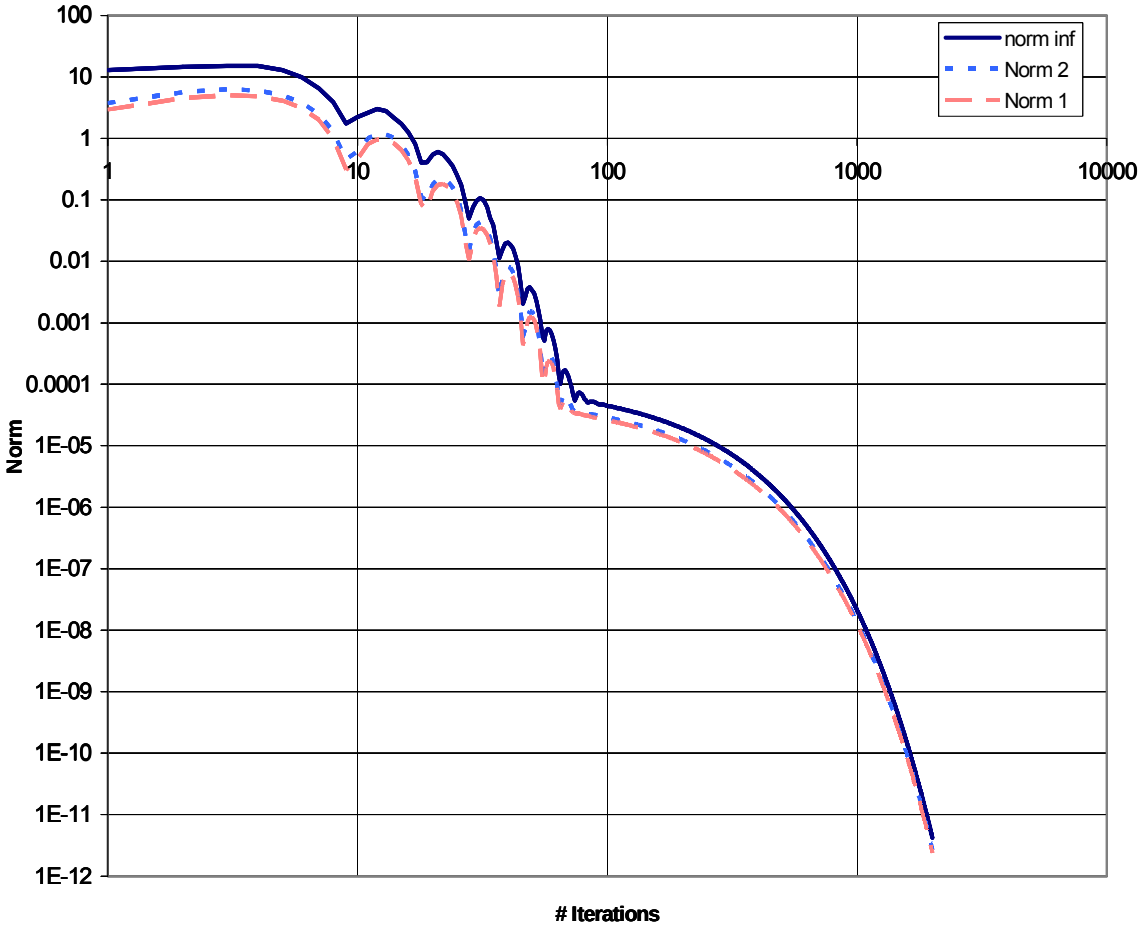

Figure 3.3: Residual norms for manufactured solution (case D, Table 3.1). Solid blue line is L_∞ norm, dotted blue line is L_2 norm and dashed red line is L_1 norm. The number of iterations are the number of iterations the non-hydrostatic solver performs per timestep.

manufactured solution drops by four orders of magnitude (Figure 3.3) in about 50 iterations. Figure 3.4 shows the comparison of L_∞ spatial error and error norms. The L_∞ spatial error norm flattens at the same number of iterations (~50) where the L_∞ residual norm has decreased by four orders of magnitude. Thus, the L_∞ residual norm can be used to reasonably represent the error when it is not possible to calculate the L_∞ spatial error norm (i.e. where there is no analytical solution).

In summary, applying the non-hydrostatic solver to the manufactured solution shows that as the grid is refined, the error decreases and the computed solution converges to the manufactured solution. The spatial error norms verify that the method is second-order accurate. The residual norms are a good proxy for the spatial error norms when an analytical solution is not available. Thus, the L_∞ residual norm is used to establish the convergence criterion in the above verification of the non-hydrostatic solver; which is the reduction of the L_∞ residual norm by four orders of magnitude. This convergence criterion is used in all further model simulations.

3.2 Validation and Convergence for an Unsteady Internal Wave

The purpose of this test case is to determine the number of iterations to reach a converged solution (i.e. based on §3.1) in an unsteady internal wave. This test case is sufficiently simple, yet exemplifies many of the nuances of internal wave modeling.

3.2.1 Setup

The validation test basin used was 10 m long and 7.5 m deep. The initial wave was a cosine wave with amplitude of 1.125 m, where the upper layer depth to total depth ratio was 0.3. A hyperbolic tangent function [Equation (2.34)] was used to construct the

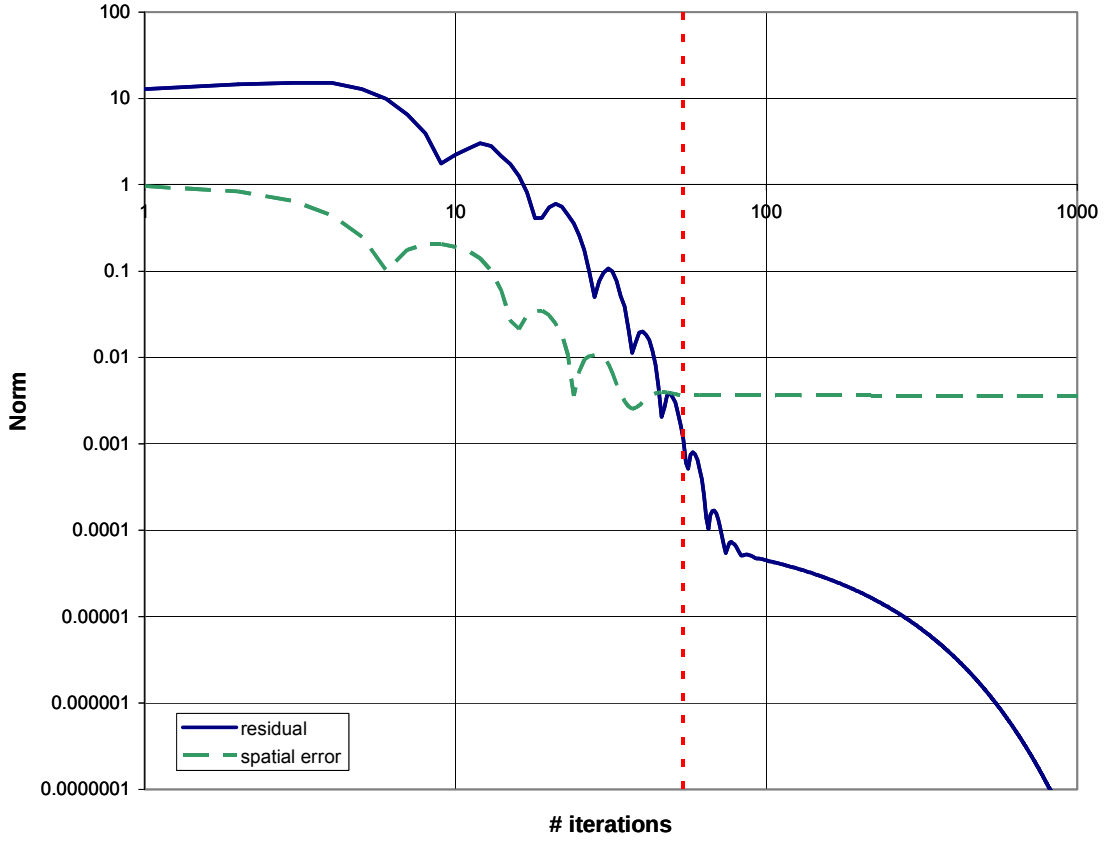

Figure 3.4: Spatial error and residual L_∞ norms for manufactured solution for case D. The red dotted line is where the L_∞ residual norm decreases by four orders of magnitude (i.e. the convergence criterion). The number of iterations are the number of iterations the non-hydrostatic solver performs per timestep.

density profile (Figure 2.8). The test basin's density profile has an initial pycnocline that is 5m thick with a density change of 4 kg/m^3. A square grid of 0.25 m * 0.25 m was applied to this domain.

3.2.2 Results

Akin to the manufactured solution in §3.1, the L_1, L_2 and L_∞ residual norms for the internal wave test case decrease with increasing number of iterations that the non-hydrostatic solver performs within each timestep of the simulation (Figure 3.5). However, the decrease in convergence is slower than the manufactured solution (Figure 3.6). The L_∞ residual norm decreases by four orders of magnitude in about 50 iterations for the manufactured solution case, while the L_∞ residual norm decreases by the same amount in about 180 iterations for the internal wave test case. The longer convergence time for the test case compared to that of the manufactured solution is discussed in §6.

The estimated root mean square error is used to evaluate the density field for the different number of iterations that the non-hydrostatic solver performs per timestep. The estimated RMS error compares the difference in density at each grid cell within the pycnocline between a simulation with 1000 iterations, which is considered the converged case, against simulations with a lesser number of iterations (i.e. 10, 50, 75, 100, 200 and 500). The estimated root mean square error (ε_{RMS}) of the density field is:

$$\frac{\varepsilon_{RMS}(k)}{\Delta\rho_{py}} = \left(\frac{\sum_{n=1}^{N_{grid}} \left| \rho_{k,n} - \rho_{1000,n} \right|^2}{N_{grid}} \right)^{1/2} \qquad (3.9)$$

where k is different numbers of iterations the non-hydrostatic solver performs per timestep and $\Delta\rho_{py}$ is the density change across the pycnocline. The estimated RMS error is computed only within the pycnocline (e.g. layer 2 in Figure 2.8) because layers 1 and 3 are essentially uniform density. The pycnocline is defined by the region where there is rapid change in the density profile (e.g. Figure 2.8,

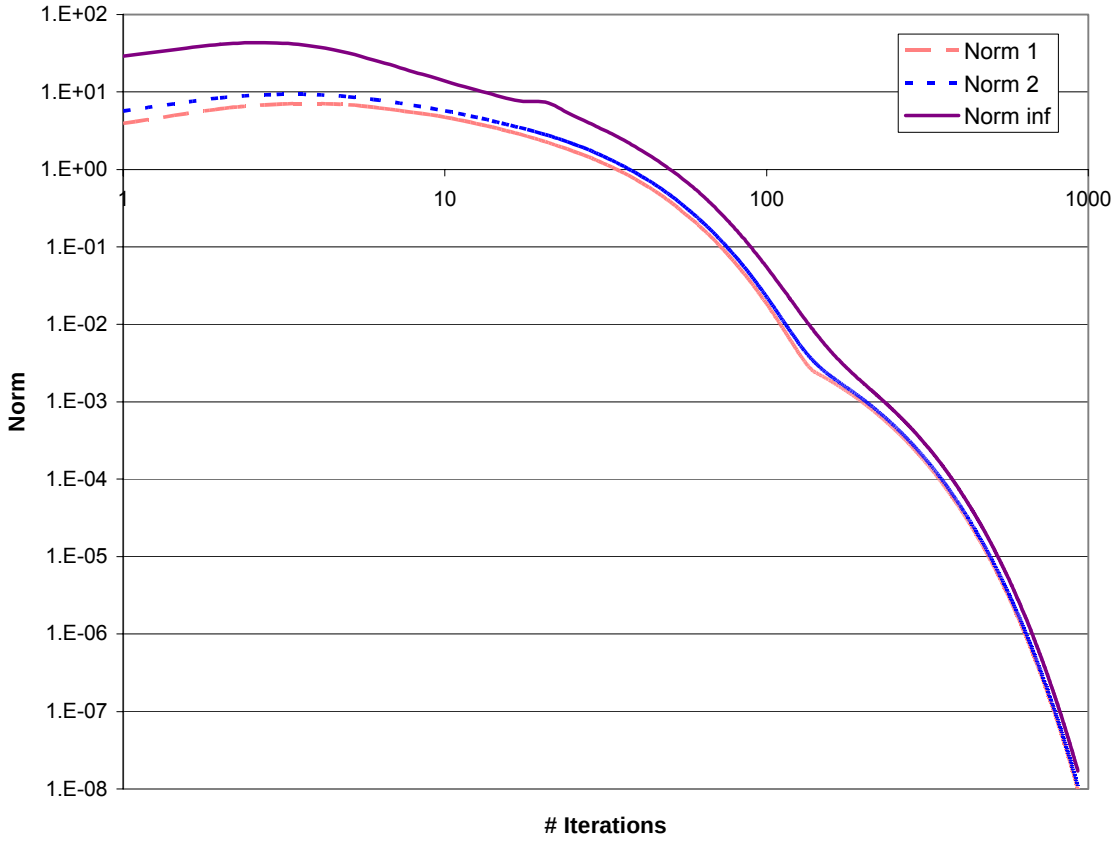

Figure 3.5: Residual norms for the internal wave test case. The solid purple line is the L_∞ norm, the dotted blue line is the L_2 norm and the dashed red line is the L_1 norm. The number of iterations are the number of iterations the non-hydrostatic solver performs per timestep.

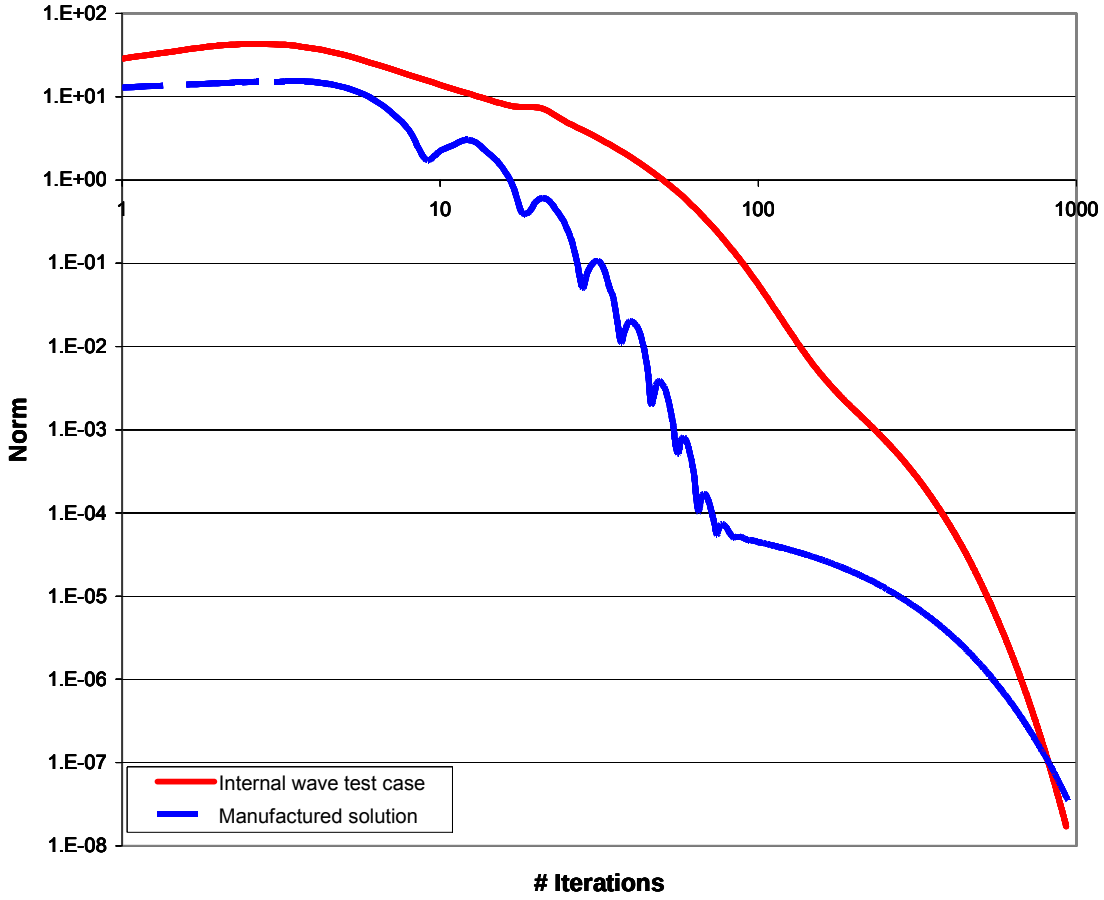

Figure 3.6: L_∞ norm for the manufactured solution (case D, dashed blue line) and the internal wave test case (solid red line). The number of iterations are the number of iterations the non-hydrostatic solver performs per timestep.

the pycnocline is demarcated between 998.1 kg/m^3 and 1001.9 kg/m^3). The RMS error is normalized by the density change across the pycnocline (e.g. in this case, 3.8 kg/m^3). Figure 3.7 shows the RMS error values for the six different non-hydrostatic solver iterations per timestep (i.e. 10, 50, 75, 100, 200 and 500). Using 200 iterations per timestep, the RMS error is one or more order of magnitude smaller than the 10, 50, 75 and 100 iteration cases. After the initial growth in the first 200 timesteps, the error growth rate for the 200 iteration case [$O(10^{-5})$ in 800 timesteps] is slower than the growth for cases with less iterations [i.e. the 100 iteration case grows to $O(10^{-3})$ in 800 timesteps]. Of course, the RMS error at 200 iterations is larger than the 500 iteration case, but using 500 iterations increases the computational time (200 iterations: 0.61 s/timestep; 500 iterations: 0.75 s/timestep) without necessarily improving the model results. That is, as discussed in §3.1.2, the solution cannot reduce the error below truncation as iterations are increased past the convergence criterion (decrease in L_∞ residual norm by four orders of magnitude) (Hirsch, 1988). At 200 iterations, the L_∞ residual norm has decreased by four orders of magnitude, so any further decrease in the L_∞ residual norm provided by increasing the number of non-hydrostatic solver iterations per timestep is unnecessary. This estimated RMS error analysis supports the findings from the norm analysis in Figure 3.5.

The non-hydrostatic pressure solution requires more computational time. For example, on a Dell Workstation PWS530 Xeon Processor with a 2.4 GHz CPU and 3.5 GB of RAM, the hydrostatic model takes 0.31 seconds/timestep, while the non-hydrostatic model takes 0.66 seconds/timestep for

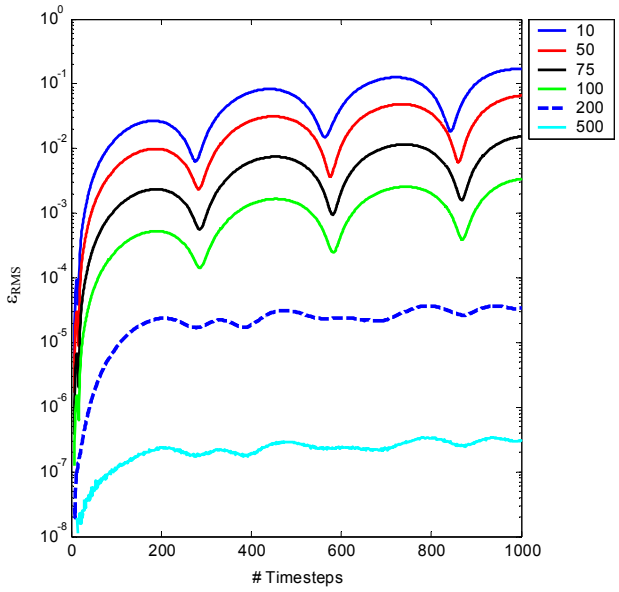

Figure 3.7: Root mean square error (ε_{RMS}) for density field in the test case. Each line represents the ε_{RMS} for a different number of iterations per timestep. The density range is 3.8 kg/m^3.

the same timestep and grid resolution where the convergence criteria of the non-hydrostatic solver is reducing the L_∞ norm by four orders of magnitude; for a grid with 60 horizontal grid cells × 73 vertical grid cells (0.01 m horizontal resolution × 0.004 m vertical resolution) and a timestep of 0.012 seconds, simulating 10 wave periods requires 90000 timestep iterations, the hydrostatic model takes 7.9 hours, while the non-hydrostatic model takes 16.4 hours. However, the above mechanics understates the scope of the problem: as discussed in §4 ff., the non-hydrostatic model requires a finer timestep and spatial resolution than the hydrostatic model to capture the resolvable processes, therefore a more meaningful comparison is the computational time required for a coarse-resolution hydrostatic model to a fine resolution non-hydrostatic model. While the choice of the coarse-resolution grid is somewhat arbitrary, for illustration we might consider a hydrostatic solution on a 30 × 73 grid on the same problem, with a 0.2 s time step and 1800 timestep iterations. The resulting solution time is 0.09 hours (5.5 minutes). With this example, the difference in computational expense between the hydrostatic and non-hydrostatic models is evident; the spatial and temporal requirements of the non-hydrostatic model, combined with the pressure Poisson solution, render it a huge computational undertaking. The solution of the pressure Poisson equation accounts for 89% of the increase in simulation time. Updating the velocity and free-surface field increases the simulation time by 10%. The above discussion is for a two-dimensional solution; a three-dimensional solution may further increase the difference in computational effort.

The pressure Poisson equation estimates the pressure at a point using the pressure from the surrounding cells. Other non-hydrostatic models (e.g. Marshall, et al., 1997; Casulli, 1999) use the pressure from time 'n' as the initial estimate of the pressure field for time 'n+1,' however the present research found that the time 'n' pressure may be a poor approximation for the time 'n+1' pressure field due to the internal wave propagation (§6.1 ff.). Setting the pressure field to zero at each timestep provides a pressure Poisson solution that converges faster than solution with the previous timestep's pressure field (Figure 3.8).

3.3 Validation Against Regime Theory and Laboratory Experiment

This section compares the numerical model's representation of internal wave evolution to the evolution of several laboratory-scale internal waves and theoretical wave evolution.

3.3.1 Regime Theory

Horn, et al. (2001; herein referred to as Horn) compared internal wave evolution in a laboratory experiment with four theoretical timescales of different internal wave phenomena: 1) damping, 2) steepening, 3) shear instability (Kelvin-Helmholtz billow formation) and 4) internal bore formations. The theoretical timescales are a function of the basin and internal wave dimensions, such as length, height and amplitude; Figure 3.9 shows a schematic of a basin. From the theoretical timescales, Horn developed a regime diagram (e.g. Figure 3.10) that uses the theoretical timescales to determine the prevailing wave phenomena under different conditions. Horn tested and validated the theoretical regimes in a laboratory experiment.

Regime diagrams based on the timescales provide the boundaries between damping, steepening into solitons, and formation of Kelvin-Helmholtz billows or undular bores. A single "universal" regime diagram (i.e. for all waves) cannot be drawn as the regime boundaries are functions of wave amplitude, upper layer thickness, total depth, basin

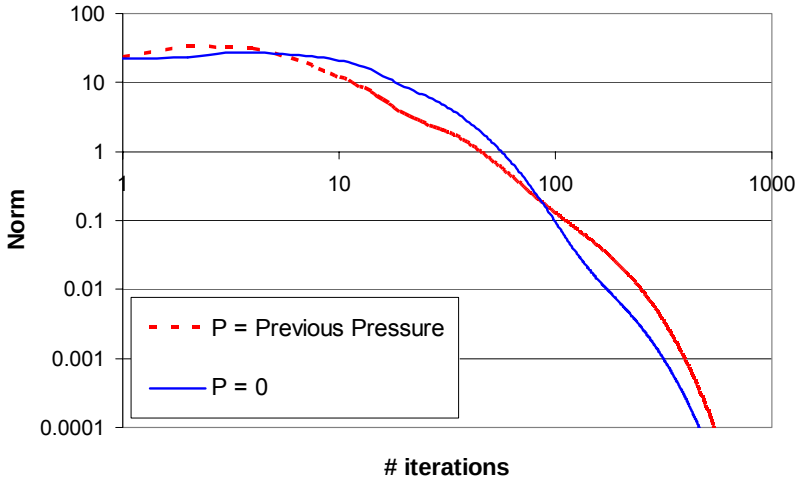

Figure 3.8: L_∞ norm for the non-hydrostatic solver when the pressure at the present timestep is approximated from zero (solid blue line) and the previous timesteps solution (dashed red line).

length, pycnocline thickness, and the density change across the pycnocline. While there are many possible ways to graph this multidimensional data set, Horn showed that a graph of wave amplitude to upper layer depth ratio (a/h) and upper layer depth to total depth ratio (h/H) provides a clear delineation of the timescales and regimes. Figure 3.10 is an example of a regime diagram for the basin used in Horn's experiments.

As discussed in Horn, Regime 1 in Figure 3.10 is the region where viscous damping dominates nonlinear steepening, typically for internal waves with small amplitudes. Regime 2 is where nonlinear steepening is dominant and solitons are formed. Regime 2 flows have been observed many times in different field studies (e.g. Boegman, et al., 2003; Farmer, 1978; Wiegand and Carmack, 1986). Regime 3 is supercritical flow, with large wave amplitudes and a shallow pycnocline, which are associated with internal hydraulic jumps and internal bores. Regime 4 physics are dominated by Kelvin-Helmholtz billows, which predominantly occur in shallow systems with deep pycnoclines; they are a result of shear instabilities at the interface between layers. Regime 5 physics are characterized by large amplitude internal waves that develop into bores and may include Kelvin-Helmholtz billows. Waves developing in the high-mixing regimes 3, 4 and 5 (supercritical flow, Kelvin-Helmholtz billows and bores) have the onset of principle phenomena occurring within one-quarter of the wave period, while the wave evolution in regimes 1 and 2 (damping and soliton formation) typically requires one or more wave periods to significantly affect the wave characteristics. Horn's regime diagram provides a framework to validate the non-hydrostatic solver. Simulation experiments were performed for several scenarios corresponding to the different regimes.

3.3.2 Horn's Laboratory Experiment and Model Simulations

The dimensions of Horn's laboratory experiment were used for a series of model simulations: length (L) = 6 m, height (H) = 0.29 m and width = 0.3 m (Figure 3.9). The regime diagram in Figure 3.10 is defined for the above scales. Horn's experimental basin is a closed system, with solid boundaries on all sides and the top. The present model is designed

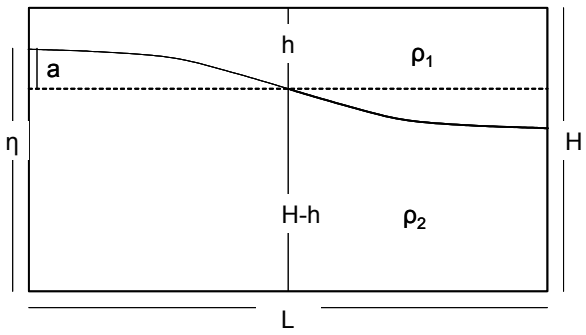

Figure 3.9: Schematic of basin.

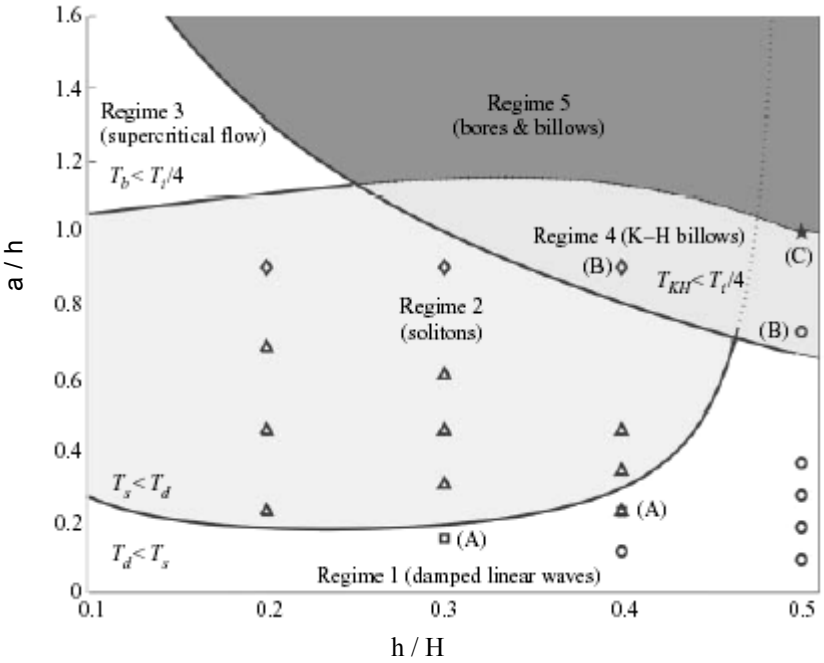

Figure 3.10: The regime boundaries from laboratory experiments; ordinate: amplitude-upper layer depth ratio, abscissa: upper layer depth-total depth ratio. A typical interface thickness, 1 cm, was used to determine the timescales, T_{KH} and Td. The star represents Kelvin-Helmholtz billows and bore, the diamond is the broken undular bore, the triangle is the solitons, the square is steepening, and the circle is damped linear waves. (from Horn, et al, 2001)

only for free-surface simulations, so this is one area where the model and experimental conditions diverge. However, the free-surface remains essentially flat (maximum displacement of 0.001 m) as the initial conditions are an entirely baroclinic flow, which has no significant coupling to the free surface (Kantha and Clayson, 2000b). The model boundary conditions are as described in §2.1.4. The model viscosity is set to zero, which is a second area where the model and experimental conditions diverge. However, as discussed in §2.1.1, this only effects the damping rate of modeled waves at fine grid scales when the numerical dissipation is less than the physical dissipation. Thus, it can be expected that the model may show development of solitons (regime 2) under conditions when Horn's experiments show damped linear waves. Modeling the viscosity in Horn's experiment is impractical as the principle viscous damping in the experiment is not the shear across the wave interface, but is the boundary layers on the sides and top of the tank. Modeling the drag of these boundary layers is impractical with the present model and of little relevance to the present subject of interest.

Horn's experiments were set up in a tilted tank with two fluids of different density. The density difference between the two layers was 20 kg/m^3 across a pycnocline thickness of 0.01 to 0.02 m. The tilted tank was quickly moved to a horizontal position to initialize the wave. This impulsive start creates an initial condition that is approximately a linear tilt. Model simulations of Horn's experiments are initialized with a cosine wave having an amplitude that corresponds to the tank's initial angle of tilt in Horn's experiment. The difference in initial wave setup is the third area of divergence between the model simulation and the laboratory experiment. However, this difference is not expected to affect the wave evolution. A three layer hyperbolic tangent salinity profile [Equation (2.34)] was used to establish the initial density profile that is close to Horn's condition (Figure 3.11).

Nine scenarios were modeled to reproduce some of Horn's experiments, as shown in Table 3.2; these scenarios were chosen based on Horn's reported results (see Horn, et al., 2001 Figures 5 and 6). These scenarios exemplify the influence of nonlinearity, and the subsequent development non-

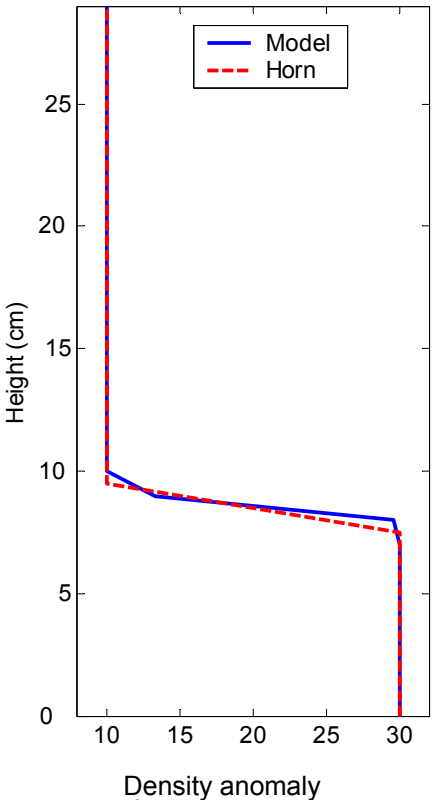

Figure 3.11: Initial density profile for Horn's laboratory experiment (red, dashed line) and the modeled hyperbolic tangent density profile.

hydrostatic pressure gradients, on internal wave evolution. Group A maintains the same depth ratio (h/H) and varies the amplitude ratio (a/h) to illustrate the relationship between nonlinearity and initial wave amplitude. Group B changes the depth ratio and amplitude ratio. Changing the depth ratio also influences the nonlinearity of the system; that is, as the depth ratio decreases, the nonlinearity increases. Scenarios 6 and 9 have a depth ratio of 0.5. At this depth ratio, the wave is considered weakly nonlinear. Therefore nonlinear steepening and soliton formation are not significant wave evolutions. Scenario 6 has a small amplitude ratio (a/h = 0.18), so the expected phenomenon is a damped wave. Scenario 9 has a large amplitude ratio (a/h = 1.0) and Kelvin-Helmholtz billows are expected to form.

3.3.3 Results

Horn's raw data was not available for numerical comparisons, so qualitative comparisons are made to figures from Horn, et al. (2001). Specifically, the model simulations are compared qualitatively against Horn's laboratory experiment to demonstrate the model's ability to capture soliton development in Figures 3.12 - 3.14. The model is compared to the experimental results by comparing the evolution of pycnocline displacement at a point in the tank; the amplitude of the wave and solitons, time of emergence of solitons and number of solitons within a wave series are the three major points of comparison.

Before a discussion of the model and laboratory results, it is necessary to review the principal difference between the model simulations and Horn's experiments; that is the neglect of viscosity in the model simulations. The experimental tank is narrow and has a lid, so there is significant area (i.e. the surface area of the interface is 1.8 m^2 and the surface area of the tank is 3.8 m^2) that creates a viscous boundary layer which will dominate the wave damping. The computational domain in the model simulations is the same size, but the boundary layers are not modeled. Without viscosity, the model simulations have no physical damping to restrain wave steepening. The model does have numerical dissipation which may cause some damping, however, the numerical viscosity due to numerical dissipation is less than molecular viscosity for the wave periods up to the emergence of solitons (§4.1 ff.). Therefore, as steepening is occurring, the wave experiences negligible damping, so the modeled wave tends to develop solitons sooner and with greater amplitudes than in the experiments with viscous effects.

Wave Evolution

Interfacial displacement can be used as a measure of wave evolution. The interfacial vertical

Table 3.2: Scenarios used in the laboratory-scale case (§3.3)

	Scenario	h/H	a/h
Group A	1	0.30	0.15
	2	0.30	0.30
	3	0.30	0.45
	4	0.30	0.60
	5	0.30	0.90
Group B	6	0.50	0.18
	7	0.40	0.23
	2	0.30	0.30
	8	0.20	0.45
	9	0.50	1.00

displacement recorded by the central wavegauge in Horn's tank is used to compare the laboratory data to the isopycnal displacement in the center of the model domain. Figure 3.12 shows the model and Horn's results for group A (§3.3.2., Table 3.2). In general, the model matches the qualitative evolution of wave phenomena and the period of the waves, but over-predicts the wave amplitude. This is consistent with comparing an inviscid model to a laboratory experiment with viscous fluid. There tends to be one less soliton in the wave series in the model simulations than in the laboratory experiments; this will be discussed later in this section.

Scenario 1 is within regime 1 where the dominating wave behavior is viscous damped waves. Physical viscous damping is not present and the damping due to numerical dissipation is less than physical damping. Therefore, it is expected that modeled waves within regime 1 will have less damping (i.e. these wave will have slightly larger 'bumps' develop) than in the laboratory experiment; this is seen in a comparison of scenario 1 between the model simulation and Horn's experiment.

Scenarios 2-4 are in regime 2 with soliton development, which the model represents, showing the leading wave with the largest amplitude and each successive wave in the train with smaller amplitudes. The model results qualitatively follow Horn's trend of more rapid soliton formation with increasing nonlinearity.

Scenario 5 is in regime 2 and should theoretically steepen and develop solitons, however Horn observed a broken undular bore in the leading wave (Figure 3.12). The wave evolution, as described by the model simulation, shows bore development (Figure 3.15), but the breaking described by Horn is not observed. While detailed data on the breaking phenomena were not reported by Horn, it is likely their spatial scales are too fine to be captured in the present model. Behind the bore, the model shows soliton formation, which is also indicated in Horn's results. The model simulation for scenario 5 shows slightly fewer solitons in the wave series than Horn's experiment.

The model results for group B (§3.3.2., Table 3.2) show the same characteristics observed by Horn: the nonlinearity of internal wave evolution increases as the amplitude ratio (a/h) increases and as the depth ratio (h/H) decreases (Figure 3.13). With increased nonlinearity, non-hydrostatic pressure effects increase, which allows the non-hydrostatic model simulations to depict soliton formation. Without the non-hydrostatic pressure, the modeled evolution of the wave is quite different (§4 ff.). Similar to the results for group A, the model simulations of group B generally match the qualitative evolution of wave phenomena and the period of the waves seen in Horn's laboratory experiment. The wave amplitude is over-predicted in the model simulations.

Scenario 9 has a large amplitude ratio (1.0) and is on the boundary between Kelvin-Helmholtz billows (regime 4) and bore formation (regime 5). The timescale for Kelvin-Helmholtz formation is 13 s and the timescale for bore formation is exactly one quarter of the wave period (25 s). Bores and Kelvin-Helmholtz billows form when their respective timescales are less than one quarter of the wave period (Horn, et al. 2001). For this scenario, Kelvin-Helmholtz billows were observed by Horn, while the model simulation showed the wave degenerate into a system of higher mode waves (Figure 3.16). Kelvin-Helmholtz billows are a fine-scale phenomenon, which require a small grid resolution to model them. The grid scale (60×73) used may be too coarse horizontally to capture this event.

Emergence of Solitons

A critical point of comparison is the emergence of solitons. Horn defines the emergence of solitons as, "… the time when the waves are sufficiently well separated that the depth (measured from the crest of the leading wave) of the trough between the leading solitons (measured from the crest of the leading wave) is 25% of the amplitude of the leading wave" (Horn, et al., 2001). Horn used three wavegauges spaced approximately 1.5 m apart. As solitons may have emerged between wavegauges, Horn reports the time it took for the wave to move between the wavegauge that showed solitons and the upstream wavegauge. Horn's definition and method of soliton emergence was used to identify the emergence of solitons for the model simulations. The period of the emergence of solitons for Horn's experiments and model simulations is seen in Figures 3.12 and 3.13.

Horn defines the timescale of steepening as:

$$T_s = \frac{L}{\alpha\eta} \tag{3.10}$$

where L is the basin length, η is the amplitude and

$$\alpha = \frac{3}{2} c \frac{h_1 - h_2}{h_1 h_2} \tag{3.11}$$

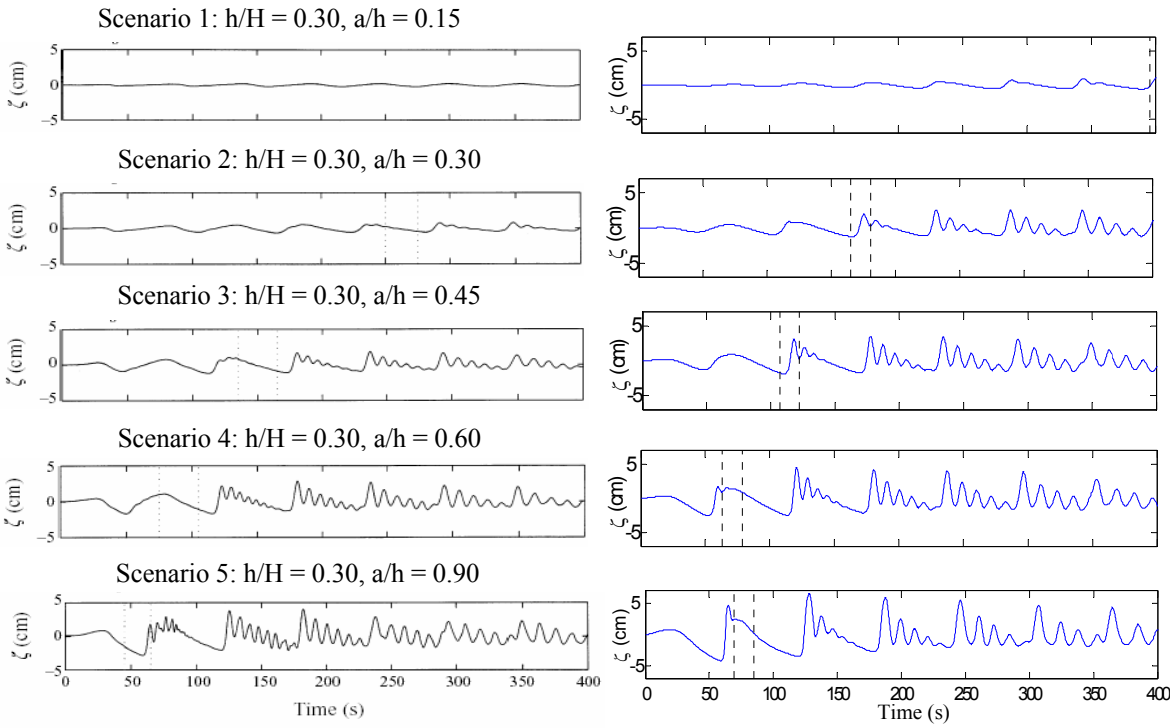

Figure 3.12: Interfacial displacements for Group A at the center of the tank. The figures on the left are Horn's experiment (Horn, et al., 2001). The figures on the right are the model simulations. In both sets of figures, the dotted lines indicate the range in which solitons emerged.

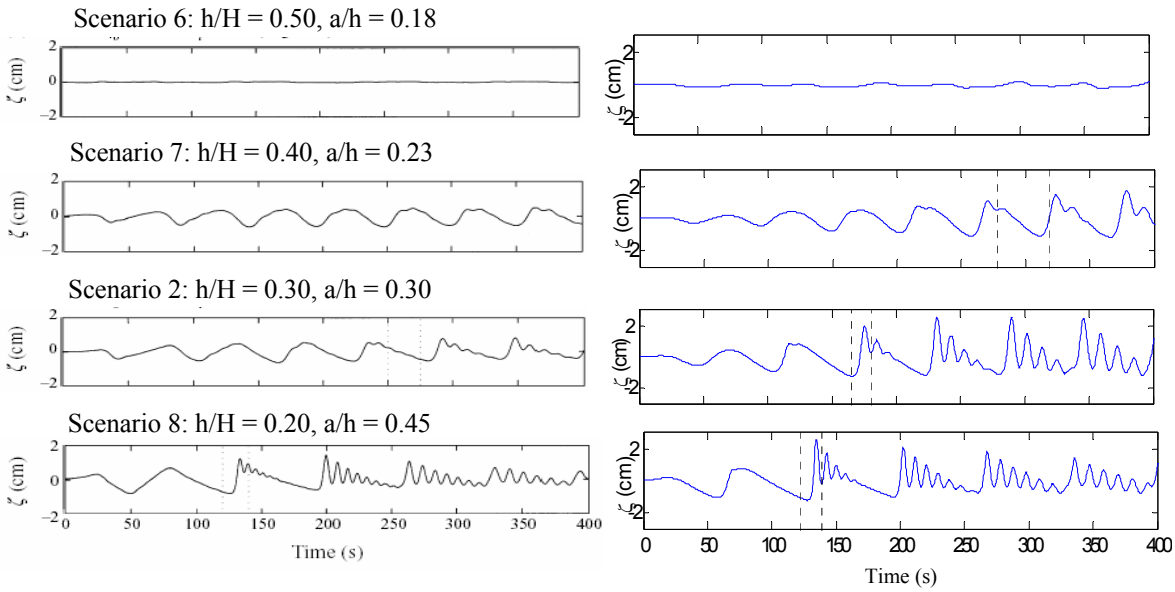

Figure 3.13: Interfacial displacements for Group B at the center of the tank. The figures on the left are Horn's experiment (Horn, et al., 2001). The figures on the right are the model simulations. In both sets of figures, the dotted lines indicate the range in which solitons emerged.

where h_1 is the upper layer thickness, h_2 is the lower layer thickness, H is the total depth, c is the wave speed:

$$c = \sqrt{g' \frac{h_1 h_2}{H}} \qquad (3.12)$$

g' is reduced gravity. The timescale of steepening was calculated for each scenario and are reported in Table 3.3. The model simulations have soliton formation slightly earlier than the timescale of steepening and Horn's observations (Figures 3.14). This discrepancy can be attributed to the inviscid approximation in the model.

Table 3.3: Timescale of steepening for scenarios in internal wave test case (§3.3).

Scenario	Ts (s)
1	427
2	213
3	142
4	107
5	71
6	--
7	446
8	124
9	--

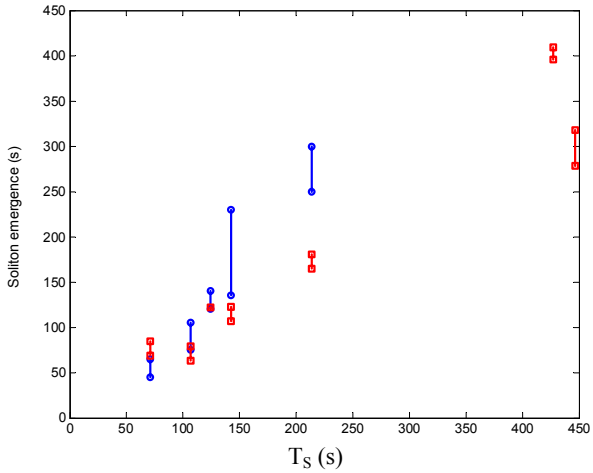

Figure 3.14: Comparison of timescale of steepening with Horn's observation of the emergence of solitons (blue lines with circle) and model simulation observation of the emergence of solitons (red lines with square).

Number of Solitons

Scenarios 3-5 had less solitons emerge in the model simulation than in Horn's laboratory experiment. The reason for this is unknown. The number of solitons is not a function of viscosity, like the difference in wave amplitude and time of soliton emergence. The number of solitons appears to be dependent on the horizontal grid resolution (§4.1 ff.). The grid resolution examined in this section (60×73) represents the initial wavelength (12 m) by 120 grid cells. The author's hypothesis that this resolution would be sufficient is incorrect. There needs to be more investigation into the lower limit of resolution needed to capture all of the solitons in the wave series. However, the grid resolution must be balanced with viscosity since horizontal grid refinement decreases the numerical viscosity to the same order of magnitude or smaller than molecular viscosity (§4.1 ff). With decreased numerical

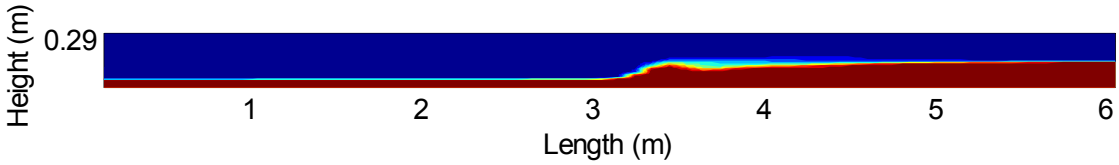

Figure 3.15: Scenario 5, bore development at time 60s.

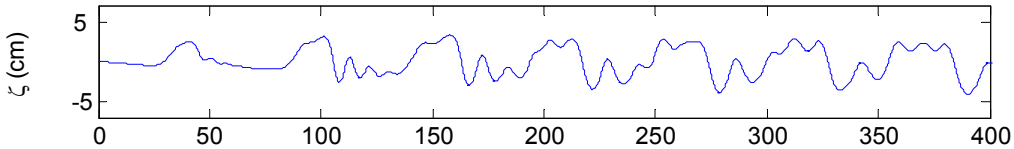

Figure 3.16: Isopycnal displacement for scenario 9 at the center of the tank. h/H = 0.5 and a/h = 1.0.

viscosity, the modeled wave amplitude and time of emergence of solitons may become significantly different than what is predicted by theory and shown in laboratory experiments.

3.4 Summary

The manufactured solution (§3.1) verified that the non-hydrostatic solver is accurate and convergent. The convergence criterion was established to be when the L_∞ residual norm is decreased by four orders of magnitude. The internal wave test basin (§3.2) validated the convergence criterion established by the manufactured solution and determined the number of non-hydrostatic pressure solver iterations per timestep needed for convergence. Comparison between Horn's experiments and model results validates the non-hydrostatic solver by showing it captures the physics of internal wave evolution.

Non-hydrostatic pressure has a dispersive effect on internal wave evolution. The non-hydrostatic model clearly demonstrates the emergence of solitons for a wave that lies within regime 2. The major difference between Horn's laboratory experiment and the model simulations is the viscous effects in Horn's experiment are not included in the model simulations. Horn's experiment has a large boundary layer area compared to volume of the basin, thus viscous effects are prevalent in the laboratory results. The model simulations did not model viscosity, so solitons emerged earlier and soliton amplitudes were larger. However, the basic characteristics of the wave train were captured by the model. The model was not able to correctly represent the number of solitons in the wave series at the grid resolution used. In summary, the non-hydrostatic model is shown to be valid when tested against theory and a laboratory experiment. The non-hydrostatic model captures the physics of internal wave evolution.

Chapter 4. Comparison of Hydrostatic and Nonhydrostatic models

Hydrostatic models do not model the physics of wave dispersion (a non-hydrostatic process), yet Hodges and Delavan (2004) observed significant wave dispersion in a hydrostatic model which produces soliton-like formations. Such soliton-like formations may mimic the expected internal wave evolution, however this coincidence is a false positive. Without non-hydrostatic pressure, the soliton-like formations can only be an artifact of the numerical method, and is thus dependent on grid resolution and numerical truncation error. Previous literature has not examined the effect of grid resolution on hydrostatic and non-hydrostatic model performance. This chapter examines laboratory and lake scale simulations. The laboratory-scale simulations examine nine different internal waves (§3.3) and qualitatively compares the laboratory experiments to the hydrostatic and non-hydrostatic model simulations. One laboratory-scale internal wave case is examined on different grid meshes to examine the effect of grid resolution on model skill for the hydrostatic and non-hydrostatic models. The lake-scale simulation is also analyzed on different grid meshes. The analytical techniques in §2.2 are used to quantitatively evaluate changes in energy, which is used to compare differences between hydrostatic and non-hydrostatic models on the different grid meshes.

4.1 Laboratory Scale Comparison

Results of hydrostatic and non-hydrostatic models have been compared with the same laboratory experiments (Horn, et al., 2001) used in §3.3. Non-hydrostatic pressure is a small-scale effect; thus, it is advantageous to model a laboratory-scale internal wave because the small-scale grid (e.g. 0.1 m × 0.004 m) allows the non-hydrostatic pressure to affect wave evolution and not be damped out due to the size of the grid. The hydrostatic and non-hydrostatic models used eight different grid resolutions to compare model skill for one scenario (scenario 2, Table 3.2). The grid aspect ratios ($\Delta z/\Delta x$) for all resolutions were of $O(10^{-2})$ or greater.

4.1.1 Setup

Basin dimensions and the scenarios are identical to those listed in §3.3.1 and Table 3.2. Each scenario was separately simulated using the both hydrostatic and non-hydrostatic models (§4.1.2). For all scenarios, a model grid of 60×73 (Δx = 0.1 m and Δz = 0.004 m) was used. The pycnocline is represented by five cells ($h_{py}/\Delta z = 5$). Scenario 2 is modeled on several different grid meshes, as described in Table 4.1, to compare model error (§4.1.3). Each simulation for the changing grid resolution was run for ten wave periods as this time allows the internal wave to evolve and develop into solitons. All simulations used the inviscid/diffusionless approximation.

Table 4.1: Grid meshes for scenario 2 simulations. Those meshes with an 'x' were performed.

	# Cells in Z-dir			
# Cells in X-dir	15	29	73	$\lambda_o/\Delta x$
30	x	x	x	60
60	x	x	x	120
600	x	x		1200
$h_{py}/\Delta z$	1	2	5	

The timestep is dependent on the physics of the wave and the grid resolution. Due to the characteristics of the hydrostatic and non-hydrostatic models, the timestep required to yield a stable solution is different. For both models, the timestep selection is based on the Courant-Friedrich-Lewy (CFL) condition for baroclinic motions. The hydrostatic model uses the form of the CFL condition:

$$CFL_x \equiv c\frac{\Delta t}{\Delta x} \tag{1.13}$$

where Δt is the timestep for a specific, initial internal wave speed (c) and grid resolution (Δx). The CFL condition is a non-dimensional number which limits the timestep and grid discretization needed to stabilize the conditionally stable explicit Euler scheme (Ferziger and Perić, 2002) used in CWR-ELCOM. The baroclinic CFL condition is the most restrictive condition, as opposed to the barotropic or advective CFL condition, for density-stratified flows (Hodges, 2000). In CWR-ELCOM, the maximum allowed baroclinic $CFL_x = \sqrt{2}$ (Hodges, 2000), but this work uses a conservative CFL_x condition of 1/3. The hydrostatic model is dissipative (§4.1.3 ff.), so strong vertical motions are inhibited. The CFL_x condition in Equation (1.13) provides a sufficient timestep for the hydrostatic model. However, the non-hydrostatic model is generally less dissipative, especially for finer horizontal grid resolutions (§4.1.3 ff.), so strong vertical motions may occur.

Thus, the timestep that was appropriate for the hydrostatic model is not suitable for the non-hydrostatic model (i.e. strong vertical motions cause instabilities, Figure 4.1) and the timestep must be smaller. The timestep for the non-hydrostatic model is determined by the vertical velocity and vertical grid resolution, yielding a new definition for the CFL condition:

$$CFL_z \equiv \frac{ac}{\Delta x}\frac{\Delta t}{\Delta z} \tag{1.14}$$

where a is the wave amplitude and $ac/\Delta x$ is a measure of vertical velocity of a bore. The maximum CFL_z condition allowed is 1/3. The smaller timestep simulation does show a marked improvement in the internal wave evolution in the non-hydrostatic model (Figure 4.1), and is thus used for further analysis. The hydrostatic model is not significantly altered by the different timesteps.

4.1.2 Scenario Simulations

This section uses qualitative comparisons between the laboratory experiment and the hydrostatic and non-hydrostatic model simulations. The number of solitons that emerge in a wave train for the laboratory experiment and the model simulations is compared to the theoretical number of solitons that will evolve. Kao, et al. (1985) defined the theoretical number of solitons (N) that will evolve in a train as:

$$N \le \frac{M}{\pi} + 1 \tag{1.15}$$

where M is defined for a two-layer system in a model with the Boussinesq approximation:

$$M = \left[\frac{3}{2}\frac{h_1 - h_2}{h_1^2 h_2^2}\eta_o\right]^{\frac{1}{2}} L \tag{1.16}$$

The length of the basin is L, h_1 is the upper layer thickness, h_2 is the lower layer thickness and η_o is the wave amplitude. The results are separated into the simulations for group A, group B, scenario 9 and the number of solitons that emerge in a wave train.

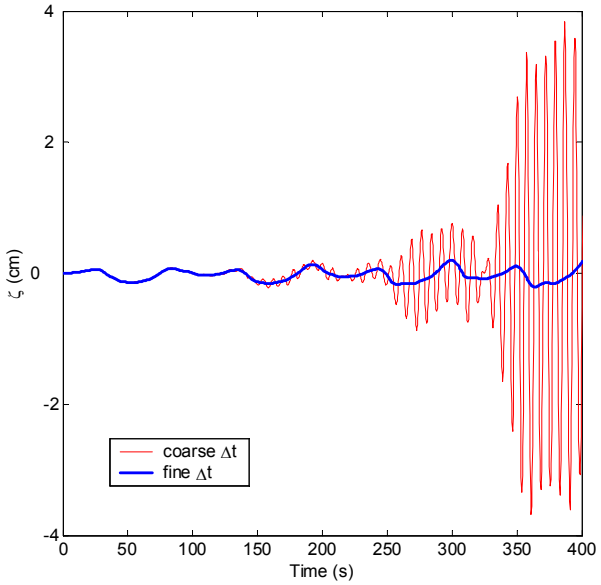

Figure 4.1: Scenario 6 pycnocline displacement simulated with a coarse timestep, determined by CFL_x, and a fine timestep, determined by CFL_z.

Group A

Group A has the same interface depth ratio (h/H = 0.3) and varies the amplitude of the wave for each scenario (Figure 4.2). At small amplitudes (scenario 1), there is some small steepening but no solitons emerge; both models show similar evolution. For scenarios with larger amplitudes (regime 2), the nonlinearity of the wave increases causing the wave to steepen and evolve into a train of solitons with decreasing amplitude. The non-hydrostatic model represents this evolution, while the hydrostatic model showed bore formation. Scenario 5 has the greatest initial amplitude and forms an undular bore. The laboratory experiment shows a high-frequency signal, indicating that the bore was initially turbulent (Horn, et al., 2001). The non-hydrostatic model shows the bore formation, but does not show a high-frequency signal or any other indication of turbulence in the wave evolution. The non-hydrostatic model was able to characterize the soliton train that formed in the laboratory experiment after the bore was damped by turbulent mixing. The hydrostatic model developed the initial bore with a slightly smaller amplitude than the non-hydrostatic model. As time progresses, the hydrostatic model retains the bore shape in the leading wave and develops soliton-like features behind it.

Group B

Group B varies the interface depth ratio for each scenario (Figure 4.3). For scenarios with larger depth ratios, that is a thick upper layer, the nonlinearity of the wave is small. When the depth ratio is at mid-depth (h/H = 0.5, scenario 6), the

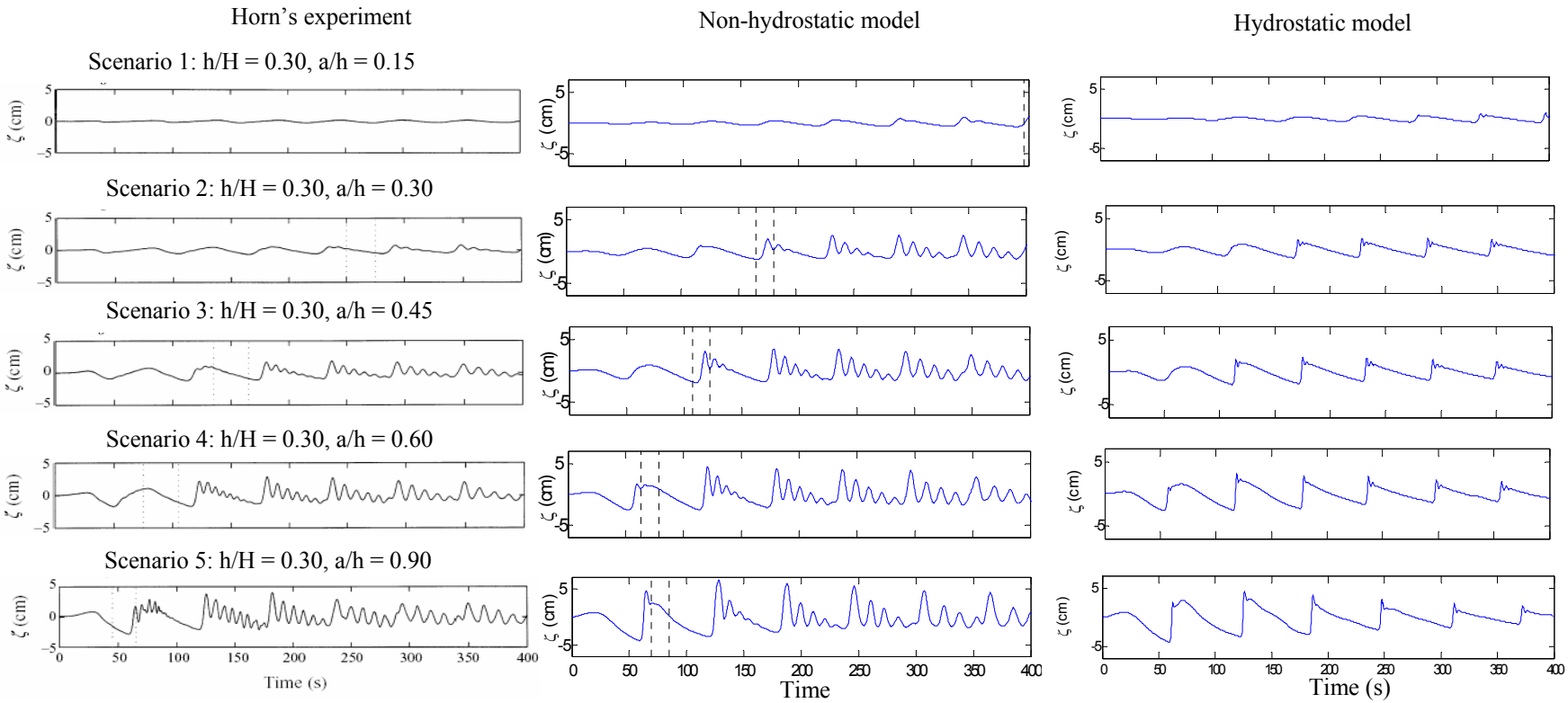

Figure 4.2: Interfacial displacements for Group A measured at the center of the tank. The figures on the left are Horn's experiment (Horn, et al., 2001). The figures in the middle are the non-hydrostatic model simulations. The figures on the right are the hydrostatic model simulations. The dotted lines in Horn's experiment and the non-hydrostatic model indicate the range of time in which solitons emerged.

system has no appreciable nonlinearity and the hydrostatic and non-hydrostatic model produce similar results. A thin upper layer (i.e scenario 8) causes the wave to steepen quickly and results in a train of solitary waves with larger amplitudes (a ~ 2.5 cm) than a thicker upper layer (i.e. scenario 7, a ~ 1.7 cm), which is seen in the non-hydrostatic model. The hydrostatic model is able to predict the onset of steepening, but the wave evolution is entirely unphysical.

Scenario 9

Horn, et al. (2001) observed shear instabilities developing into Kelvin-Helmholtz billows in only one experiment (scenario 9). There is no figure of laboratory observations of this experiment, and it is not specified how the wave evolves after the billowing event, so no direct comparison can be made between the laboratory experiments and model simulations. Neither the hydrostatic, nor the non-hydrostatic models were able to capture Kelvin-Helmholtz billows. Horn, et al. (2001) observed two bores form at both ends of the tank and propagate towards the center, which the non-hydrostatic model did simulate. The non-hydrostatic model shows the bore propagation, with a series of solitons behind the bore (Figure 4.4). The hydrostatic model has neither bore formation, nor Kelvin-Helmholtz billows.

Number of Solitons in Wave Train

In general, the non-hydrostatic model underestimates the number of observed solitons in the wave series from the laboratory experiment (§3.3.3). The theoretical number of solitons, as defined by Kao, et al. (1985), for each scenario is in Table 4.2. Figure 4.5 shows how the number of solitons in a train for the model simulations and laboratory experiments compare with the theoretical number of solitons. The theoretical number of solitons is always larger than what was observed in the laboratory experiment and the model simulations.

Summary

The non-hydrostatic model reproduces the results of the laboratory experiment quite well for the different scenarios (Figures 4.2 and 4.3). The non-hydrostatic model shows solitons emerge sooner than in the laboratory experiments and slightly greater amplitude in isopycnal displacement. This can be attributed to the application of the inviscid approximation as discussed in §3.3.3. The hydrostatic model captures the evolution for weakly nonlinear waves (scenarios 1 and 6), but presents a poor representation of nonlinear wave evolution (scenarios 2-5, 7 and 8; Figures 4.2 and 4.3). In scenarios 2-5, 7 and 8, the hydrostatic model exactly matches the non-hydrostatic model until steepening causes the hydrostatic model to develop into a bore while the non-hydrostatic model evolves into a train of solitons. Bore development in the hydrostatic model is typically followed by some soliton-like formations, but these are different from observations in the laboratory experiments and non-hydrostatic model simulations. The hydrostatic soliton-like formations are near the crest of the bore front and their amplitudes are small compared to the amplitudes of the soliton trains in the laboratory experiments. A comparison of internal wave evolution for scenario 2 is seen in Figure 4.6. This confirms observations of hydrostatic and non-hydrostatic internal wave evolution from the isopycnal displacement.

Discussion

Observations of the isopycnal displacement demonstrate that the non-hydrostatic model performs better than hydrostatic model, with respect to reproducing the internal wave evolution of the laboratory experiments by Horn, et al. (2001). The non-hydrostatic model shows clear differences in internal wave evolution among the different scenarios, while the hydrostatic model either shows a damped wave (scenario 1 and 6) or a bore with small soliton-like formations (scenario 2-6, 7 and 8). The soliton-like formations behind the bore do not disperse or change in amplitude as time progresses; this observation is the same for all scenarios where bore formation occurs. The non-hydrostatic model shows the train of solitons disperses behind the leading wave and decrease in amplitude with time, as in the laboratory experiment. Non-hydrostatic pressure is a dispersive property (Long, 1972); the non-hydrostatic model's ability to simulate dispersion verifies that the non-hydrostatic model captures the overarching physics of nonlinear wave evolution.

Table 4.2: Theoretical number of solitons (N) that will develop for a 2-layer, Boussinesq model.

Simulations	1	2	3	4	5	6	7	8	9
N	6.2	8.3	9.9	11.3	13.6	1.0	5.6	12.7	1.0

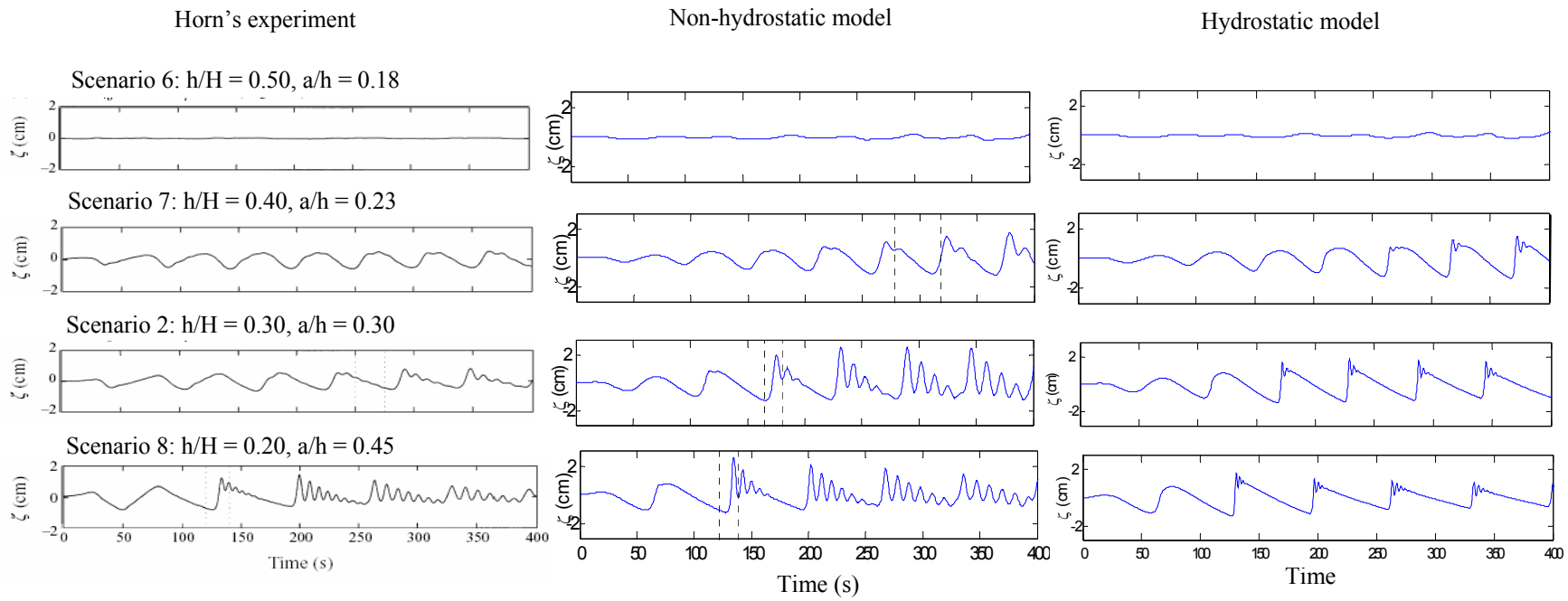

Figure 4.3: Interfacial displacements for Group B measured at the center of the tank. The figures on the left are Horn's experiment (Horn, et al., 2001). The figures in the middle are the non-hydrostatic model simulations. The figures on the right are the hydrostatic model simulations. The dotted lines in Horn's experiment and the non-hydrostatic model indicate the range of time in which solitons emerged.

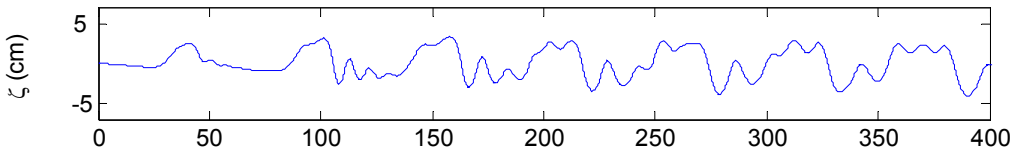

Figure 4.4: Isopycnal displacement for scenario 9 at the center of the tank. h/H = 0.5 and a/h = 1.0.

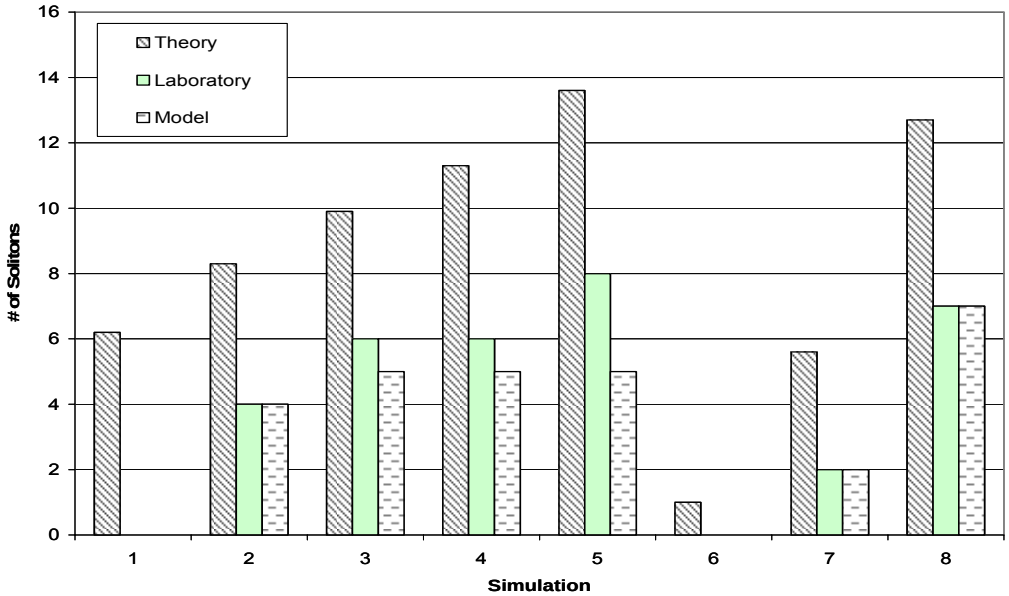

Figure 4.5: Number of solitons that develop according to theory (Kao, et al., 1985) and in the laboratory experiment and model simulations.

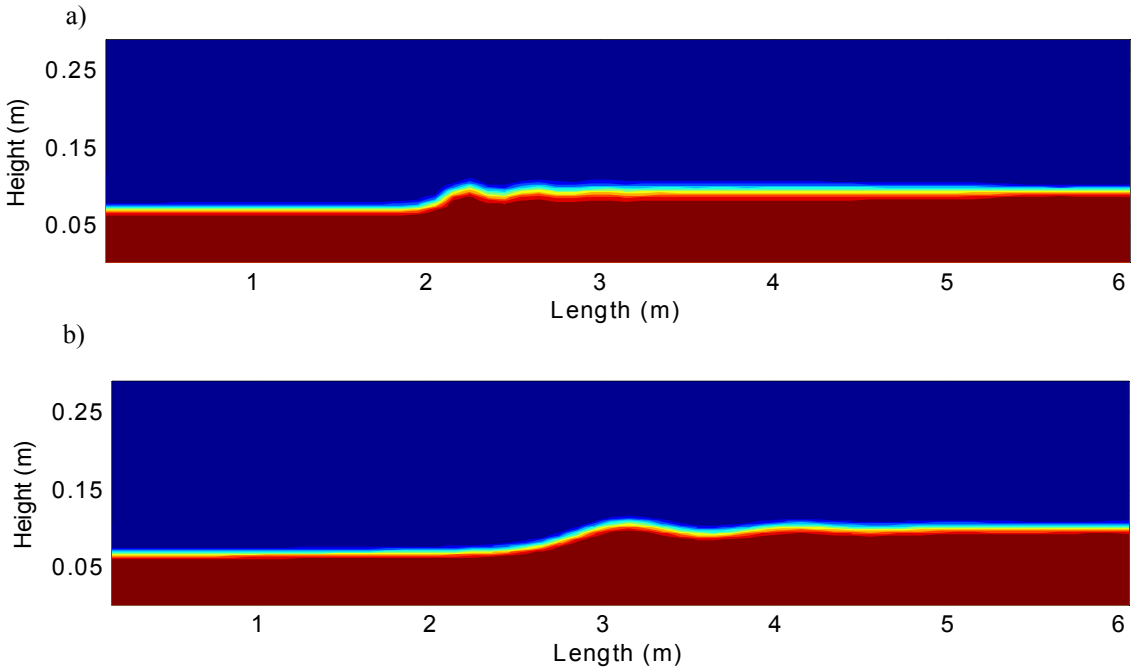

Figure 4.6: a) Hydrostatic and b) non-hydrostatic model of scenario 2 internal wave evolution.

Wave evolution in scenario 9 includes the appearance of shear instabilities in a Kelvin-Helmholtz billow (Horn, et al, 2001). While neither the hydrostatic nor the non-hydrostatic models were able to capture the billows. However, the non-hydrostatic model was able to simulate the bore formation propagating from the end of the tank. Horn, et al. (2001) does not specify how the wave evolves after the Kelvin-Helmholtz billow collapses, but it is speculated that the wave will degenerate into a train of solitons. The non-hydrostatic model shows a series of solitons develop behind the leading bore. If the speculation of the wave evolution is correct, than the non-hydrostatic model may be a reasonable estimation of the wave evolution after the initial Kelvin-Helmholtz billow formation and collapse.

4.1.3 Changing the Grid Resolution

Scenario 2 was examined on several different grids (Table 4.1) to asses the effect of grid resolution on the models' performance. Scenario 2 lies within regime 2 and is expected to have steepening and soliton formation. The analysis techniques discussed in §2.2 are used to quantify differences between the models and grid resolutions. Specifically, the different analysis methods used to quantify model results are the isopycnal displacement, background potential energy evolution, numerical diffusivity, dynamic energy evolution, numerical viscosity and the power spectral density.

Isopycnal Displacement

The isopycnal displacement of scenario 2 for the different grid resolutions is seen in Figures 4.7 and 4.8. The wave evolution for a grid refined vertically (Figure 4.7) shows that the leading wave moves slightly faster for finer vertical grids. The amplitudes of all the solitons within the wave train are smaller for finer vertical grids (~ 1 cm difference between the coarsest and finest grids in Figure 4.7). This is seen in both the hydrostatic and non-hydrostatic models. Horizontal refinement substantially changes the pycnocline displacement (Figure 4.8). Horizontal grid refinement also develops differences in the wave period. As the grid is horizontally refined, the hydrostatic and non-hydrostatic models predict a smaller wave period; that is in Figure 4.8, the finer horizontal grid has an average wave period of 120 s, while the coarser grid has an average wave period of 230 s. Furthermore, the effect of grid scale on the wave influences the formation of soliton trains. The non-hydrostatic model has more solitons in the wave train for the finer grid than the coarser grid. Finally, the leading soliton has approximately the same wavelength (~1 m) through time and for the different grids in the non-hydrostatic model. In the hydrostatic model, the wave evolves into a bore followed by soliton-like formations; the wavelengths of the soliton-like formations change in size as the grid is refined.

Background Potential Energy

Changes in the background potential energy (E_B) represent numerical diffusion in a diffusionless model (§2.2). The non-hydrostatic and hydrostatic models show an increase in the background potential

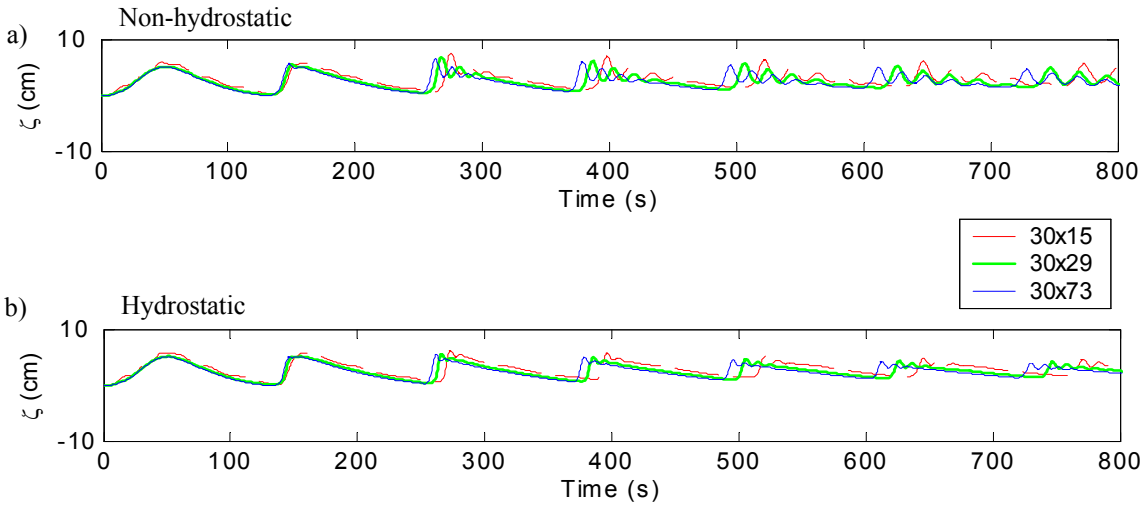

Figure 4.7: Isopycnal displacement of scenario 2 for vertical grid refinement, measured at the center of basin. a) Non-hydrostatic model, b) hydrostatic model.

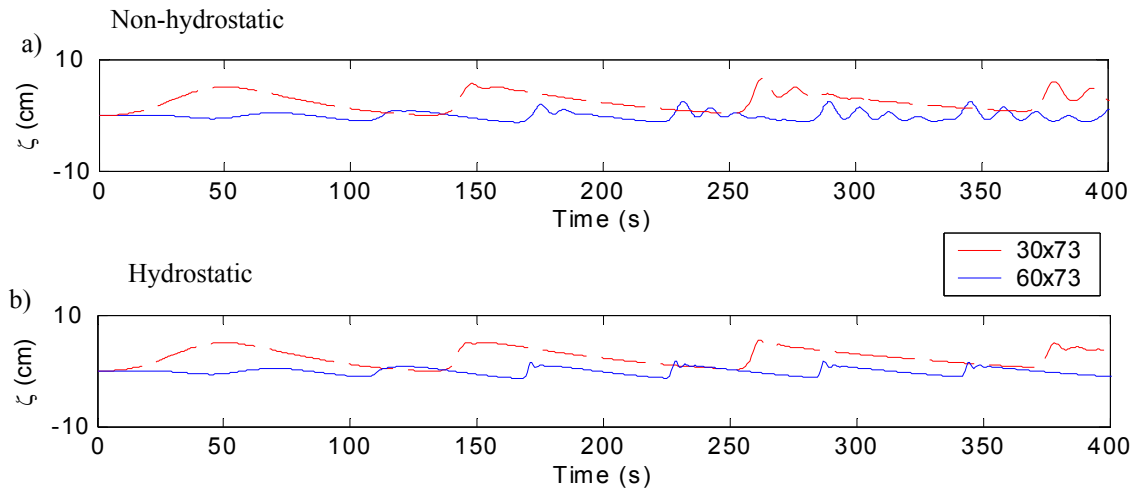

Figure 4.8: Isopycnal displacement of scenario 2 for horizontal grid refinement, measured at the center of basin. a) Non-hydrostatic model, b) hydrostatic model.

energy (E_B), with the hydrostatic model increasing at a slightly lower rate (Figure 4.9). In both models, grid refinement in the horizontal direction (Figure 4.9 c and d) shows more change in E_B over time. In the non-hydrostatic model, the finest horizontal grid (600×29) has a change in E_B of about 92% over nine wave periods, while the coarsest grid (30×29) has a change in E_B by 80% (Table 4.3). The hydrostatic model has a change in E_B by 89% for the finest grid and 77% for the coarsest grid (Table 4.3). In the hydrostatic and non-hydrostatic models, refinement in the vertical direction shows less change in E_B (Figure 4.9 a and b). The finest vertical grid (30×73 and 60×73) is about an order of magnitude less than the coarsest vertical grid (30×15 and 60×15).

The system can be considered unphysical when the normalized background potential energy (Figure 4.9) goes above unity. In the non-hydrostatic model, the E_B goes above unity around three wave periods for the coarsest grid (30×15). Refining the grid horizontally for this vertical resolution decreases the time when the E_B goes unphysical to 2.2 wave periods. For the 600×29 grid, the E_B increases above one around five wave periods, while the 30×29 grid is physical until about nine wave periods. The hydrostatic model has slightly less diffusion than the non-hydrostatic model and remains physical for only a short time longer. Conversely, vertical refinement significantly improves the numerical diffusion in both models (Figure 4.9); at ten wave periods the E_B is well below unity for the finest vertical resolution, irrespective of the horizontal resolution. A coarse vertical grid has more effective numerical diffusion than a fine vertical grid, so grid refinement reduces the numerical diffusion.

Table 4.3: Percent increase in background potential energy for scenario 2.

Grid	% Increase	
	Hydrostatic	Non-hydrostatic
30*15	90	91
60*15	79	90
600*15	77	80
30*29	89	92
60*29	78	85
600*29	77	80

Numerical Diffusivity

The numerical diffusion coefficient (Figure 4.10) derived in §2.2 confirms what was observed in the background potential energy (E_B); vertical refinement reduces the system's diffusivity, while refinement in the horizontal increases the system's diffusivity (Figure 4.10). The hydrostatic model has lower diffusivities than the non-hydrostatic model for all grids, except 60×73. As time progresses, there is an initial growth in the diffusivity, followed by a continual decline. This trend matches the behavior of E_B, which increases rapidly at first and flattens with time (Figure 4.9). The numerical diffusivity is orders of magnitude larger than the diffusivity of salt, indicating that numerical diffusion is significant in the models and physical diffusion (in

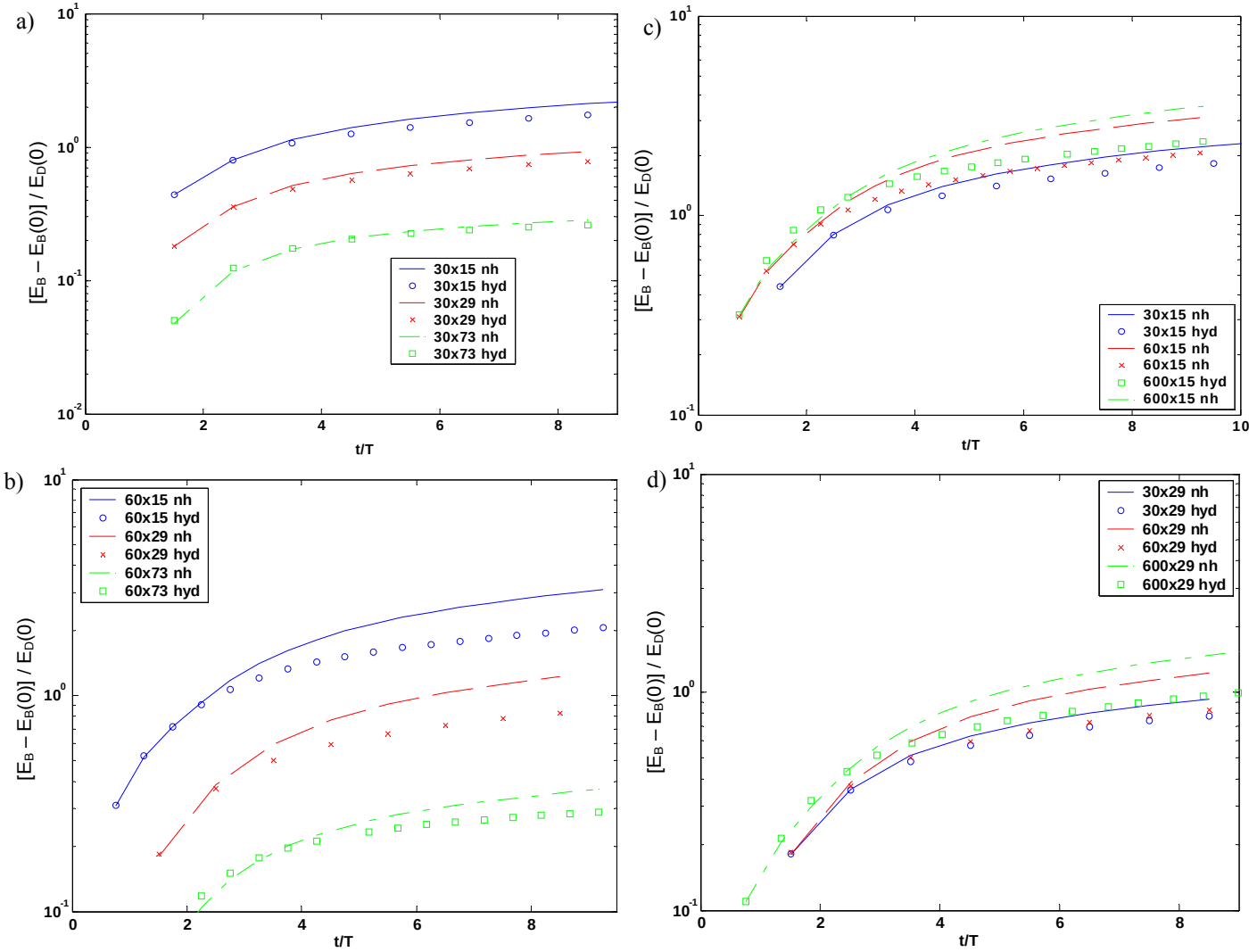

Figure 4.9: Background potential energy (E_B) of scenario 2 for different grid resolutions. A) Horizontal grid = 30, B) Horizontal grid = 60, C) Vertical grid = 15, D) Vertical grid = 29. Lines represent non-hydrostatic model results (nh), markers represent hydrostatic model results (h). The difference between E_B and the initial E_B is normalized by the initial dynamic energy (E_D).

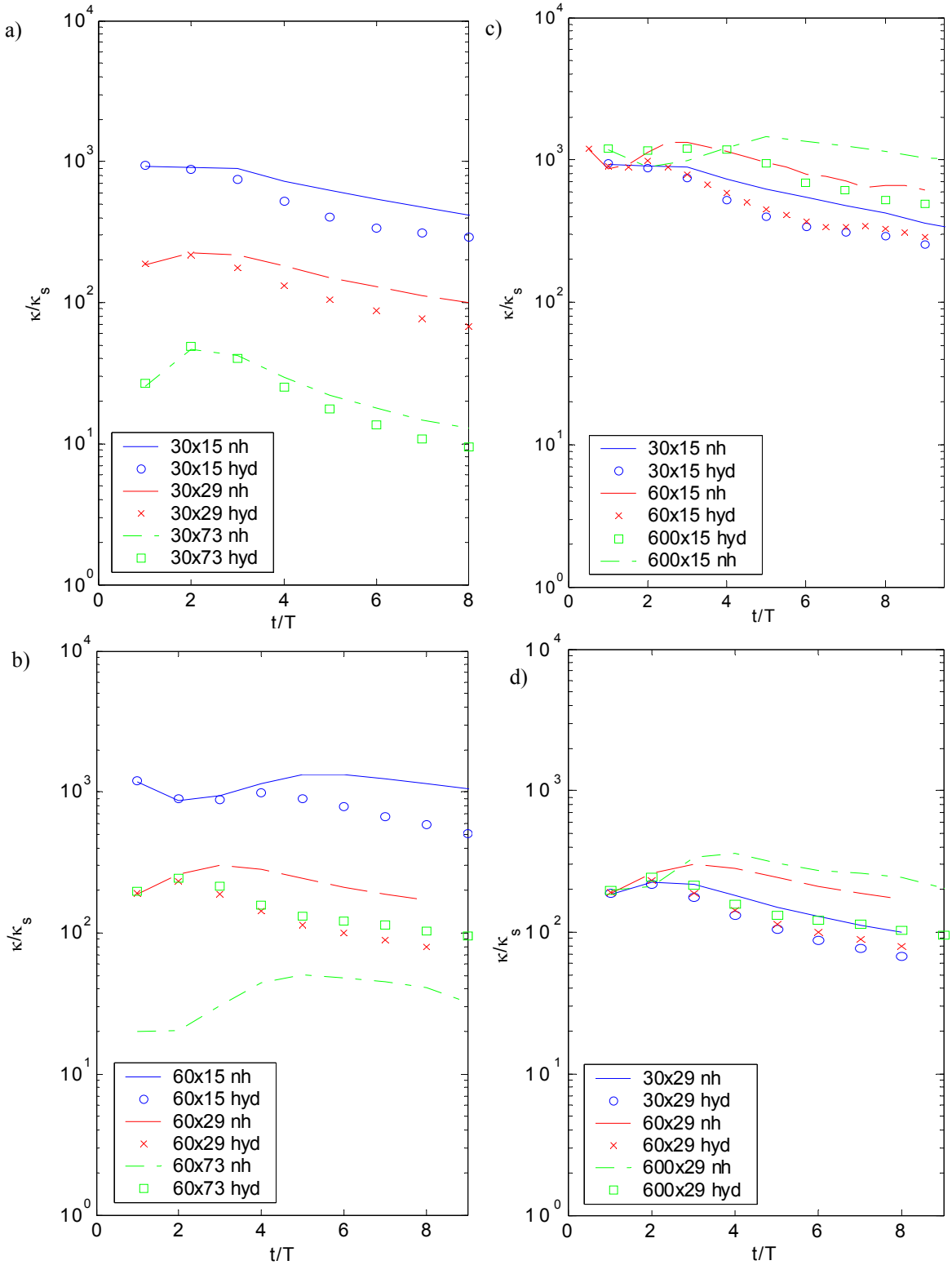

Figure 4.10: Numerical diffusivity (κ) of scenario 2 for different grid resolutions. a) Horizontal grid = 30, b) horizontal grid = 60, c) vertical grid = 15, d) vertical grid = 29. Lines represent non-hydrostatic model results (nh), markers represent hydrostatic model results (h). $\kappa_s = 10^{-9}$ m^2/s.

the absence of turbulence and wave breaking) would have a negligible effect on internal wave evolution.

Dynamic Energy

Decreases in dynamic energy (E_D) represent the dissipation by numerical error (§2.2). The non-hydrostatic model has lower dissipation rates than the hydrostatic model for all grid resolutions (Figure 4.11). Horizontal grid refinement (Figure 4.11 c and d) decreases the rate at which E_D is dissipated. For the finest horizontal grid resolution (600×29), the non-hydrostatic model dissipates E_D by 8% over nine wave periods, whereas the hydrostatic model dissipates E_D by 85%. The coarsest grid (30×29) dissipates E_D by 80% in the non-hydrostatic model and the hydrostatic model dissipates E_D by 90% (Table 4.4). Vertical grid refinement (Figure 4.11 a and b) generally increases the dissipation rate. However, the 600×29 grid has less dissipation than the coarser 600×15 grid, which is counter to other observations of vertical grid refinement (Figure 4.12).

Numerical Viscosity

Numerical viscosity (§2.2) tends to be smaller for finer resolution grids (Figure 4.13); the non-hydrostatic model produces numerical viscosities that are smaller than those produced by the hydrostatic model. Generally, the numerical viscosity increases and then decreases as time progresses. The decrease in numerical viscosity with time corresponds to an overall decrease in dynamic energy (Figure 4.11). Once the dynamic energy begins to decrease, the velocity shears that drive the numerical viscosity are being reduced. That is, any system with a lower dynamic energy should generally lose dynamic energy at a lower rate than a system with a higher dynamic energy, and thus a lower numerical viscosity is expected, which is seen in Figures 4.11 a and b and 4.13 a and b. The numerical viscosity is slightly larger than molecular viscosity; as the grid is refined, the numerical viscosity decreases and nears the molecular viscosity. Numerical viscosities computed for the hydrostatic model are slightly greater than those for the non-hydrostatic model, which is expected as the hydrostatic model has greater numerical dissipation than the non-hydrostatic model.

Power Spectral Density

The power spectral density (§2.2) quantifies the energy transfer of different wavelength waves over time (Figure 4.14). The peak power in a wave

Table 4.4: Percent decrease in dynamic energy for scenario 2.

Grid	% Increase	
	Hydrostatic	Non-hydrostatic
30*15	85	77
60*15	85	47
600*15	80	20
30*29	91	80
60*29	90	52
600*29	89	8

evolution is associated with the wavelength that has the maximum pycnocline displacement (i.e. amplitude). For all grid resolutions, the hydrostatic model had no shift in peak power from the initial wavelength within ten wave periods (Figure 4.15). However, there is still some energy transferred to different wavelength waves. Timeslices of the power spectral density show as the wavelength decreases there is energy associated with certain wavelengths that follow a harmonic pattern (Figure 4.16). The non-hydrostatic model does show a shift in peak power between four and seven wave periods depending on the grid resolution (Figure 4.15). Finer horizontal grids shift the peak power sooner than coarser horizontal grids. The peak power shifts to different wavelengths, although the range is small (~ 0.12 – 0.17 wavelengths). Once the peak power shift has taken place, all grid resolutions for the non-hydrostatic model show similar peak power/wavelength evolution. For example, as seen in Figure 4.15d, the 600×29 grid shifts the peak power at $t/T = 4$ to $\lambda/\lambda_o = 0.12$. At $t/T = 4.5$, the 600×29 mesh shifts to $\lambda/\lambda_o = 0.15$, which coincides with the peak power shift of the 60×29 grid. Prior to the peak power shift, the non-hydrostatic model shows a harmonic energy shift to $\lambda/\lambda_o = 0.5$ and some smaller wavelengths (Figure 4.17). However, after the peak power shift, the peak power is located at a wavelength ratio (λ/λ_o) of 0.2 for all grid resolutions. The spectral analysis shows that the peak power shift is to 20% of the initial basin-scale wavelength, which is consistent with the degeneration of the wave into a train of five solitons (Figure 4.2). The increase in power at small wavelengths shows that energy is being directly transferred from the basin-scale wave to the train of solitons.

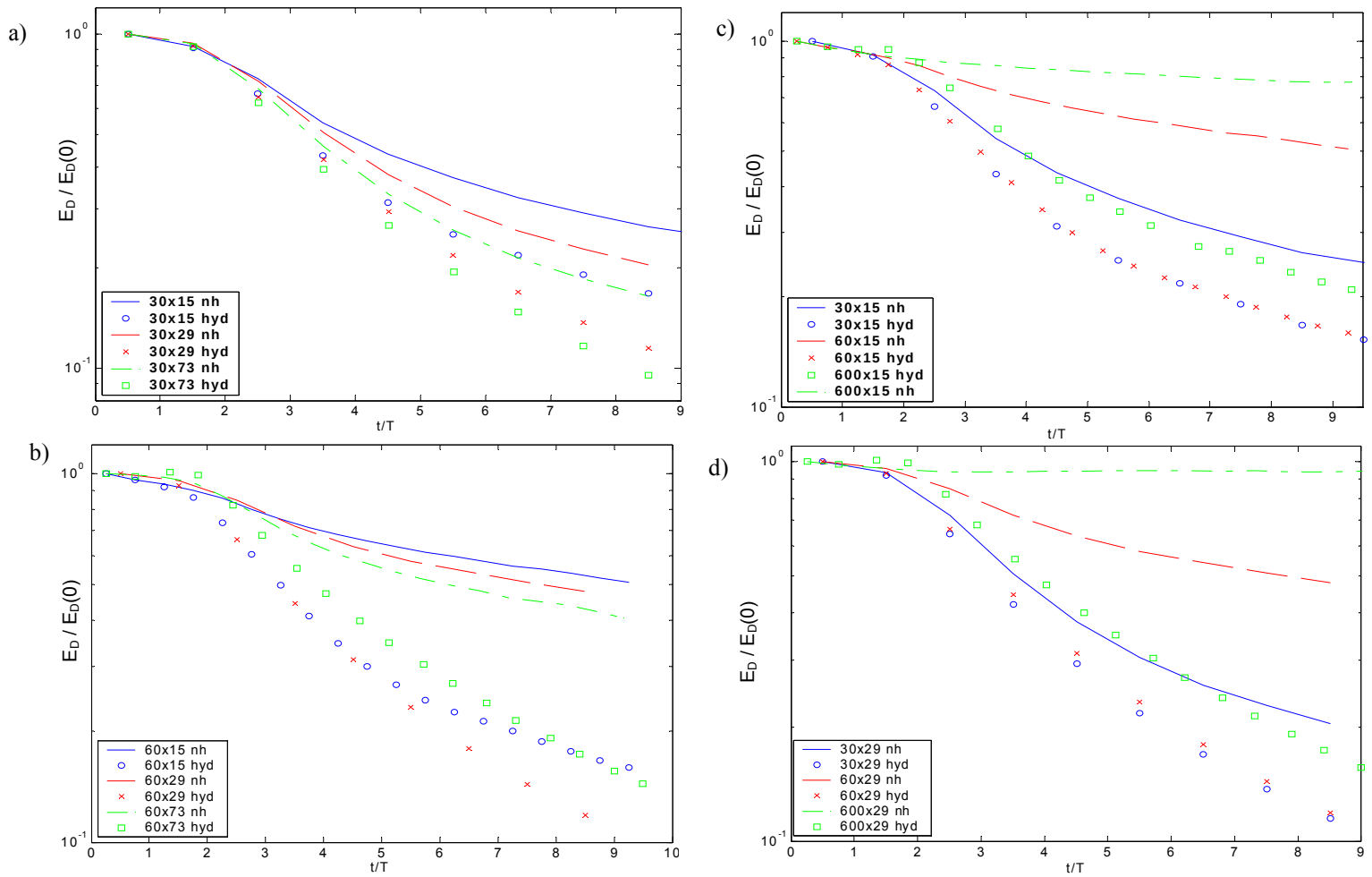

Figure 4.11: Dynamic energy (E_D) of scenario 2 for different grid resolutions, a) Horizontal grid = 30, b) Horizontal grid = 60, c) Vertical grid = 15, d) Vertical grid = 29. Lines represent non-hydrostatic model results (nh), markers represent hydrostatic model results (h). E_D is normalized by the initial E_D.

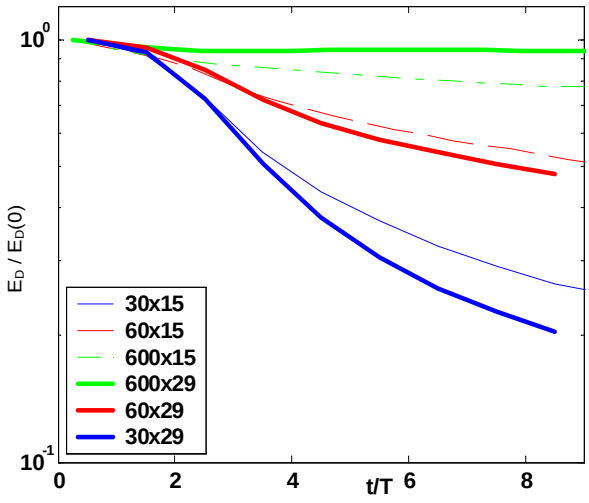

Figure 4.12: Dynamic energy of scenario 2 for the non-hydrostatic model. Six grids are displayed where the horizontal refinement (horizontal grid = 30, 60 and 600) is the same for two different vertical grids (vertical grid = 15 and 29). E_D is normalized by the initial E_D.

Discussion

The key findings of the laboratory-scale model simulation are: 1) in both the hydrostatic and non-hydrostatic models horizontal grid refinement always leads to more growth in the background potential energy and larger numerical diffusivities, indicating the horizontal grid refinement increases the numerical diffusion of the system, 2) the hydrostatic model is more dissipative and somewhat less diffusive than the non-hydrostatic model and 3) the non-hydrostatic model is nearly free of numerical dissipation for a sufficiently refined horizontal grid and the controlling mechanism for model skill is numerical diffusion. The increase in background potential energy with horizontal grid refinement is opposite of the conventional wisdom that reducing grid size must improve model skill and reduce error. This finding corroborates the finding of Hodges and Delavan (2004) and may be explained by examining the concept of energy exchange from §2.2. Dissipation decreases the dynamic energy, which is the kinetic and available potential energy. The available potential energy is the energy that activates diffusion (when mixing occurs). Thus, if there is less available potential energy to be mixed, then there is less possible diffusion. As the grid is horizontally refined, the dissipation rate decreases. Reducing numerical dissipation allows the background potential energy to continue to grow, thereby increasing numerical diffusion. The non-hydrostatic model has less dissipation than the hydrostatic model (Figure 4.11), and thus has more diffusion (Figure 4.9). Vertical grid refinement generally has less numerical diffusion and more numerical dissipation in both models, which is tied to the above idea that the more dynamic energy is damped, the less energy available to be diffused.

The results indicate that for the non-hydrostatic model numerical diffusion is strongly dependent on the vertical grid resolution (Figure 4.9 a and b and Figure 4.10 a and b) and numerical dissipation is strongly dependent on the horizontal grid (Figure 4.11 c and d and Figure 4.13 c and d). That is, as a grid is vertically refined, numerical diffusion decreases and horizontal refinement decreases numerical dissipation. Indeed, the numerical dissipation in fine horizontal grids is such that the numerical viscosity is on the order of molecular viscosity. It is an expensive task to have a nearly numerically dissipative free model (e.g. a grid with 1200 cells per wavelength; for this basin a horizontal grid of 600). However, considering turbulent eddy viscosities where it is supposed the eddy viscosity is 100 times the molecular viscosity, all of the grids examined would have smaller numerical viscosities than the eddy viscosity (Figure 4.13). Even if the eddy viscosity is 10 times the molecular viscosity, several grids (30×73, 60×73, 60×15, 600×15 and 600×29) would have numerical viscosities less than the eddy viscosity. This shows that coarser grid resolutions may still produce a model that performs well with respect to numerical viscosity when compared with eddy viscosity. It is speculated that with numerical viscosities lower than eddy viscosity, then the numerical dissipation (Figure 4.11) could be considered small. Following, a model with low numerical dissipation would have its' skill controlled by numerical diffusion.

The non-hydrostatic model's representation of internal wave evolution closely matched the evolution seen in the laboratory experiment. The wavelength and amplitude is approximately the same for different resolutions. The non-hydrostatic model also shows a shift in peak power to the characteristic wavelength of the solitons. This shift occurs at all grid resolutions and is an indication of the non-hydrostatic model's ability to capture the physics of internal wave evolution. The non-hydrostatic model was not able to always capture the numbers of observed solitons occurring in the wave train. This difference is most likely due to an issue with numerical dispersion. Numerical dispersion is

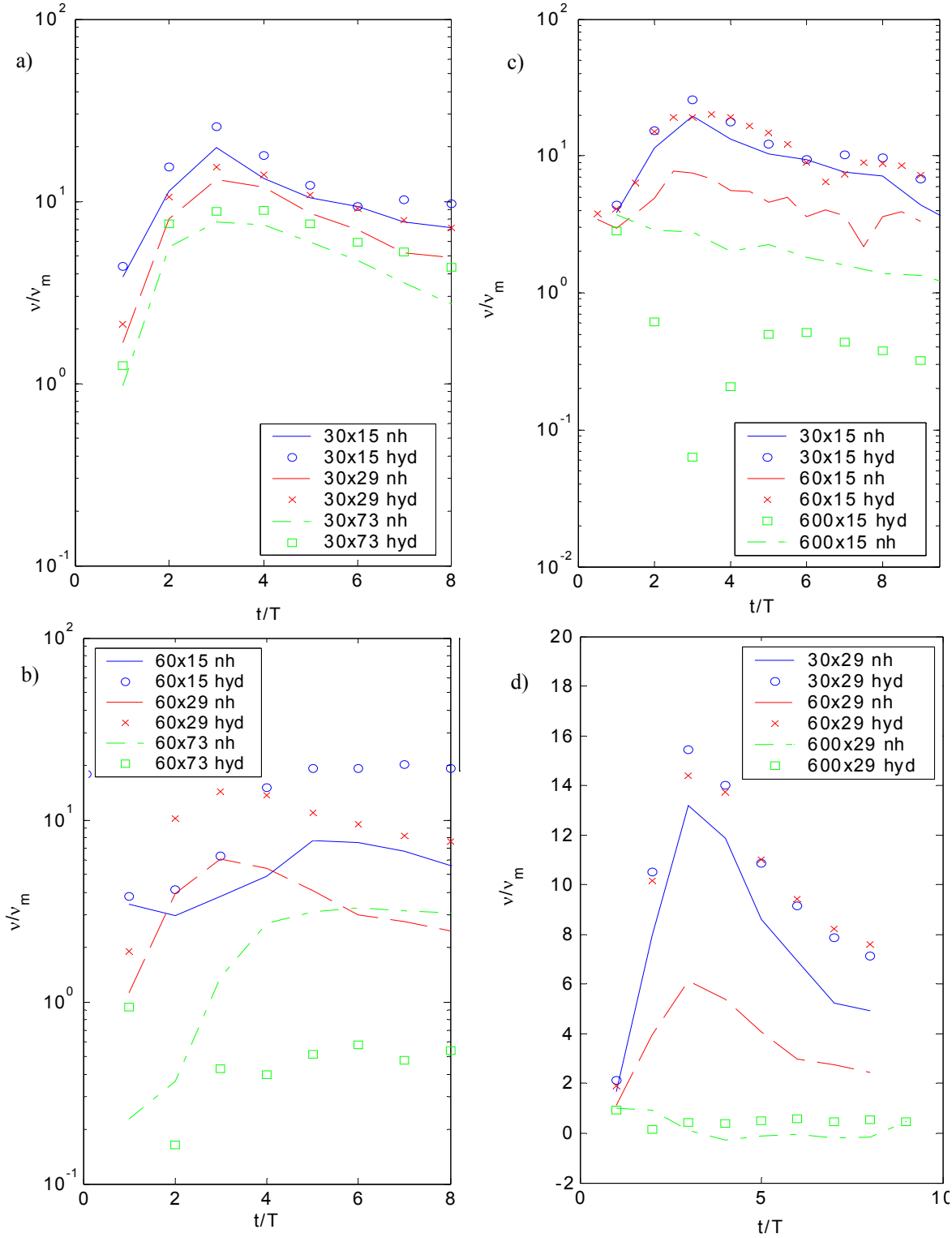

Figure 4.13: Numerical viscosity (υ) of scenario 2 for different grids. a) Horizontal grid = 30, b) horizontal grid = 60, c) vertical grid = 15, d) vertical grid = 29. Lines represent non-hydrostatic model results (nh), markers represent hydrostatic model results (h). Note, d) the ordinate is not log scale because the numerical viscosity includes negative values. $\nu_m = 10^{-6}$ m2/s.

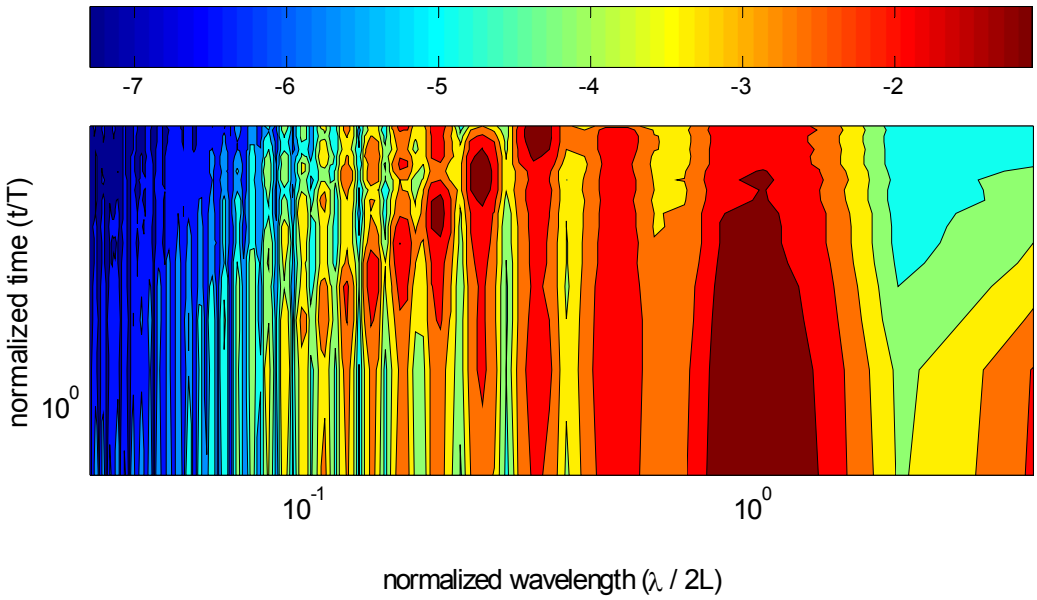

Figure 4.14: Representative power spectral density for non-hydrostatic model of scenario 2. The colorbar represents the $\log_{10}$ relative PSD.

affected by discretization methods in time, which were not analyzed in the present research; it remains a point of interest for future research. The hydrostatic model did not show the soliton development observed in the laboratory experiment. Analysis of the power spectral density shows the hydrostatic model retains most of the wave's energy within the bore (represented as the initial wavelength wave in Figure 4.15). Small soliton-like formations were observed behind the bore, but the peak power is not shifted to them (Figures 4.15 and 4.16). The soliton-like formations vary for different horizontal grid resolutions in both amplitude and wavelength. The soliton-like formations are considered an artifact of the model and grid resolution because the soliton-like formations differ significantly from the laboratory experiment, vary with the grid resolution and the peak power is not transferred to them. It is thought that the hydrostatic model will continue to change the soliton train characteristics with grid refinement.

4.2 Lake-Scale Comparison

The hydrostatic and non-hydrostatic models were applied to a lake-scale comparison to demonstrate model performance on a larger scale than the laboratory experiment. Most of the previously developed non-hydrostatic models (e.g. Stansby and Zhou, 1998; Chen, 2003) do not attempt real-world scale problems. Those that do (Marshall, et al., 1997; Casulli, 1999), do not model internal waves. Thus, testing the behavior of a non-hydrostatic model on a larger-scale internal wave has not previously been done. Similar to §4.1.3, the grid is varied and the analytical methods of §2.2 are used to quantify the effect of grid resolution on the model's skill.

4.2.1 Setup

A 2D closed basin with length (L) of 12500 m and height (H) of 50 m was chosen as representative of a medium-sized lake (Delavan, 2003). The initial wave shape was a cosine and the density field was constructed with a three-layer hyperbolic tangent function [Equation (2.34)]. The density difference across the pycnocline was varied to assess the effect of density gradient on model performance. The amplitude ratio (a/h) was 0.3 and the depth ratio (h/H) was 0.3. The wave used in this simulation has amplitude and depth ratios that indicate steepening and soliton formation should occur (i.e. regime 2). Several different grid meshes were examined, as listed in Table 4.5. The timestep used was based on Equation (1.13); this will be discussed further in §4.2.2 ff. Each simulation was conducted over 100 wave periods. The inviscid/diffusionless approximation was used.

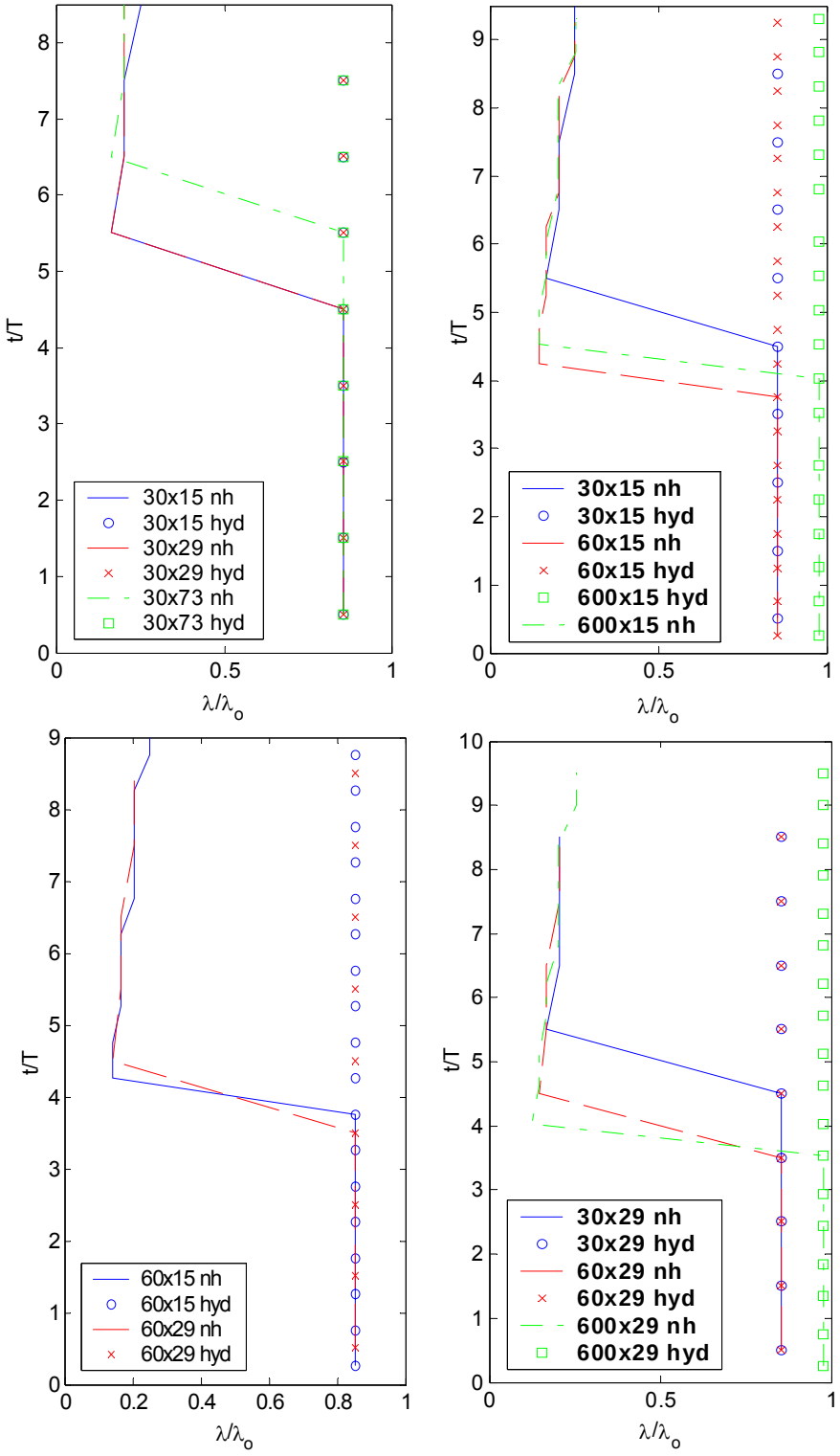

Figure 4.15: Wavelength with peak PSD of scenario 2 for different grids. a) Horizontal grid = 30, b) horizontal grid = 60, c) vertical grid = 15, d) vertical grid = 29. Lines represent non-hydrostatic model results (nh), markers represent hydrostatic model results (hyd).

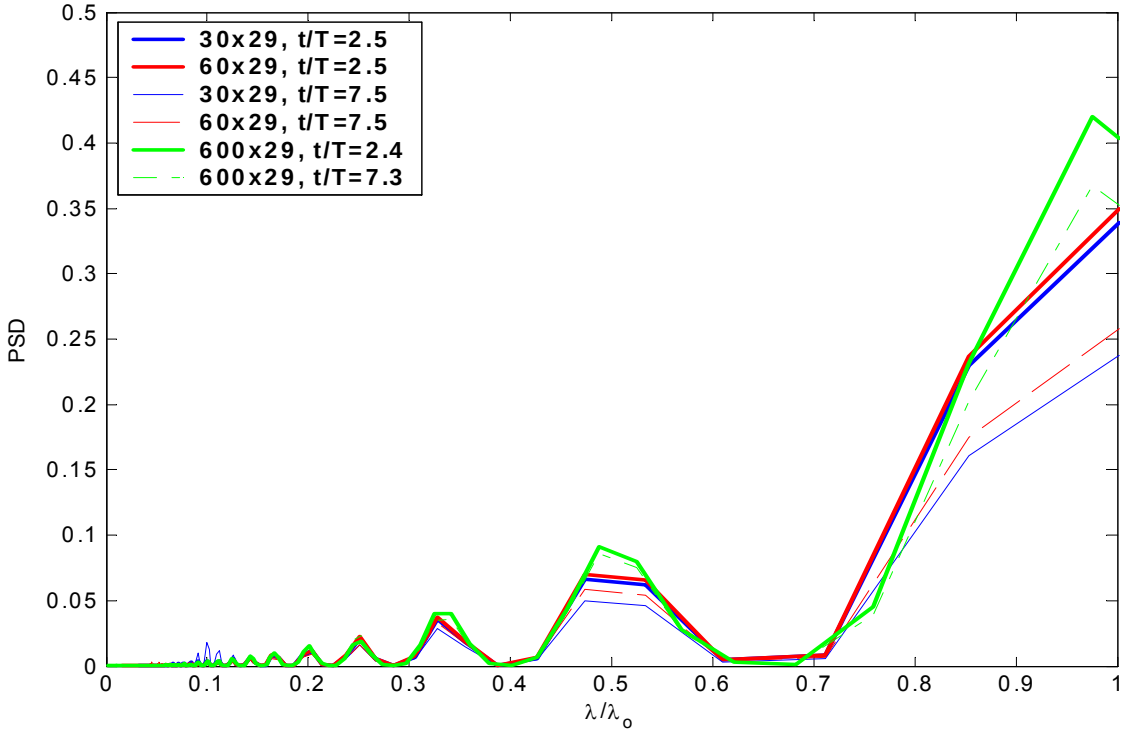

Figure 4.16: Typical timeslices of PSD for hydrostatic model simulation of scenario 2 at t/T = 2.5 and t/T = 7.5.

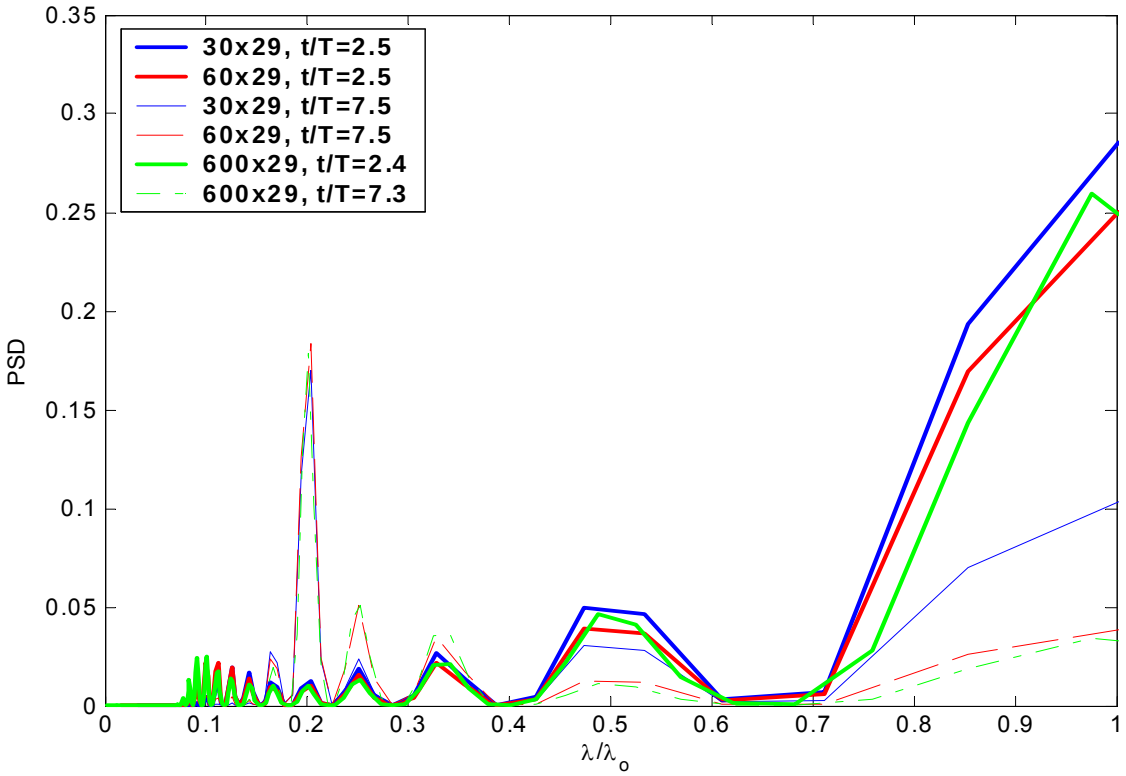

Figure 4.17: Typical timeslices of PSD for non-hydrostatic simulation of scenario 2 at t/T = 2.5 and t/T = 7.5.

Table 4.5: Grid meshes for lake scale comparison. Those meshes with an 'x' were performed; nh indicates that only the non-hydrostatic model was used.

	# Cells in Z-dir			
# Cells in X-dir	9	27	81	$\lambda_o/\Delta x$
9	x	x	x	18
27	x	x	x	54
81	nh	nh	x	160
$h_{py}/\Delta z$	1	3	9	

Results

Results are analyzed for nine simulations using the loss of dynamic energy (Figure 4.19), computed numerical viscosity (Figure 4.20), change in background potential energy (Figure 4.21), computed numerical diffusivity (Figure 4.22) and the peak power spectral density (Figure 4.23). As a note to the results, the finest horizontal grid went completely unstable for all vertical resolutions (81×9, 81×27, 81×81), as seen in the E_B, E_D, numerical diffusivity and viscosity in Figures 4.19 - 4.22. The vertical advective CFL:

$$CFL_{advective-z} \equiv w\frac{\Delta t}{\Delta z} \qquad (1.17)$$

was greater than one, indicating the presence of strong vertical motions. The Euler-Lagrange Method is stable for hydrostatic models (Hodges, 2000), but the stability has not been investigated in this research or elsewhere in literature for non-hydrostatic models. Reducing the timestep to adhere to Equation (1.14) did not mitigate the instability. The addition of viscosity had no effect on the instability either. This issue is discussed further in §4.2.3.

The internal wave initially steepens with small, soliton-like features developing (Figure 4.18) and is damped out after ten wave periods. The system is dissipative, losing an order of magnitude of dynamic energy in less than ten wave periods for all grid resolutions (Figure 4.19). The large numerical dissipation accounts for the damping effect observed on the wave's evolution. For vertical and horizontal grid refinement, there is nearly the same loss in dynamic energy for the first three wave periods. After this time, grid refinement causes more dynamic energy to be dissipated. The most significant differences in dynamic energy amongst grid resolutions were due to refinement in the vertical grid. The decrease in dynamic energy in the lake-scale simulations is comparable to the laboratory-scale hydrostatic simulations (i.e. the dynamic energy decreases about an order of magnitude in ten wave periods). However, in the laboratory-scale

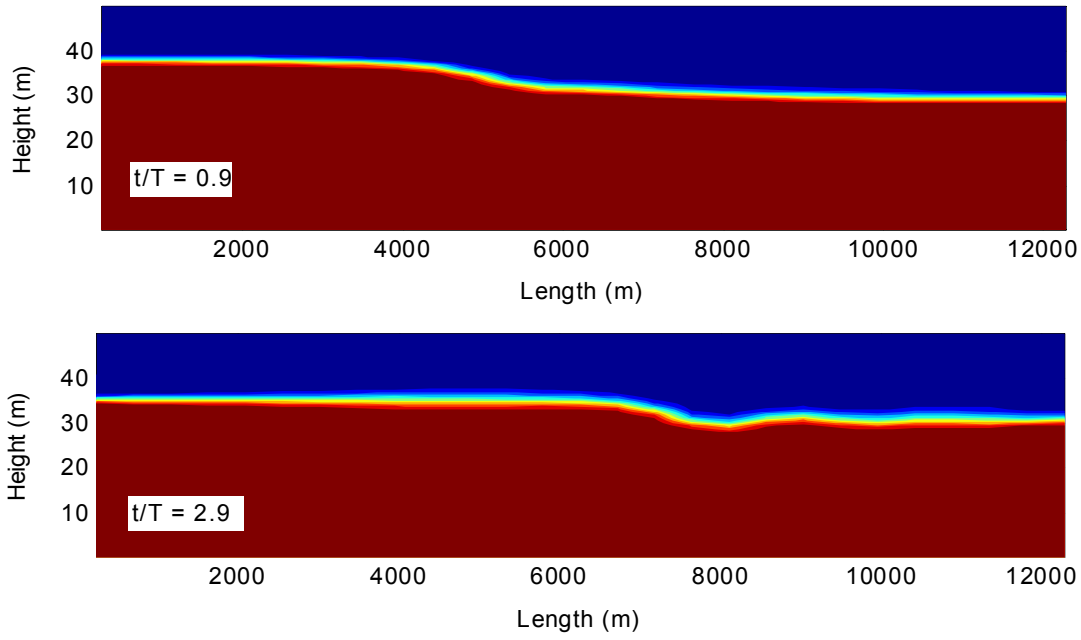

Figure 4.18: Internal wave evolution for lake-scale case at t/T = 0.9 and t/T = 2.9.

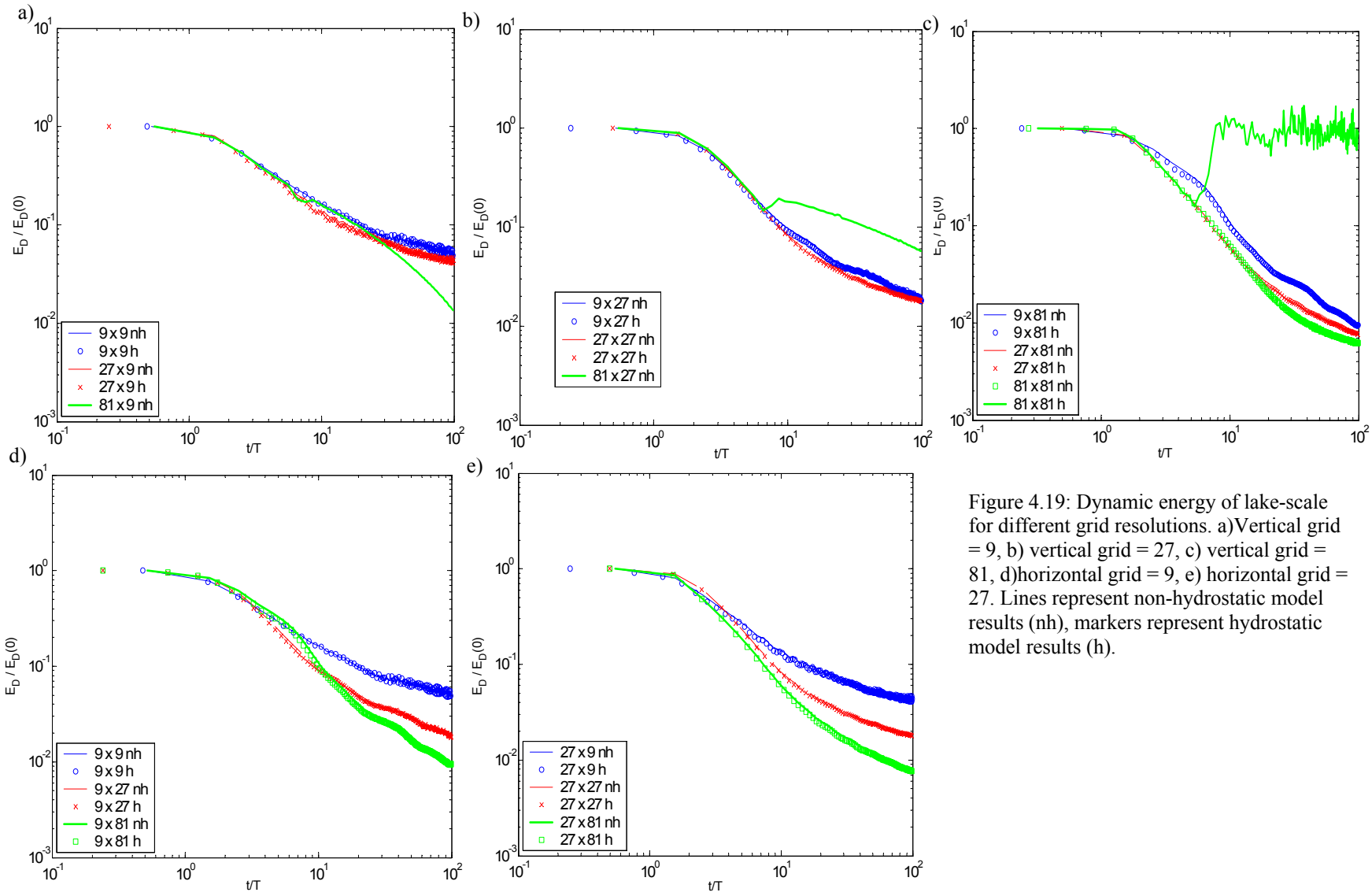

Figure 4.19: Dynamic energy of lake-scale for different grid resolutions. a)Vertical grid = 9, b) vertical grid = 27, c) vertical grid = 81, d)horizontal grid = 9, e) horizontal grid = 27. Lines represent non-hydrostatic model results (nh), markers represent hydrostatic model results (h).

non-hydrostatic model simulations had less numerical dissipation than the hydrostatic model and horizontal grid refinement dominated changes in numerical dissipation, which was not seen in the lake-scale simulations. After about ten wave periods, the numerical viscosity (Figure 4.20) becomes scattered. At ten wave periods the wave is damped, so there are small velocities and subsequently low numerical dissipation. Therefore, after ten wave periods, small fluctuations in the dynamic energy are amplified resulting in scatter. This scatter is irrelevant to the present research as we are interested in wave evolution before damping. All grids show the numerical viscosity initially increase and then decrease after two or three wave periods (Figure 4.20). This is similar to the laboratory-scale results (§4.1.3). Vertically refined grids (Figure 4.20 d and e) showed lower values for the numerical viscosity, similar to the laboratory-scale results; there was not a significant difference in the numerical viscosity for horizontally refined grids, which was not seen in the laboratory-scale results. One other difference between the lake-scale and laboratory-scale results for numerical viscosity is that the numerical viscosity for the lake-scale simulations were over 100 times greater than molecular viscosity, while the laboratory-scale simulations' numerical viscosity never exceeded 30 times molecular viscosity.

The growth in background potential energy is greater for horizontal grid refinement and less for vertical grid refinement (Figure 4.21) similar to the laboratory-scale. Vertical grid refinement dominates changes in numerical diffusion over different grid resolutions. The normalized change in E_B increases above unity and is considered unphysical around three wave periods for the coarsest vertical grid. The finest vertical grid has a change in E_B from ~ 0.01 to 0.4 over 100 wave periods (Figure 4.21 d and e). Changes in the horizontal grid have a relatively small effect on the growth of E_B. Likewise, the numerical diffusivities (Figure 4.22) decrease by an order of magnitude for vertical grid refinement, while horizontal refinement produces relatively similar numerical diffusivities (Figure 4.22). This confirms the vertical grid as the controlling mechanism of numerical diffusion, which is the same result in the laboratory-scale simulations (§4.1.3).

The power spectral density (Figure 4.23) shows a shift in peak power around ten wave periods; the wavelength with peak power varies with the grid resolution. A coarse horizontal grid (e.g. Figure 4.23a) shows all power shifting to the same wavelength ($\lambda/\lambda_o \sim 0.5$) for different vertical resolutions. For a finer horizontal resolution, as the grid is vertically refined (Figure 4.23 b), the peak power shifts to smaller wavelengths ($\lambda/\lambda_o = 0.2$) and gradually moves back towards larger wavelengths ($\lambda/\lambda_o = 0.5$) as time progresses. However, unlike the laboratory-scale simulations where the peak power shifted to the same wavelengths irrespective of the grid resolution, the peak power shifts to different wavelengths when the grid is horizontally refined (Figure 4.23 c-e).

Application of the non-hydrostatic model generates nearly identical results to the hydrostatic model. The only two grid resolutions that showed any difference between the hydrostatic and non-hydrostatic models were the 27×9 and 9×27 grids. Figures 4.21 and 4.22 show that the 27×9 and 9×27 grids had less diffusion in the non-hydrostatic model than the hydrostatic model. After ten wave periods, the background potential energy in the non-hydrostatic model converges to the background potential energy in the hydrostatic model. The numerical diffusivities in the non-hydrostatic model are less than the numerical diffusivities for the hydrostatic model for the entire 100 wave period simulation.

The density gradient across the pycnocline was varied ($\Delta\rho$ = 0.1, 1.0 and 10.0 kg/m^3) to asses its effect on the modeling of internal waves. There is no significant difference between hydrostatic and non-hydrostatic simulations for the identical grid resolution (Figure 2.24).

4.2.2 Discussion

Long (1972) states that there is a relationship between nonlinearity and non-hydrostatic pressure; a sufficiently steep wave has significant non-hydrostatic effects affecting the internal wave evolution. The wave simulated in this section is nonlinear and lies within regime 2 (a/h = 0.3, h/H = 0.3). Thus, non-hydrostatic pressure effects should disperse the steepened wave and have different numerical error behavior than the hydrostatic model. However, the results show the non-hydrostatic model is nearly identical in all grid resolutions to the hydrostatic model. The similarity between the hydrostatic and non-hydrostatic models can be explained by grid resolution. Grid resolution plays a key role in how the non-hydrostatic pressure affects internal wave evolution. The model grid can only represent a single, average non-hydrostatic pressure for a single cell. Thus, for cells with small grid aspect ratios (i.e. 9×9: aspect ratio = 4[10^{-3}]; 9×81:

aspect ratio = 4[10^{-4}]), the non-hydrostatic pressure effect is muted. The 27×9 grid has the largest grid aspect ratio (0.012) of all the grids successfully applied to the lake-scale wave. This grid resolution did show small differences in numerical diffusion (in terms of the background potential energy and numerical diffusivity) between the hydrostatic and non-hydrostatic models. It is believed by this author, if finer grid resolutions with larger aspect ratios had remained stable (i.e. the 81×9 and 81×27 cases), these cases would have shown effects from the inclusion of non-hydrostatic pressure.

The mechanism causing the model instability for fine horizontal grid resolutions is presently unknown. The timestep is not controlling vertical motions, unlike the laboratory case (§4.1.1), so this is not a simple CFL issue. There are several possible sources of error for this instability. There may be an error in the non-hydrostatic model that was only detected in this situation. The most likely possibility is the use of the explicit Euler discretization for the baroclinic term in CWR-ELCOM. While explicit Euler discretizations are unstable, they have been successfully applied as part of models, such as CWR-ELCOM where truncation error serves as stabilization. Stability is clearly only a problem with the non-hydrostatic pressure solution as the hydrostatic model remains stable under all tested conditions. The issue with stability may be due to the decrease in numerical dissipation seen in the laboratory-scale simulation. Another possibility for this instability could be a more global problem with the application of the fractional-step method for internal wave evolution. While several other non-hydrostatic models have used the fractional-step method, there has been no reported work on grid refinement and very little work on internal wave modeling. Most of the known non-hydrostatic models (Mahadevan, et al. 1996a, b; Marshall, et al., 1997; Stansby and Zhou, 1998; Casulli, 1999; Chen, 2003) do not explicitly model internal waves and present results only for laboratory scale problems. If lake or ocean scale problems are investigated, only the general circulation patterns and free-surface elevations are reported. Daily and Imberger (2003) model internal waves, however only on the laboratory scale. None of the aforementioned models present results for more than one grid mesh. Stability at fine resolutions in a large domain remains an open issue for future research.

4.3 Summary

The non-hydrostatic model laboratory-scale simulations in the present work compared well with the theory and laboratory experiments of Horn. Horn, et al. (2001) examined data from several published field studies and confirmed the applicability of the theoretical timescales used to develop a regime diagram. Therefore, it is inferred that the results of the laboratory-scale model simulations are relevant to real-world scale basins.

The non-hydrostatic model provides a substantially better representation of internal wave evolution than the hydrostatic model for laboratory scales. The features of internal wave development (such as soliton formation) are physical in the non-hydrostatic model, while a function of the grid resolution in the hydrostatic model. There is no appreciable difference between the hydrostatic and non-hydrostatic model for weakly nonlinear, and subsequently weakly non-hydrostatic waves. In cases with a strongly nonlinear, non-hydrostatic wave on a sufficiently fine grid, such as in the laboratory simulations, the non-hydrostatic pressure effect is significant. The addition of non-hydrostatic pressure disperses the nonlinearly steepening initial wave into a train of solitons, as observed in the laboratory, and captures the energy cascade through the wave train. Adding non-hydrostatic pressure does not eliminate numerical error, but it does change the characteristics of model error; numerical diffusion is the mechanism that determines model skill, whereas the hydrostatic model is numerically dissipative.

The largest grid aspect ratio applied to the lake scale case for a stable non-hydrostatic simulation is 0.012 (27×9 grid). The largest grid aspect ratio applied to scenario 2 is 2.0 (600×15 grid), and the smallest grid aspect ratio is 0.02 (30×73 grid). It is deduced from the results of the laboratory scale and lake scale cases that a non-hydrostatic model needs a sufficiently large grid aspect ratio [$\Delta z/\Delta x > O(10^{-2})$] to affect internal wave evolution.

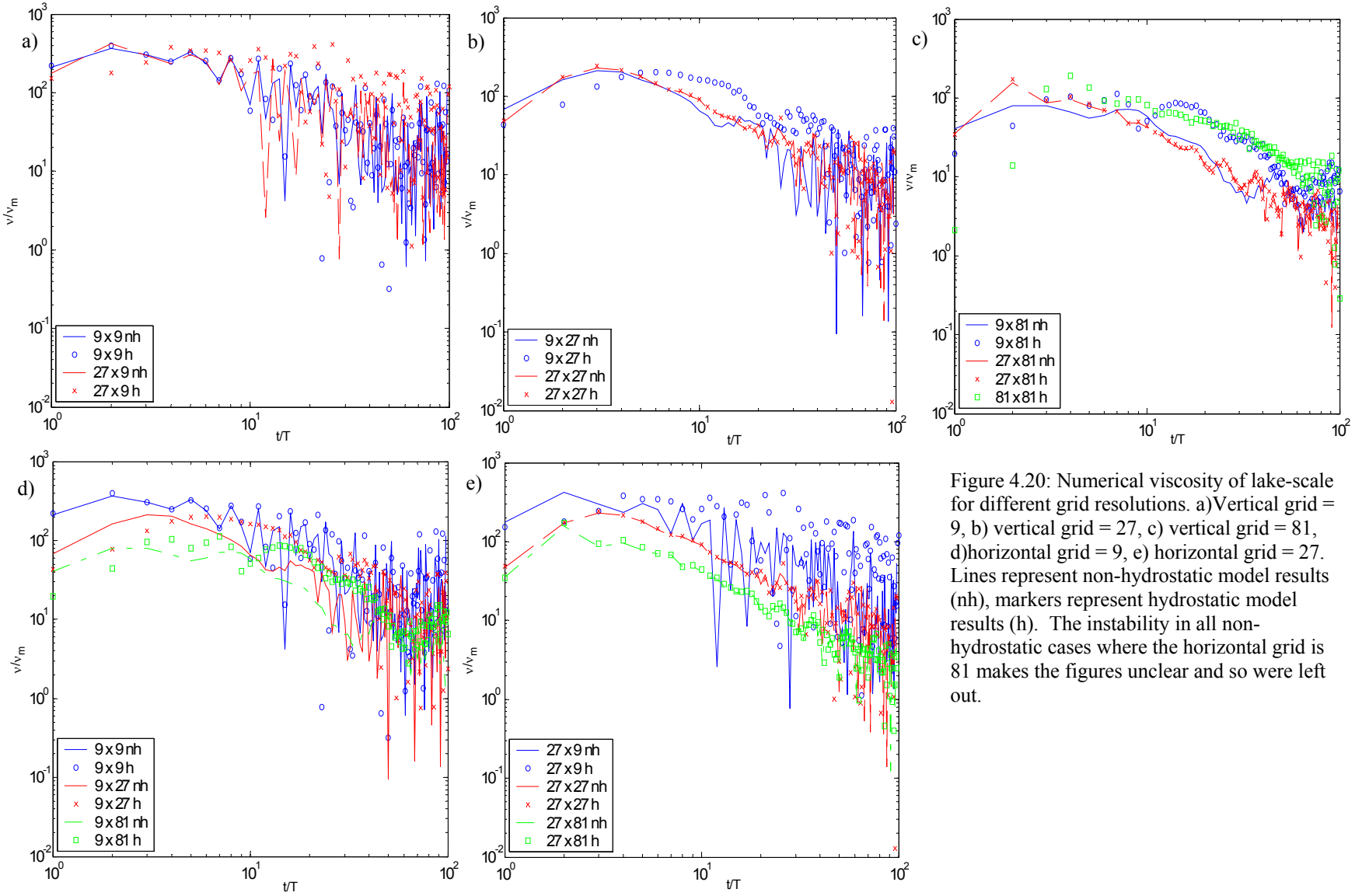

Figure 4.20: Numerical viscosity of lake-scale for different grid resolutions. a)Vertical grid = 9, b) vertical grid = 27, c) vertical grid = 81, d)horizontal grid = 9, e) horizontal grid = 27. Lines represent non-hydrostatic model results (nh), markers represent hydrostatic model results (h). The instability in all non-hydrostatic cases where the horizontal grid is 81 makes the figures unclear and so were left out.

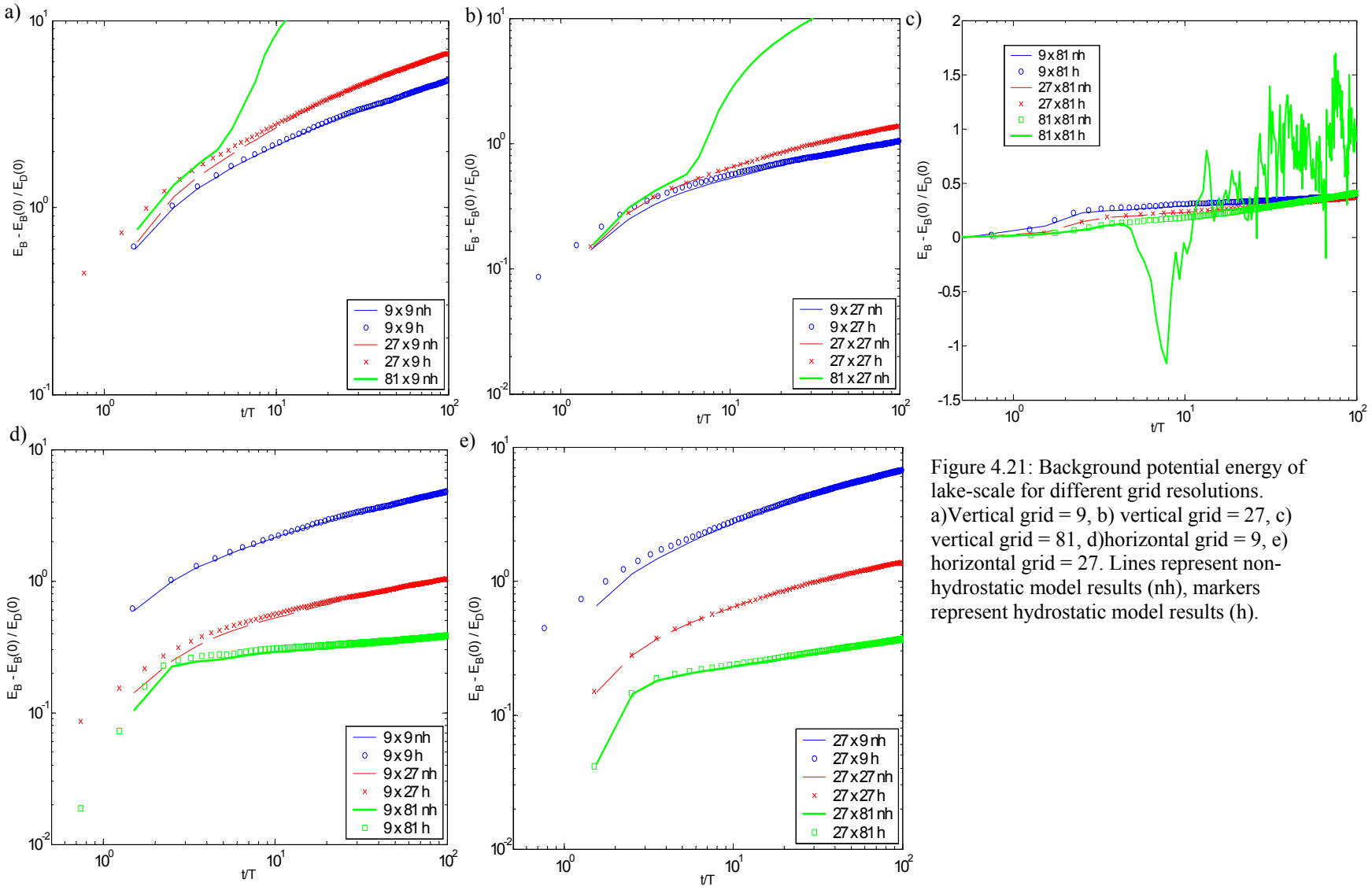

Figure 4.21: Background potential energy of lake-scale for different grid resolutions. a)Vertical grid = 9, b) vertical grid = 27, c) vertical grid = 81, d)horizontal grid = 9, e) horizontal grid = 27. Lines represent non-hydrostatic model results (nh), markers represent hydrostatic model results (h).

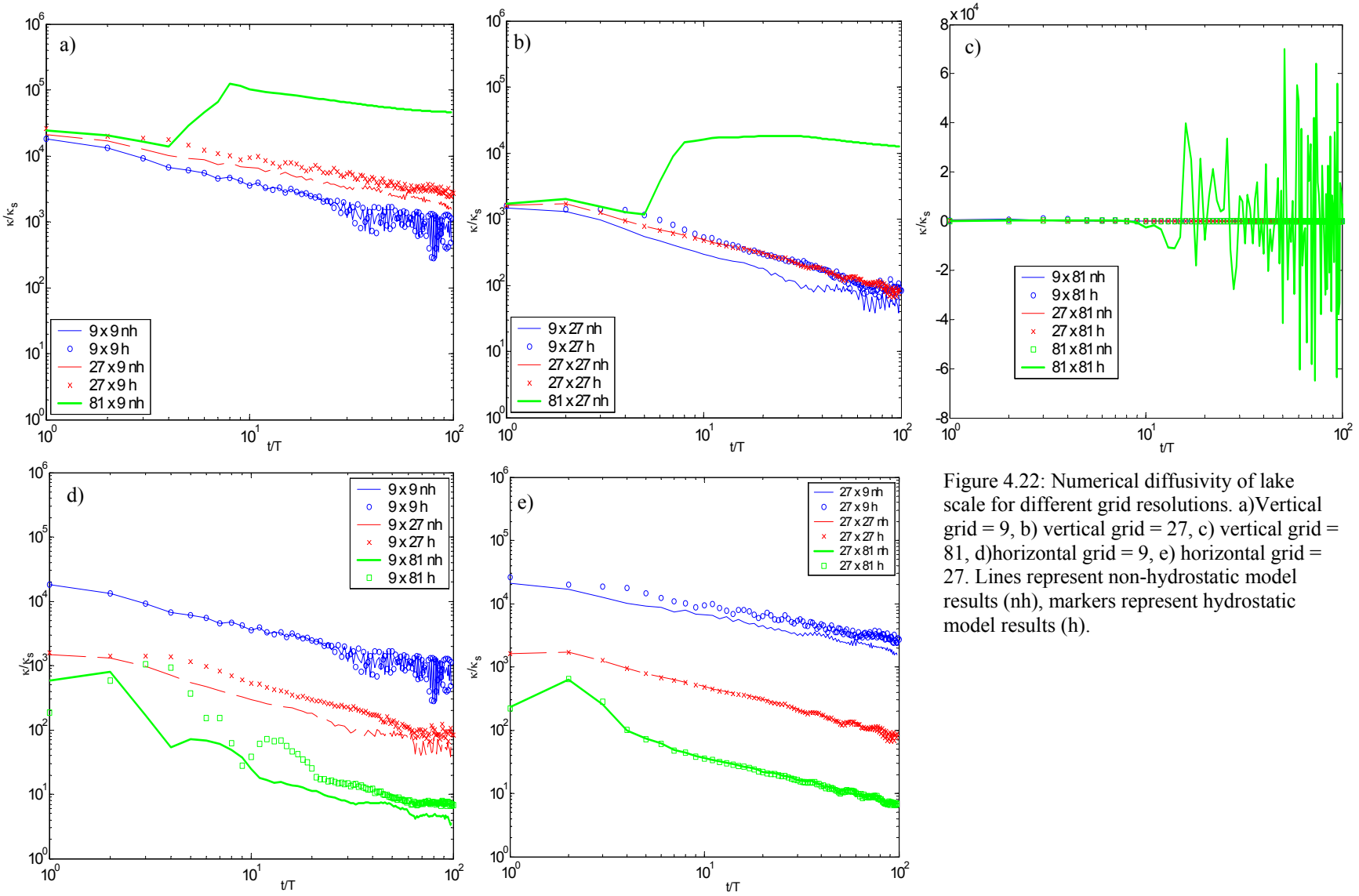

Figure 4.22: Numerical diffusivity of lake scale for different grid resolutions. a)Vertical grid = 9, b) vertical grid = 27, c) vertical grid = 81, d)horizontal grid = 9, e) horizontal grid = 27. Lines represent non-hydrostatic model results (nh), markers represent hydrostatic model results (h).

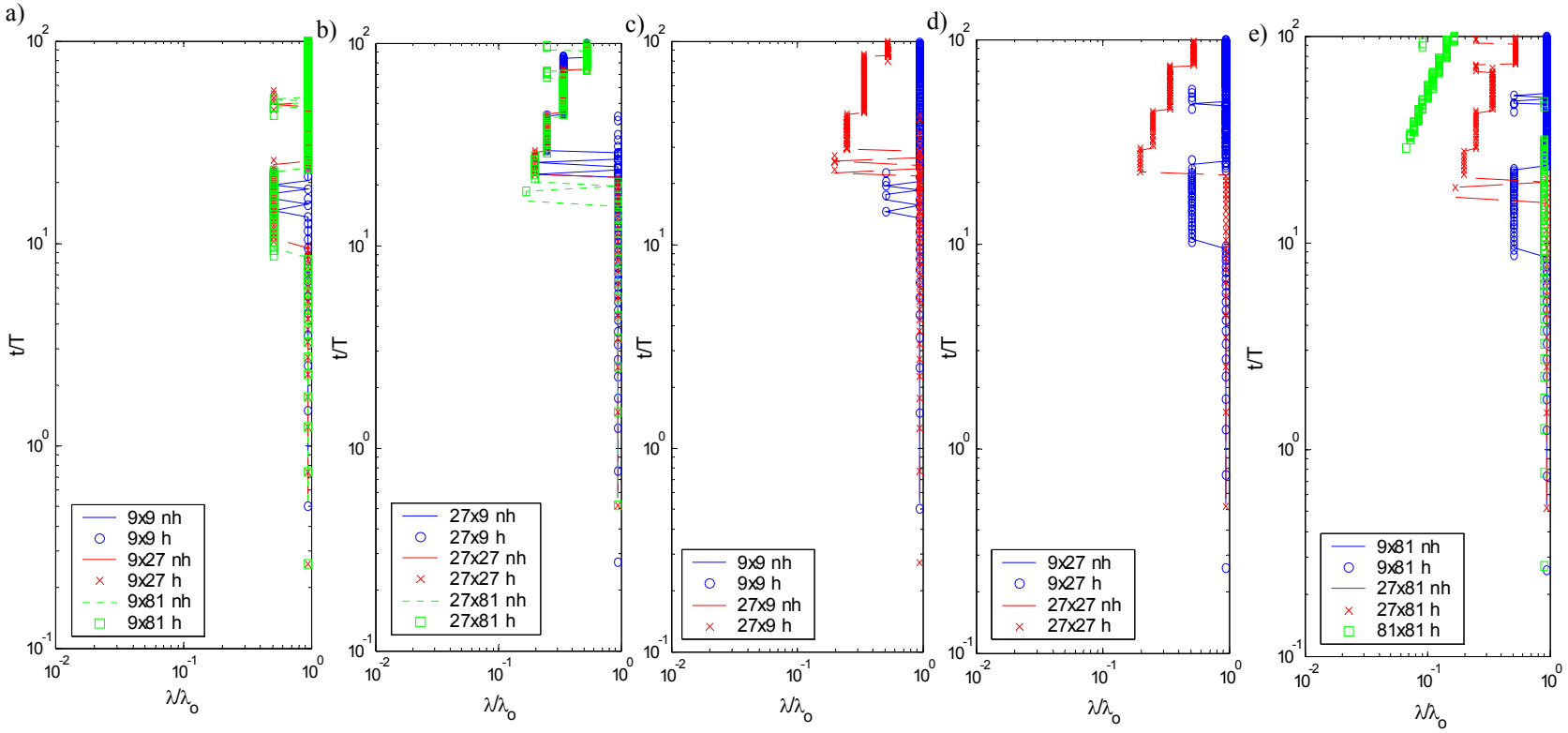

Figure 4.23: Wavelengths with peak PSD of lake-scale for different grid resolutions. a)Horizontal grid = 9, b) horizontal grid = 27m c)vertical grid = 9, d) vertical grid = 27, e) vertical grid = 81. Lines represent non-hydrostatic model results (nh), markers represent hydrostatic model results (h).

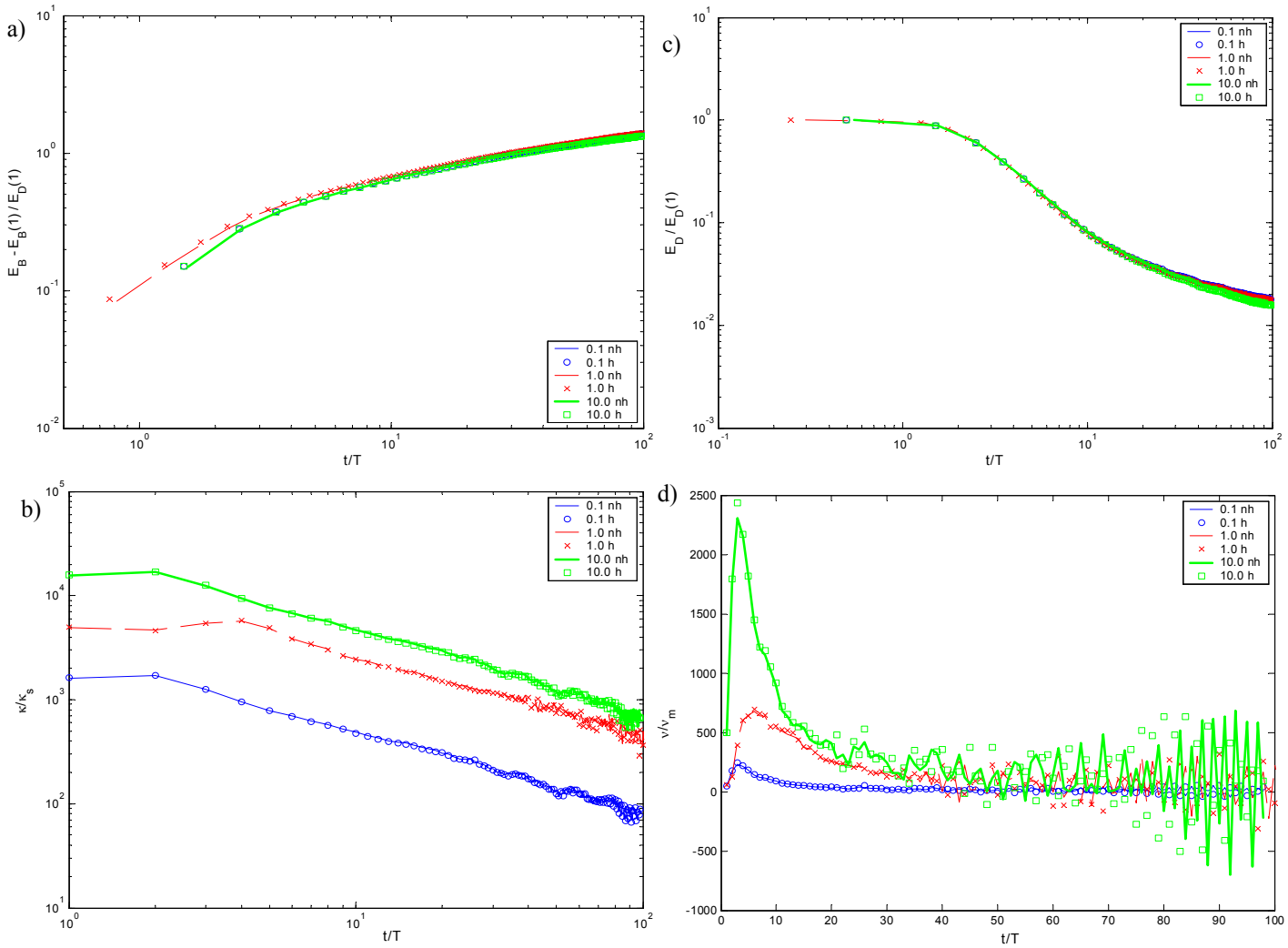

Figure 4.24: Varying the density gradient of the lake-scale simulation. a)Background potential energy, b) numerical diffusivity, c) dynamic energy, d) numerical viscosity. Lines represent non-hydrostatic model results (nh), markers represent hydrostatic model results (h).

Chapter 5. Isolation of non-hydrostatic effects

In environments with hydrostatic aspect ratios (e.g. oceans, estuaries, lakes), non-hydrostatic pressure gradients are only locally significant, such as at steep wave fronts. Stansby and Zhou (1998) discussed this issue and suggested isolating regions of significant non-hydrostatic pressure gradients; however, they neither identified regions of non-hydrostatic behavior nor provided a local solution for the non-hydrostatic pressure. The present research builds the foundations for linking hydrostatic models with local non-hydrostatic solutions to yield practical simulations of non-hydrostatic internal wave behavior. This chapter presents a new method for identifying local regions where the non-hydrostatic pressure is expected to be significant. The key advance in the state-of-the-art is that the non-hydrostatic region is demonstrated to be identifiable using only a hydrostatic solution. Thus, this method could be used to allow the application of a local non-hydrostatic solver where necessary, while "hydrostatic" areas are more simply computed with a hydrostatic model. The ability to "boot-strap" from simpler hydrostatic methods to non-hydrostatic methods should allow faster solution than global application of non-hydrostatic methods. The development of a local non-hydrostatic solver remains an issue for further research (§6 ff.), so the present work can be seen as a necessary development of foundational methods.

As a wave propagates, the fluid around the wave front is pushed away from the wave front (Figure 5.1); this is where the strongest vertical velocities are located (Daily and Imberger, 2003). The strong vertical velocities cause the wave to behave more nonlinearly, and subsequently, more non-hydrostatically. Thus, the vertical acceleration is used to identify local regions with non-hydrostatic behavior. The new non-hydrostatic pressure isolation approach is based on the separation of hydrostatic and non-hydrostatic pressure solutions in the fractional-step method, so that the regions with non-hydrostatic behavior are *a priori* identified from the hydrostatic solution. The hydrostatic solution provides the vertical acceleration used in the non-hydrostatic pressure isolation method. A non-hydrostatic parameter obtained from the non-hydrostatic pressure isolation method characterizes a cell as hydrostatic or non-hydrostatic. This chapter provides the numerical theory used to develop the non-hydrostatic pressure isolation method and an application of the method for two different waves. Further, the non-hydrostatic pressure isolation method is applied to one wave on three different grid resolutions to assess the effect of grid resolution on the non-hydrostatic pressure isolation method.

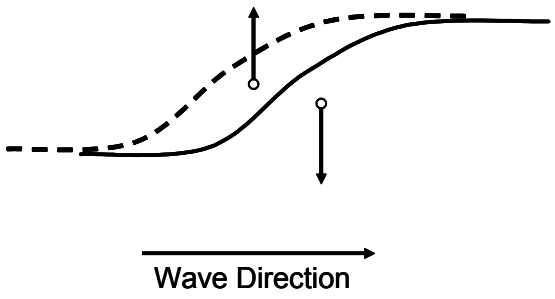

Figure 5.1: Direction of vertical velocities for a horizontally propagating wave front.

5.1 Numerical Theory

The governing equations (see §2.1.1) yield a vertical momentum equation for inviscid flow:

$$\frac{DW}{Dt} = -\frac{1}{\rho_o}\frac{\partial P_{nh}}{\partial z} \qquad (5.1)$$

This equation is a relationship between vertical acceleration and the non-hydrostatic pressure vertical gradient, which ordinarily exists only for a non-hydrostatic model. The vertical velocity (W) is representative of a flow field that accounts for non-hydrostatic pressure. In a hydrostatic model, the non-hydrostatic pressure is neglected and Equation (5.1) is not modeled. The hydrostatic vertical velocity is computed diagnostically by enforcing the continuity equation (see §2.1.1). The non-hydrostatic pressure isolation method uses the hydrostatic vertical velocity and the relationship in Equation (5.1) to approximate the non-hydrostatic pressure.

$$\frac{DW^*}{Dt} = -\frac{1}{\rho_o}\frac{\partial P_{nh}}{\partial z} \qquad (5.2)$$

W* is the hydrostatic vertical velocity; this is the same vertical velocity used in Equation (2.7). Therefore, the left-hand side of Equation (5.2) is known after the hydrostatic model is applied; the right-hand side is unknown and is approximated with the non-hydrostatic pressure isolation method. A comparison of the hydrostatic vertical acceleration (DW^*/Dt) and the modeled non-hydrostatic pressure vertical gradient is seen in Figure 5.2. The hydrostatic vertical acceleration is the approximated

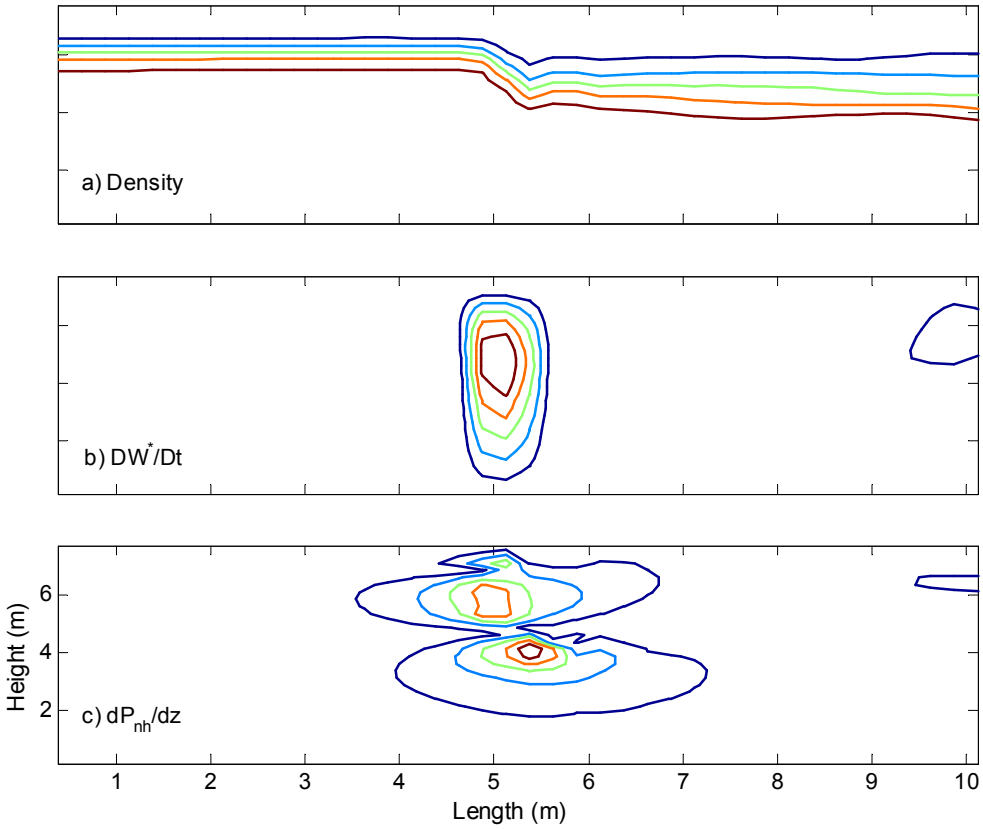

Figure 5.2: Comparison of hydrostatic/non-hydrostatic vertical momentum terms. a) Density profile; b) hydrostatic vertical acceleration; c) modeled non-hydrostatic pressure vertical gradient. The main non-hydrostatic influence is at the steep wave front. There is also some non-hydrostatic effect on the right side of b and c.

non-hydrostatic pressure vertical gradient. Note, 'modeled' refers to anywhere the non-hydrostatic model is used and 'approximated' refers to when the hydrostatic model is used to make an approximation of the non-hydrostatic pressure. The location of peak values for the approximated non-hydrostatic pressure vertical gradient is a reasonable match for the peak modeled non-hydrostatic pressure vertical gradients. The approximated and modeled non-hydrostatic pressure vertical gradients are symmetrical around the wave front, although the modeled non-hydrostatic pressure vertical gradient shows a slightly wider range of influence around the steep wave front. Aside from the principle wave front, there is some steepening associated with a higher mode wave at the right end of the basin in Figure 5.2. Both the approximated and modeled non-hydrostatic pressure vertical gradients identify this location.

Horizontal flow dominates internal wave propagation and is prognostically determined in hydrostatic models, thus it is practical to use the horizontal momentum equation in the development of the non-hydrostatic pressure isolation method. The non-hydrostatic horizontal momentum equation contains the non-hydrostatic pressure horizontal gradient:

$$\frac{DU}{Dt} = -g\left(\frac{\partial \eta}{\partial x} + \frac{1}{\rho_o}\frac{\partial}{\partial x}\int_{z'}^{\eta}\tilde{\rho}\,dz\right) - \frac{1}{\rho_o}\frac{\partial P_{nh}}{\partial x} \qquad (5.3)$$

The non-hydrostatic pressure horizontal gradient is not known in a hydrostatic model, but an approximation of the non-hydrostatic pressure horizontal gradient effect is required to identify regions of significant non-hydrostatic behavior. The approximation for the non-hydrostatic vertical gradient can be used to estimate the non-hydrostatic pressure horizontal gradient. Vertically integrating Equation (5.2) produces an approximation of the non-hydrostatic pressure:

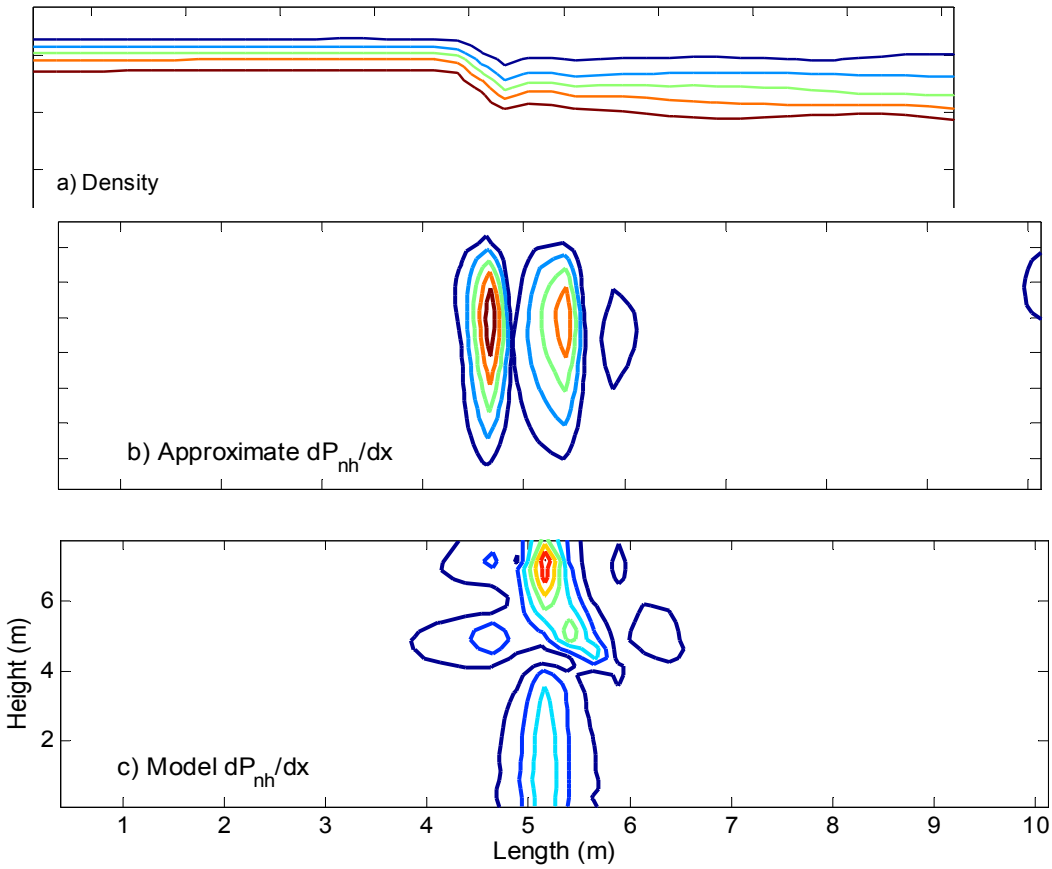

Figure 5.3: Comparison of non-hydrostatic pressure horizontal gradient. a) Density profile; b) approximate non-hydrostatic pressure horizontal gradient; c) model non-hydrostatic pressure horizontal gradient.

$$P_{nh} = -\rho_o \int \frac{DW^*}{Dt} dz \qquad (5.4)$$

The horizontal spatial derivative of the approximated non-hydrostatic pressure [Equation (5.4)] is:

$$\frac{\partial}{\partial x} \int \frac{DW^*}{Dt} dz = -\frac{1}{\rho_o} \frac{\partial P_{nh}}{\partial x} \qquad (5.5)$$

Equation (5.5) approximates the non-hydrostatic pressure horizontal gradient, as seen in Figure 5.3. Similar to the non-hydrostatic pressure vertical gradient, the approximated non-hydrostatic pressure horizontal gradient matches the occurrence of the modeled non-hydrostatic pressure horizontal gradient at the steep wave front.

A screening parameter is developed to quantify the relevance of the approximated non-hydrostatic pressure with regards to its influence on internal wave evolution, thereby identifying regions where the non-hydrostatic effect is large. The screening parameter relates the non-hydrostatic pressure horizontal gradient to other terms within the horizontal momentum equation that influence internal wave evolution. Where the screening parameter is large, that location is considered to have significant non-hydrostatic behavior.

Non-hydrostatic pressure effects are linked to the nonlinearity of a wave and are propagated at the speed of the wave (§6 ff.). As the non-hydrostatic pressure gradients are strongest at the wave front, their relative importance on internal wave evolution is dependent on how the non-hydrostatic pressure gradient scales with the horizontal acceleration. Therefore, the screening parameter that isolates

regions of non-hydrostatic behavior compares the non-hydrostatic horizontal gradient to the hydrostatic horizontal acceleration (DU^*/Dt):

$$\gamma \equiv \frac{\left(-\frac{1}{\rho_o}\frac{\partial P_{nh}}{\partial x} \right)}{\left(\left.\frac{DU^*}{Dt}\right|_{max,n} - \frac{DU^*}{Dt} \right)} \qquad (5.6)$$

The difference between the maximum horizontal acceleration at a time step (n) and the horizontal acceleration at each cell is used to mitigate the effect of cells with very small horizontal accelerations that may amplify the screening parameter erroneously. The total horizontal acceleration is used to include the horizontal wave propagation and the nonlinear steepening. The total horizontal acceleration can be decomposed into the horizontal wave propagation, which is characterized by the local horizontal acceleration:

$$\frac{\partial U^*}{\partial t} \qquad (5.7)$$

and the nonlinear steepening, which is characterized by the advection acceleration:

$$U^* \frac{\partial U^*}{\partial x} + W^* \frac{\partial U^*}{\partial z} \qquad (5.8)$$

In terms of the approximated non-hydrostatic pressure gradient, the screening parameter is:

$$\gamma \equiv \frac{\left(\frac{\partial}{\partial x}\int \frac{DW^*}{Dt} dz \right)}{\left(\left.\frac{DU^*}{Dt}\right|_{max,n} - \frac{DU^*}{Dt} \right)} \qquad (5.9)$$

Figure 5.4 shows the comparison between the approximated and modeled screening parameter. The approximated screening parameter slightly over-predicts non-hydrostatic regions through the water column, whereas the modeled screening parameter is located only at the steep wave front.

5.2 Application of the Non-hydrostatic Pressure Isolation Method

The non-hydrostatic pressure isolation method is applied to two different internal waves to demonstrate the method's ability to isolate regions with significant non-hydrostatic pressure effects.

5.2.1 Setup

The test basin is a 2D rectangular basin with an initial internal wave setup as specified in Table 5.1. The two different internal waves (internal wave 1 and internal wave 2) were initialized as a cosine wave with a three-layer hyperbolic-tangent density profile. The amplitude of internal wave 1 is 1.125 m, yielding an amplitude ratio (a/h) of 0.5. The amplitude of internal wave 2 is 0.3 m, yielding a/h = 0.1. Internal wave 1 is steep (a/L = 0.11), while internal wave 2 is much less steep (a/L = 0.04).

Internal wave 1 was simulated with three different square grids (20×15, 40×30 and 80×60, where each grid cell has dimensions of 0.5 m × 0.5 m, 0.25 m × 0.25 m and 0.125 m × 0.125 m, respectively). Square grids were chosen to avoid damping the non-hydrostatic effect over a grid with a small aspect ratio (§4.3). Internal wave 2 was simulated with the 40×30 grid.

5.2.2 Results

The non-hydrostatic pressure isolation method is an effective way to screen for and target areas that require a non-hydrostatic solution. However, the

Table 5.1: Dimensions of test basin.

Characteristic	Symbol	Value		Units
		Internal wave 1	Internal wave 2	
Length	L	10	10	m
Height	H	7.5	7.5	m
Upper layer depth	h	2.25	3.0	m
Depth ratio	h/H	0.3	0.4	--
Pycnocline thickness	h_{py}	5	5	m
Density gradient	$\Delta\rho$	4	4	kg/m^3

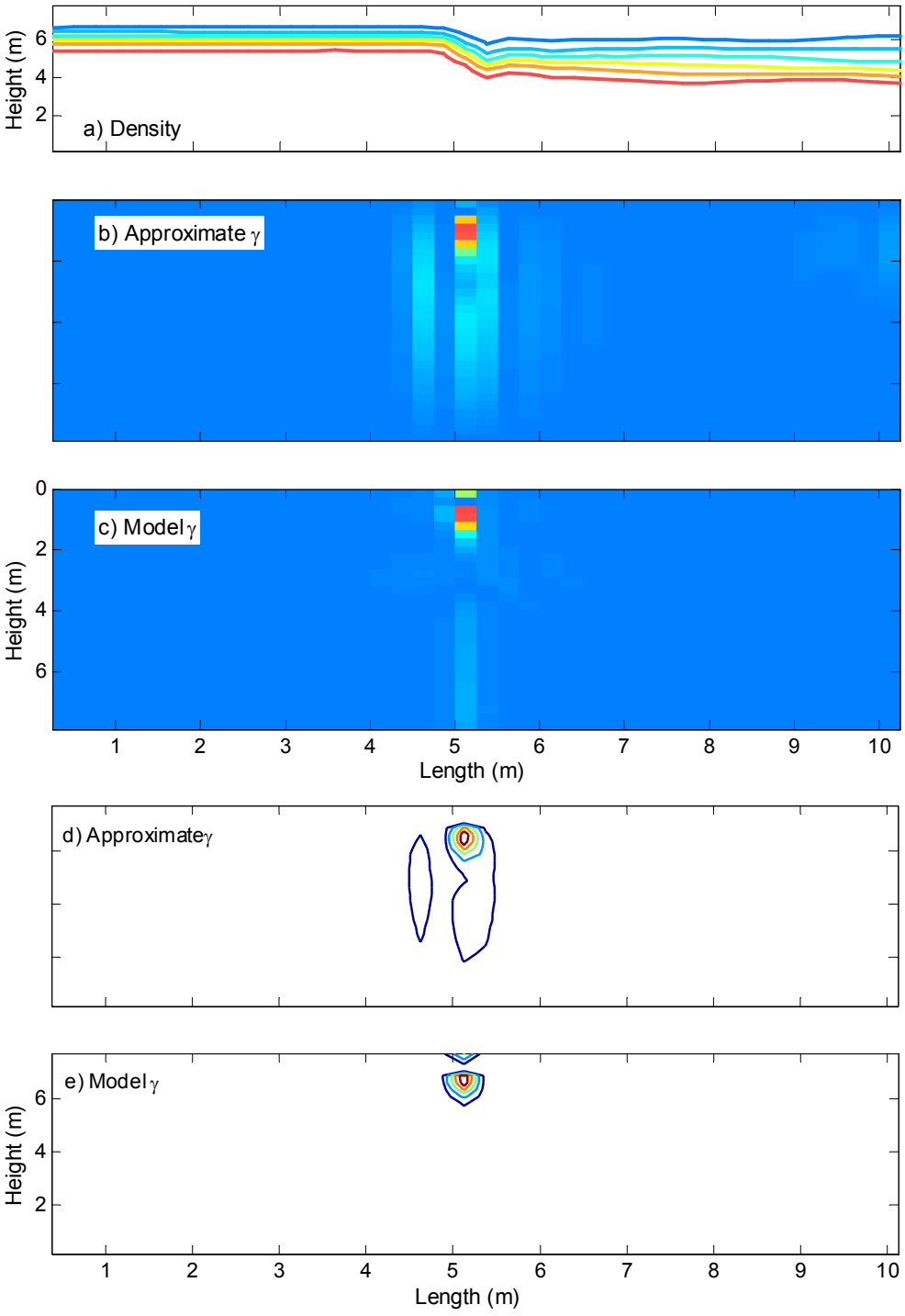

Figure 5.4: Comparison of screening parameter, γ. a) Density profile; b,d) γ calculated with the approximate non-hydrostatic pressure horizontal gradient; c,e) γ calculated with the model non-hydrostatic pressure horizontal gradient. In b and c, as cells scale from dark blue to dark red, the cell is considered more non-hydrostatic.

screening parameter requires a criterion for discriminating hydrostatic and non-hydrostatic regions. Where the screening parameter exceeds the criterion, that cell is considered non-hydrostatic, while a cell that has a screening parameter below the criterion is considered hydrostatic. Quantifying the criterion as a function of density gradients, wave characteristics and grid resolution is beyond the scope of this work. However, to demonstrate the behavior of the non-hydrostatic pressure isolation method, three different criteria were chosen ($\gamma = 1$, 5 and 10) and applied *a posteriori* to model results. Figures 5.5 and 5.6 show that as the non-hydrostatic screening parameter is increased, the region that is considered non-hydrostatic decreases. Figure 5.6 shows spikes in the number of cells that exceed the criterion about every 400 timesteps. This time coincides with when the steep wave fronts reflect off the basin wall, where the wave has large vertical velocities and therefore the non-hydrostatic effect is strong.

Three grid resolutions were applied to internal wave 1. The finest grid resolution (80×60) identified the most cells as non-hydrostatic, while the coarsest grid (20×15) identified the least (Figure 5.7). This does not imply that there are more non-hydrostatic regions with the finer grid, but rather there are more cells representing this region. Figures 5.4, 5.8 and 5.9 show that all grids have similar ability to identify the region of non-hydrostatic behavior.

Internal wave 1 is strongly nonlinear and so the non-hydrostatic pressure effect is strong at the wave front. Internal wave 2 is weakly nonlinear, nonetheless the non-hydrostatic pressure isolation method identifies the steepest part of the wave, as seen in Figure 5.10. Figure 5.11 shows a comparison between the number of cells with a screening parameter greater than one for internal wave 1 and internal wave 2. Internal wave 2 shows large rises in the number of cells considered non-hydrostatic when the wave is traveling along the basin and has the least number of non-hydrostatic cells when the wave is at the basin walls. When the wave is reflecting off the basin walls, the vertical and horizontal accelerations are greater than anywhere else in the basin, so the screening parameter is able to properly detect these regions with non-hydrostatic behavior. When internal wave 2 is traveling along the basin, it should not behave non-hydrostatically, as it is a near-linear wave. However, the horizontal accelerations are very small so the screening parameter is amplified. The filter used in the screening parameter to eliminate small accelerations does not work in the limit of very small horizontal accelerations. Thus, the screening parameter delineates regions as non-hydrostatic erroneously.

5.3 Summary

The new non-hydrostatic pressure isolation method identifies regions where the non-hydrostatic pressure effect is significant. For a sufficiently steep wave, the method is able to predict these regions quite well. For weakly nonlinear waves, the non-hydrostatic pressure isolation method tends to over-predict non-hydrostatic regions, due to the nature of a weakly nonlinear system. The method of the screening parameter takes the difference between the local horizontal acceleration and the maximum horizontal acceleration in the field to ameliorate the problem of small accelerations. Despite this construction, a weakly nonlinear system has such small accelerations that the non-hydrostatic screening parameter is still amplified. Thus, the present method is limited by the need to identify a characteristic horizontal acceleration scale, which herein is taken as the maximum value of the domain. If a wave is weakly nonlinear, and therefore hydrostatic, the non-hydrostatic pressure isolation method is not applicable. However, if a wave has significant steepening, then the non-hydrostatic pressure isolation method identifies non-hydrostatic regions. The results from the non-hydrostatic pressure isolation method must not be viewed alone, but with a general understanding of the nature of the modeled wave.

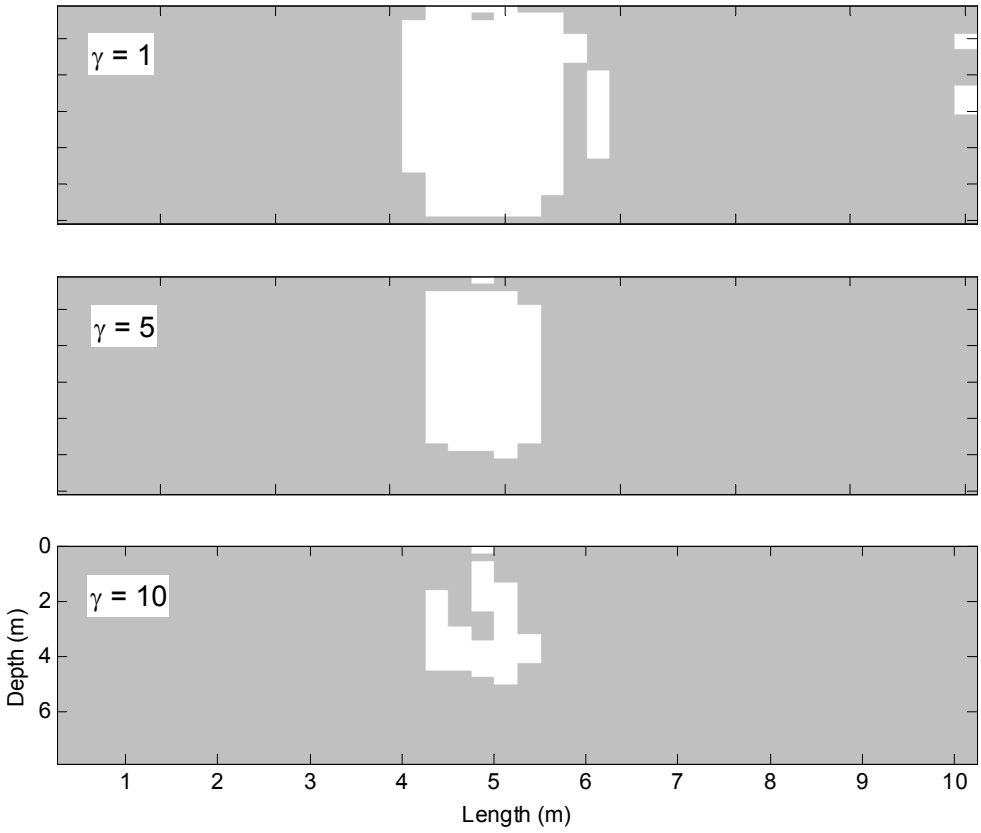

Figure 5.5: Internal wave 1 domains with different non-hydrostatic screening parameters. The white are regions considered non-hydrostatic and the black are regions considered hydrostatic.

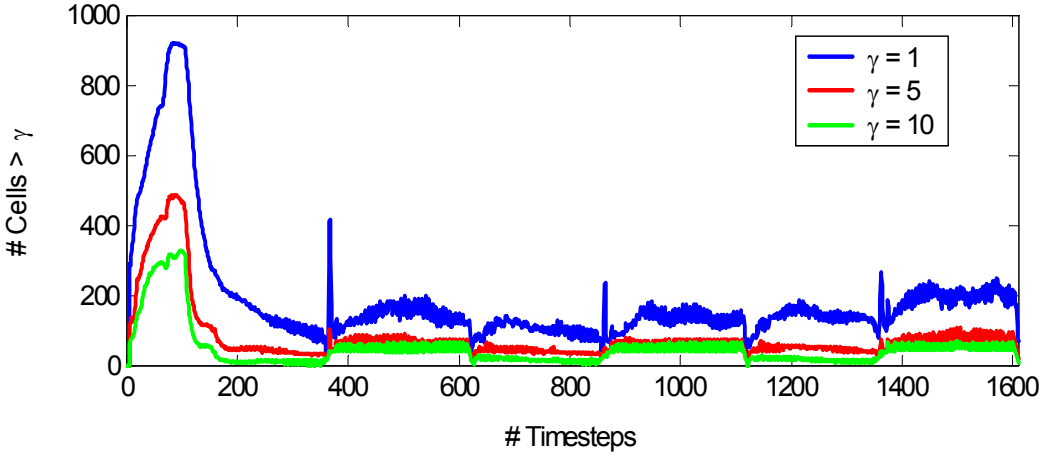

Figure 5.6: Number of cells considered non-hydrostatic for internal wave 1; γ > criteria for a 40×30 grid

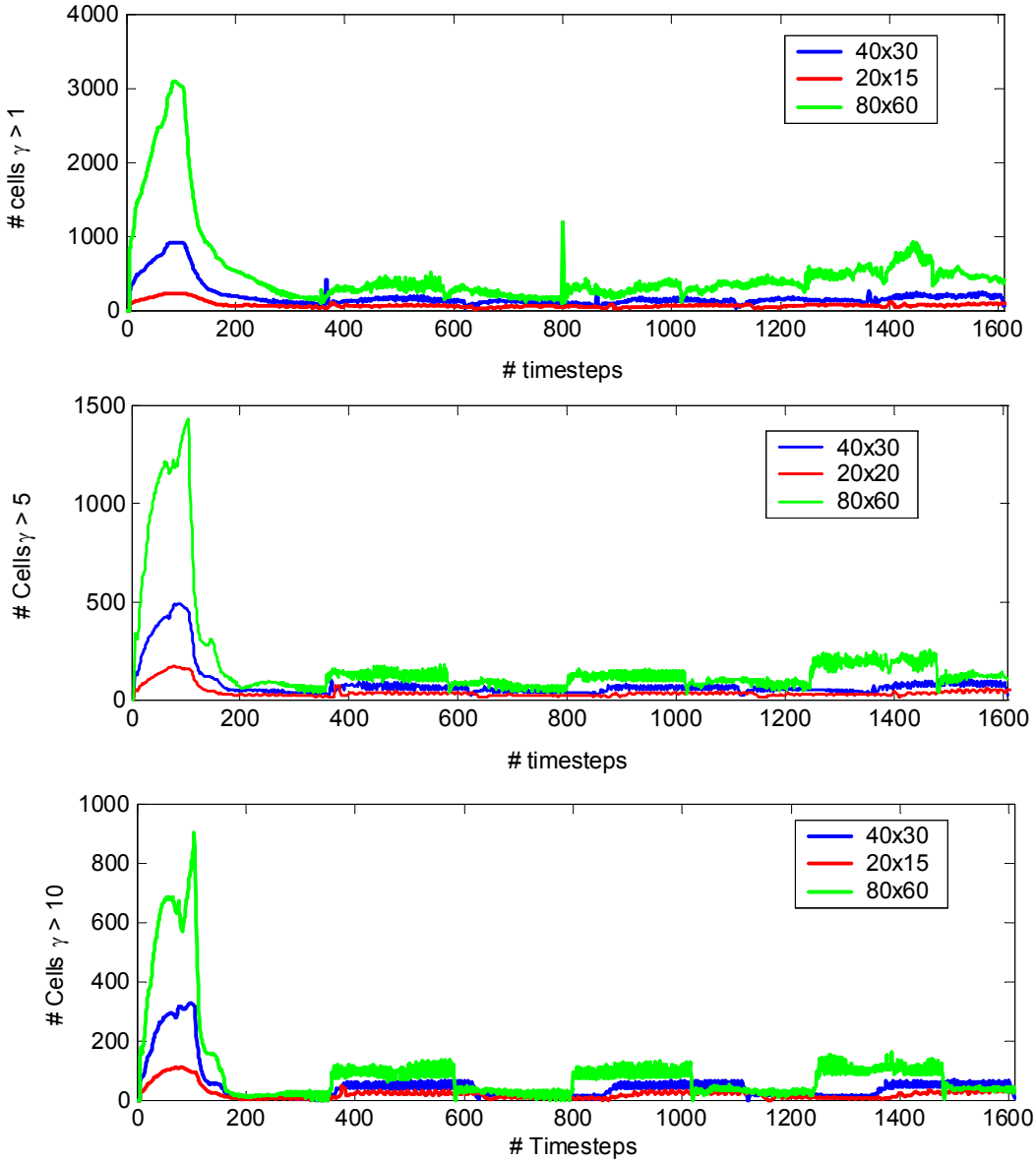

Figure 5.7: Number of cells considered non-hydrostatic for internal wave 1. Each panel has three different grids (blue line is 40×30 grid, red line is 20×15 grid and green line is 80×60 grid). The top panel is for a screening parameter, $\gamma > 1$; the middle panel has $\gamma > 5$ and the bottom panel has $\gamma > 10$.

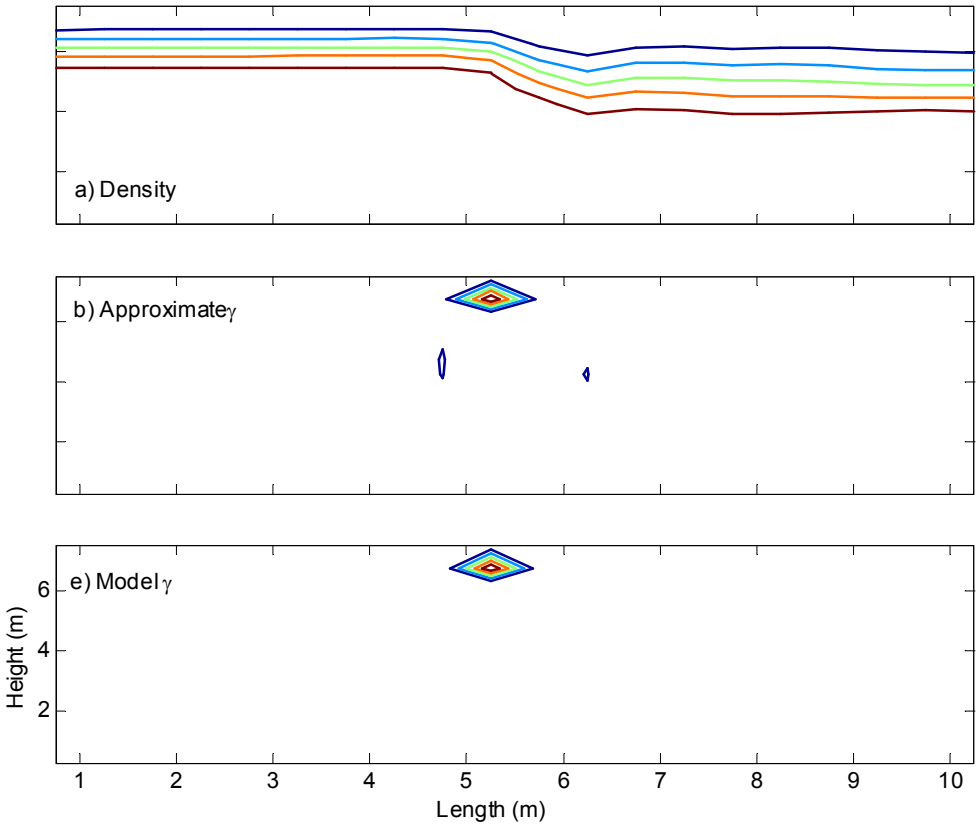

Figure 5.8: Comparison of non-hydrostatic screening parameter, gamma, on the 20×15 grid for internal wave 1. a) Density profile; b) γ calculated with the approximate non-hydrostatic pressure horizontal gradient; c) γ calculated with the model non-hydrostatic pressure horizontal gradient.

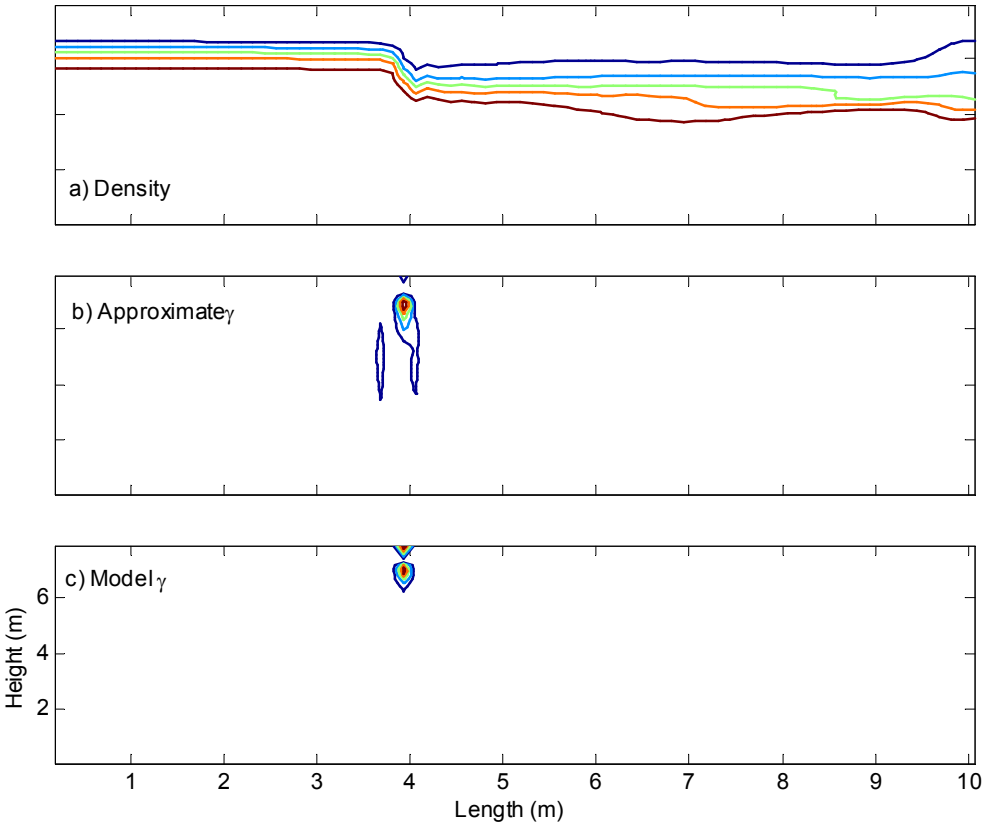

Figure 5.9: Comparison of non-hydrostatic screening parameter, gamma, on the 80×60 grid for internal wave 1. a) Density profile; b) γ calculated with the approximate non-hydrostatic pressure horizontal gradient; c) γ calculated with the model non-hydrostatic pressure horizontal gradient.

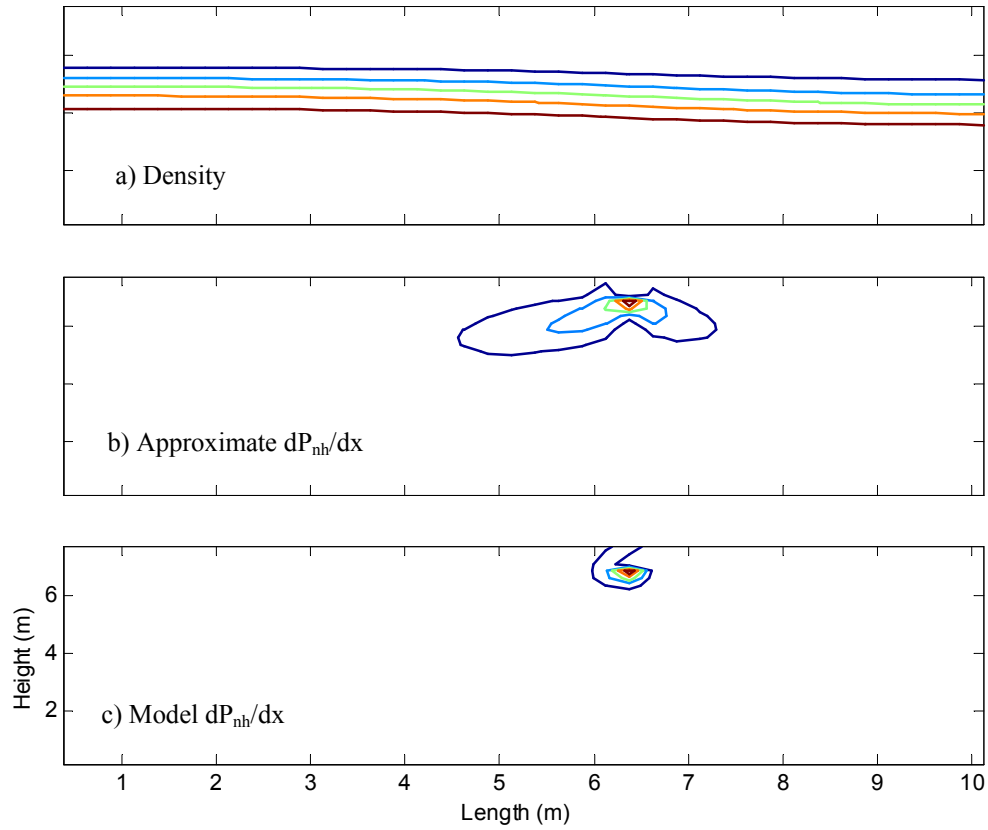

Figure 5.10: Comparison of non-hydrostatic pressure horizontal gradient for internal wave 2. a) Density profile; b) approximate non-hydrostatic pressure horizontal gradient; c) model non-hydrostatic pressure horizontal gradient.

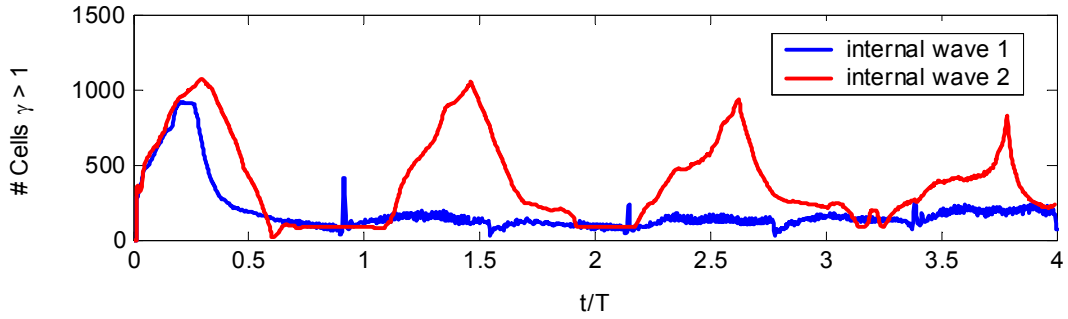

Figure 5.11: Number of cells considered non-hydrostatic for internal wave 1 (blue line) and internal wave 2 (red line). $\gamma > 1$.

Chapter 6. Conclusions and Recommendations

The two main objectives of the present research are:

- quantify the differences between hydrostatic and non-hydrostatic simulations of internal wave evolution, and
- develop a method to *a priori* determine regions with non-hydrostatic behavior.

Both of these objectives have been accomplished, and the results provide insight into the mechanisms that control internal wave modeling. This chapter: 1) summarizes the work and conclusions, 2) discusses a numerical issue that limits the rapidity of the pressure Poisson solution's convergence and 3) provides recommendations for future work.

6.1 Summary Discussion

Differences between the hydrostatic and non-hydrostatic representation of internal waves are considerable (§4.1). The hydrostatic model simulates half of the physics necessary to capture internal wave evolution (i.e. nonlinear acceleration). This allows the wave to nonlinearly steepen, but there is no physical term to model dispersion. Thus, the hydrostatic model is limited in capability to modeling hydrostatic shallow waves that remain essentially linear damped waves (§4.1, scenarios 1 and 6). However, the hydrostatic model is incapable of physically capturing the dispersion of a steepened wave into a train of solitons, as the hydrostatic model neglects the physics that control this process. The soliton-like formations observed in the hydrostatic model (in this work (§4) and Hodges and Delavan, 2004) change when the grid resolution for a hydrostatically-modeled wave is varied. This indicates that the size and shape of the soliton-like formations are dependent on the grid (§4.1.3) and therefore are a model fabrication. This finding is further confirmed by the power spectral density distributed over wavelengths; the peak power is not shifted to the wavelengths of the soliton-like formations, and any power that is seen in these waves is a result of harmonics (§4.1.3). Numerical error within the hydrostatic model accumulates to reduce the energy in the wave and eventually damp out the wave's steepness. Numerical diffusion can be reduced by vertically refining the grid, but the hydrostatic system is numerically dissipative, irrespective of the grid resolution.

Unlike the hydrostatic model, the non-hydrostatic model includes the non-hydrostatic pressure term, which acts as a dispersive force. Thus, as a wave steepens nonlinearly, the non-hydrostatic pressure applies an effect that disperses the wave into a train of solitons. Grid resolution affects the occurrence of the train of solitons (i.e. finer horizontal grids simulate more emerging soliton trains than a coarser grid, Figure 4.8). However, the characteristic wavelength of the solitons is relatively unaffected by grid resolution, compared to the hydrostatic model. The peak power in a wave system shifts to the characteristic soliton wavelength after solitons have emerged; the shift in power is indicative of an energy transfer from basin-scale wavelengths to soliton wavelengths. It is thus concluded that the non-hydrostatic model is indeed modeling the physics of internal wave evolution. Non-hydrostatic models do not eliminate numerical error, however, the characteristics of numerical error are different in a non-hydrostatic model than in a hydrostatic model. Like the hydrostatic model, vertical grid refinement reduces numerical diffusion. In contrast to the hydrostatic model, horizontal grid refinement greatly reduces numerical dissipation in the laboratory-scale case. The laboratory-scale case (§4.1.3) decreases dynamic energy by only 8% over nine wave periods for the finest grid resolution compared to the coarsest grid resolution which decreases dynamic energy by 85%. It appears that the neglect of non-hydrostatic pressure effectively acts as a dissipative term in the hydrostatic equations. Perhaps an alternative viewpoint is that the non-hydrostatic pressure redistribution of momentum reduces the numerical dissipation that is associated with shallow water conservation of momentum.

Grid resolution and the subsequent grid aspect ratio are the two model parameters that control the non-hydrostatic model's ability to capture internal wave evolution. Most of the lake-scale cases had very small grid aspect ratios [$O(10^{-3}) – O(10^{-4})$], and showed no significant difference between the hydrostatic and non-hydrostatic models. The one lake-scale case non-hydrostatic model that differed (in diffusion only) from the hydrostatic model had a grid aspect ratio of $O(10^{-2})$; the laboratory scale case, where results were significantly different between the hydrostatic and non-hydrostatic models, had grid aspect ratios of at least $O(10^{-2})$. Due to the successful use of the non-hydrostatic model for larger grid aspect ratios, the present research suggests that the grid aspect ratio must be at least of $O(10^{-2})$ to include the effect of non-hydrostatic

pressure. In addition to the fine spatial resolution needed for a physical, low numerical error non-hydrostatic model, the temporal resolution must also be fine enough to maintain a small vertical CFL condition.

The pressure Poisson solution is inherently stiff and is problematic for the motion of stiff pressure gradients at the front of an internal wave. The analytical solution (§3.1) provides a pressure Poisson equation that is independent of a flow field. However, the pressure Poisson solution for hydrodynamic problems (e.g. internal wave evolution) depends upon the gradient of velocity. The gradient of velocity generally does not match the speed of propagation of the non-hydrostatic pressure gradient. Indeed, this appears to be a key difference between non-hydrostatic solutions of internal waves and flows that have been more commonly studied using non-hydrostatic models. For example, flow over a backwards facing step (e.g. Su, et al., 1999) has an unsteady recirculation region behind the step due to non-hydrostatic pressure. The non-hydrostatic pressure gradients in the recirculation oscillate at the same timescale as the motion of the reattachment point, which is much longer than the timescale of advection. Thus, the advection velocity limits the model time step, from which it follows that local changes in the non-hydrostatic pressure gradient from one time step to another are small. As the time 'n+1' pressure field is a good initial guess at the time 'n' pressure field in a backwards-facing step, a Poisson solver should be able to rapidly converge. In contrast, when modeling an internal wave, for common subcritical flows the wave is faster than the fluid velocity, so the baroclinic wave speed limits the model time step. As the internal wave propagates rapidly through the model grid, non-hydrostatic pressure gradients at the wave front are propagated at the wave speed. Therefore, the non-hydrostatic pressure field may change quite dramatically between time steps, such that the time 'n' pressure field is a poor approximation of the time 'n+1' pressure field. This effect is demonstrated by simulating a monochromatic wave (§3.2) under two different conditions for the Poisson solution: 1) with the time 'n' pressure is used as the starting point for the time 'n+1' pressure solution; and 2) with zero pressure used as the starting point for all pressure solutions. Figure 3.9 shows that using the time 'n' pressure always requires a larger number of iterations to meet the convergence criterion.

The fine timestep and spatial grid needed to effectively apply the non-hydrostatic model renders the solution of real-world scale problems a future capability. The present research investigated a new method to identify regions with significant non-hydrostatic behavior. Using the non-hydrostatic pressure isolation method, a model may be developed which would "boot-strap" from a simpler hydrostatic model to a non-hydrostatic model in the regions identified as "non-hydrostatic." Such a hydrostatic/non-hydrostatic hybrid model should allow faster solution of internal wave evolution. However, there is a limit to the ability of the non-hydrostatic pressure isolation method. The method over-predicts non-hydrostatic regions in shallow waves. These shallow waves are ably modeled with the hydrostatic model, since steepening and soliton formation is not the dominant phenomenon in the wave's evolution. Thus, the non-hydrostatic pressure isolation method should only be applied to waves which are expected to steepen and form solitons (i.e. regime 2, Figure 3.10).

It is crucial to water quality modeling to have a hydrodynamic model to skillfully simulate the internal wave evolution and the flow field in a basin (Gross, et al, 1999). For damped linear internal waves, a hydrostatic model may adequately model the behavior as long as viscous damping is modeled. For internal waves where nonlinear steepening and soliton formation are the prevalent features, a non-hydrostatic model provides a physical simulation of internal wave evolution on a sufficiently fine grid, whereas the hydrostatic model does not. Thus, non-hydrostatic models should be used when nonlinear internal waves and solitons are present in the flow field; this will in turn create a more realistic representation of all the system processes that depend on the flow field, such as those in a water quality model.

6.2 Conclusions

The conclusions that may be drawn from the present work are:

- The present hydrostatic model of the Euler equations shows soliton-like formations for nonlinear/non-hydrostatic waves, which are an artifact of the numerical model and grid resolution.
- There is some evidence that the grid aspect ratio ($\Delta z/\Delta x$) must be greater than $O(10^{-2})$ to capture the effect of non-hydrostatic pressure in the present non-hydrostatic model.

- A hydrostatic model can be used to identify internal-wave regions with non-hydrostatic behavior.

6.3 Recommendations

The research presented here investigates emerging areas within non-hydrostatic modeling. This work began to chip away at some of the issues challenging non-hydrostatic modeling, but much remains to be investigated. The most notable issue that must be examined in non-hydrostatic modeling is simulation time. To diminish simulation times, this author believes there are two main approaches: 1) address the issue of stiffness, and 2) construct a hybrid model that uses the non-hydrostatic pressure isolation method.

The pressure Poisson equation is inherently stiff, but the stiffness is exacerbated by the advection methods used. Presently, the velocity at the previous timestep is used in the source term of the pressure Poisson equation; this velocity moves much slower than the wave and the non-hydrostatic pressure gradients. One suggestion to improve the source term of the pressure Poisson equation would be to use a predicted advection velocity field from the previous two timesteps. For instance, use a second-order Adams-Bashforth which predicts the 'n+1' velocity from the 'n-1' and 'n' velocities. Using the past two timesteps may better estimate the strong velocity gradients near the propagating wave front.

A second approach to improve the source term in the pressure Poisson equation is to use the non-hydrostatic pressure isolation method to identify the point at an instant in time with the peak non-hydrostatic pressure gradient. This point should coincide with the propagating wave front and the strongest velocity gradients. Identifying the location with peak non-hydrostatic pressure gradients, along with the known timestep, will yield the velocity that of the peak non-hydrostatic pressure gradient. This velocity should be characteristic of the wave speed, which may be used to provide a better estimation of the non-hydrostatic pressure field.

The non-hydrostatic pressure isolation method developed here only provides the relative importance of the non-hydrostatic pressure effect in the internal wave's evolution. In application, the non-hydrostatic screening parameter needs some criterion to delineate a region as "hydrostatic" or "non-hydrostatic." For example, where the screening parameter is above a preset criterion, a cell is designated as "non-hydrostatic." At this cell, the non-hydrostatic solver may be called to calculate the non-hydrostatic pressure and the updated velocity field and free-surface. The criterion for a region to be considered non-hydrostatic must be established. The author does not know if there will be a global value for the non-hydrostatic screening parameter criterion, or if it will be dependent on each wave characteristics.

Another issue associated with the implementation of the non-hydrostatic pressure isolation method is that any change in the velocity field propagates instantaneously over the entire domain. Thus, changes within the interior of the domain may cause perturbations on the free-surface that could feed back into the flow in the form of non-conservation in mass and volume. There must be some transition between the "hydrostatic" and non-hydrostatic" cells; the transition may be handled by buffer cells. The buffer cells will account for any free-surface perturbation and make a correction to the system to ensure conservation of mass and volume. The size of the buffer region must also be investigated to determine if it is a function of the magnitude of the non-hydrostatic pressure gradients or the size of the non-hydrostatic region.

Finally, the non-hydrostatic model must be examined on more real-world scale cases with different grid resolutions to determine if the instability found in the lake-scale case (§4.2) is a model error or an issue with the fractional-step method. To verify the present research's assessment that a grid aspect ratio of at least $O(10^{-2})$ must be used to observe differences between the hydrostatic and non-hydrostatic model, the lake-scale case should be applied to finer grids. Additionally, the present non-hydrostatic pressure solver should be adapted to use a preconditioned conjugate gradient method or a multigrid method to improve convergence time.

Acknowledgements

This research was supported under the Office of Naval Research Young Investigator Program Award 2001 of Ben R. Hodges, ONR Contract No. N00014-01-1-0574. The Centre for Water Research at the University of Western Australia provided the ELCOM numerical model used in this work under a research partnership agreement with the University of Texas at Austin.

Bibliography

Apel, J.R., (1981). Satellite sensing of ocean surface dynamics. Ann. Rev, Earth & Planetary Sci., 8:303-342.

Armfield, S. and R. Street, (1999). The fractional-step method for the Navier-Stokes equations: the accuracy of three variations. J. Comp. Phys., 153:2:660-665.

Batchelor, G.K., (1967). An Introduction to Fluid Dynamics. Cambridge Univeristy Press, New York, 615 pgs.

Blumberg, A.F., & G.L. Mellor, (1987). A description of a three-dimensional coastal ocean circulation model, in Three-Dimensional Coastal Ocean Models, N. S. Heaps (ed.), American Geophysical Union, Washington D.C. pp. 1-16.

Boegman, L., J. Imberger, J.N. Ivey, & J.P. Antenucci, (2003). High frequency internal waves in large stratified lakes. Limnol. & Oceanogr., 48:12:895-919.

Casulli, V., (1999). A semi-implicit finite difference method for non-hydrostatic, free-surface flows. Int. J. for Numer. Methods in Fluids, 30:425-440.

Casulli, V. & G.S. Stelling, (1998). Numerical simulation of 3D quasi-hydrostatic free-surface flows. J. Hydraul. Engng. 124:678-686.

Chen, X., (2003). A fully hydrodynamic model for three-dimensional free-surface flows. Int. J. for Numer. Methods in Fluids, 42:929-952.

Cushman-Roisin, B., (1994). Introduction to Geophysical Fluid Dynamics. Prentice Hall, New Jersey, 320 pgs.

Daily, C. & J. Imberger, (2003). Modeling solitons under the hydrostatic and Boussinesq approximations. Int. J. for Numer. Methods in Fluids, 43:231-252

Delavan, S.K., (2003). Evolution Accumulation of Numerical Errors in Hydrostatic Models of Internal Waves, M.S. Thesis, Department of Civil Engineering, University of Texas, Austin, Aug, 2003.

De Silva, I.P.D., J. Imberger, & G.N. Ivey, (1997). Localized mixing due to a breaking internal wave ray at a sloping bed. J. Fluid Mech. 350:1-27.

Ezer, T., H, Arango, A.F. Shchepetkin (2002). Developments in terrain-following ocean models: intercomparisons of numerical aspects. Ocean Modelling, 4:249-267

Farmer, D.M., (1978). Observations of long nonlinear internal waves in a lake. J. Phys. Oceanogr., 8:63-73.

Ferziger, J.H. & M. Perić, (2002). Computational Methods for Fluid Mechanics. Springer, Berlin, Germany, 423 pgs.

Fringer, O. B., & R. L. Street. 2003. The dynamics of breaking progressive interfacial waves. J. Fluid Mech. 494: 319-353.

Garrett, C. and W. Munk, (1979). Internal waves in the ocean. Ann. Review Fluid Mech., 11:339-369.

Gill, A.E., (1982). Atmosphere-Ocean Dynamics, Academic Press: New York, 1982.

Gross, E.S., J.R. Koseff, & S.G. Monismith, (1999). Three-dimensional salinity simulations of South San Francisco Bay, J. Hyd. Engr., 125:11:1199-1209.

Haidvogel, D.B., H.G. Arango, K. Hedstrom, A. Beckmann, P. Malanotte-Rizzoli, A.F. Shchepetkin, (2000). Model evaluation experiments in the North Atlantic Basin: simulations in nonlinear terrain-following coordinates. Dynamics of Atmospheres and Oceans. 32:239–281.

Hamrick, J.M., (1992). A three-dimensional environmental fluid dynamics computer code: Theoretical and computational aspects. The College of William and Mary, Virginia Institute of Marine Science, Special Report, 317, 63 pgs.

He, P., M. Salcudean, I.S. Gartshore, and P. Nowak, (1996). Multigrid calculation of fluid flows in complex 3D geometries using curvilinear grids. Computers and Fluids, 25:4:395-419.

Hirsch, C., (1988). Numerical Computation of Internal and External Flows, Volume 1: Fundamentals of Numerical Discretization. John Wiley & Sons, Inc., New York, 515 pgs.

Hodges, B.R., (2000). Numerical Techniques in CWR-ELCOM (code release v.1). CWR Manuscript WP 1422 BH, Centre Water Res., Nedlands, Western Australia, Australia.

Hodges, B.R., (2004). Accuracy of semi-implicit shallow-water Crank-Nicolson discretization. ASCE J. Eng. Mech., 130:8:904-910.

Hodges, B.R. & S.K. Delavan, (2004). Numerical diffusion and dissipation in hydrostatic

models of internal waves. ASCE Engineering Mechanics Conference Proceedings, June 13-16, 2004.

Hodges, B.R., J. Imberger, A. Saggio and K. Winters, (2000). Modeling basin-scale internal waves in a stratified lake, Limnology and Oceanography, 45:7:1603-1620.

Horn, D.A., J. Imberger, & G.N. Ivey, (2001). The degeneration of large-scale interfacial gravity waves in lakes. J. Fluid Mech., 434:181-207.

Horn, D. A., J. Imberger, G. N. Ivey, and L. G. Redekopp. (2002). A weakly nonlinear model of long internal waves in closed basins. J. Fluid Mech., 467:269-287.

Hutter, K., G. Bauer, Y. Wang & P. Guting, (1998). Forced motion response in enclosed lakes. In Physical Processes in Lakes and Oceans (ed. J. Imberger), AGU.

Imberger, J., (1994). Transport processes in lakes: A review, p. 79-193. In R. Margalef [ed.], Limnology now: A paradigm of planetary problems. Elsevier Science.

Imberger, J. & G.N. Ivey, (1993). Boundary mixing in stratified reservoirs. J. Fluid Mech., 248:477-491.

Javam A., J. Imberger & S.W. Armfield, (1999). Numerical study of internal wave reflection from sloping boundaries. J. Fluid Mech., 396:183-201.

Kantha, L.H. & C.A. Clayson, (2000a). Numerical Models of Oceans and Oceanic Process, Academic Press, New York, 940 pgs.

Kantha, L.H. & C.A. Clayson, (2000b). Small Scale Processes in Geophysical Fluid Flows, Academic Press, New York, 888 pgs.

Kao, T.W., F. Pan, & D. Renouard, (1985). Internal solitons on the pycnocline: generation, propagation, and shoaling and breaking over a slope. J. Fluid Mech., 159:19-53.

Kim, J. and P. Moin, (1985) Application of a fractional-step method to incompressibleNavier-Stokes equations. J. Comp. Phys., 59:308-323.

Kinsman, B., (1965). Wind Waves: Their Generation and Propagation on the Ocean Surface. Dover Publications, Inc., New York, 676 pgs.

Kreyszig, E, (1999). Advanced Engineering Mathematics. John Wiley & Sons, Inc., New York, 1156 pgs.

Kundu, P.K. and I.M. Cohen, (2002). Fluid Mechanics, Academic Press, New York, 730 pgs.

Laval, B., B.R. Hodges, & J. Imberger, (2003a). Reducing numerical diffusion effects with a pycnocline filter. J. Hydraul. Engrgr., 129:215-224.

Lamb, H., (1932). Hydrodynamics. Dover Publications, Inc., New York, 738 pgs.

Laval, B., J. Imberger, B.R. Hodges, and R. Stocker. (2003b). Modeling Circulation in Lakes: Spatial and Temporal Variations. Limnology and Oceanography 48:3:983-994.

Leonard, B.P. (1979). Stable and accurate convective modeling procedure based on quadratic upstream interpolation. Computer Meth. in Appl. Mech. & Engr., 19:1:59-98.

Leonard, B.P. (1991). The ultimate conservative difference scheme applied to unsteady one-dimensional advection. Computer Meth. in Appl. Mech. & Engr., 88:17-74.

Lighthill, J. (1978), Waves in Fluids, Cambridge University Press, Cambridge, 504 pgs.

Lin, B. and R.A. Falconer, (1997). Tidal flow and transport modeling using ULTIMATE QUICKEST scheme. J. Hyd. Engr., 123:4:303-314.

Long, R.R., (1972). The steepening of long, internal waves. Tellus, 24:88-99.

Lorenz, E.N., (1955). Available potential energy and the maintenance of the general circulation. Tellus, 7:157-167.

Mahadevan, A., J. Oliger, & R. L. Street, (1996a). A non-hydrostatic mesoscale ocean model. Part I: Wellposedness and scaling. J. Phys. Oceanogr., 26:1868-1880.

Mahadevan, A., J. Oliger, & R. L. Street, (1996b). A non-hydrostatic mesoscale ocean model. Part II: Numerical implementation. J. Phys. Oceanogr., 26:1881-1900.

Marshall, J., C. Hill, L. Perlman, & A. Adcroft, (1997). Hydrostatic, quasi-hydrostatic, and nonhydrostatic ocean modeling, J. Geophys. Res., 102:5733-5752.

Miropol'sky, Yu. Z. (2001). Dynamics of Internal Gravity Waves in the Ocean, Kluwer, Dordrecht, 406 pgs.

Moore, G. (1965). Cramming more components onto integrated circuits. Electronics, 38:8.

Nishri, A., J. Imberger, W. Eckert, I. Ostrovsky, & Y. Geifman, (2000). The physical regime and the respective biogeochemical processes in the lower water mass of Lake Kinneret, Limnol. Oceanogr., 45:4:972-981.

Osborne A.R. and T.L. Burch, (1980). Internal solitons in the Andaman sea. Science, 208:4443:451-460.

Roache, P. J., (2002). Code verification by the method of manufactured solutions. J. Fluids Eng. 124:1:4-10.

Roy, C.J., (2003). Grid convergence error analysis for mixed-order numerical schemes. Amer. Inst. Aeronautics Astronautics, 41:4:595-604.

Segur, H. & J.L. Hammack, (1982). Soliton models of long internal waves. J. Fluid Mech., 118:285-304.

Signal Processing Toolbox User's Guide, (1998). The MathWorks, Inc.

Stansby, P.K. & J.G. Zhou, (1998). Shallow-water flow solver with non-hydrostatic pressure: 2D vertical plane problems. Int. J. Numer. Methods in Fluids, 28:542-563.

Su, M. D., K. Xu, and M. S. Ghidaoui. (1999). Low-speed flow simulation by the gas-kinetic scheme. J. Comput. Phys., 150:1:17-39.

Tartinville, B., E. Deleersnijder, P. Lazure, R. Proctor, K.G. Ruddick, and R.E. Uittenbogaard, (1998). A coastal ocean model intercomparison study for a three-dimensional idealized test case. App. Math. Modelling., 22:3:165-182.

Turner, J. S. (1973). Buoyancy effects in fluids. Cambridge Univ. Press, NY USA.

van Haren, H., (2004). Some observations of nonlinearly modified internal wave spectra. J. Geophys. Res., 109(C03045).

Wadzuk, B.M. & B.R. Hodges, (2003). Comparing hydrostatic and non-hydrostatic Navier-Stokes models of internal waves. ASCE Engineering Mechanics Conference, July 16-18, 2003.

Weilbeer, H. and J.A. Jankowski, (2000). A three-dimensional non-hydrostatic model for free surface flows – development, verification and limitations. Estuarine and Coastal Modeling: Proceedings of the 6th International Conference, Nov. 3-5, 1999.

Whitham, G.B., (1974). Linear and nonlinear waves, Wiley, NY, USA, 636 pgs.

Wiegand, R.C. and E.C. Carmack, (1986). The climatology of internal waves in a deep temperate lake. J. Geophys. Res., 91:C3:3951-3958.

Winters, K.B., P.N. Lombard, J.J. Riley & E.A. D'Asaro, (1995). Available potential energy and mixing in density-stratified flows. J. Fluid Mech., 289:115-128.

Yuan, H. & C.H. Wu, (2004). A two-dimensional vertical non-hydrostatic σ model with an implicit method for free-surface flows. Int. J. Numer. Meth. Fluids, 44:811-835.